공학박사 학위논문

A study to predict instrumented indentation curve through the analysis of entropy flow at high temperature

고온에서의 엔트로피 유동 해석을 통한

계장화 압입 곡선 예측 연구

2018년 2월

서울대학교 대학원

재료공학부

박 찬 평

A study to predict instrumented indentation curve through the analysis of entropy flow at high temperature

고온에서의 엔트로피 유동 해석을 통한
계장화 압입 곡선 예측 연구

지도교수 권 동 일

이 논문을 공학박사 학위논문으로 제출함
2017 년 12 월

서울대학교 대학원
재료공학부
박 찬 평

박찬평의 박사학위 논문을 인준함
2017 년 12 월

위 원 장 한 흥남
부위원장 권 동 일
위 원 박 은 수
위 원 최 병 학
위 원 정 은 채

Abstract

Chan-Pyoung Park
Dept. Materials Science and Engineering
The Graduate School
Seoul National University

Instrumented indentation testing (IIT) can measure many mechanical properties, from basic properties, such as elastic modulus and hardness, to advanced properties, such as tensile properties, fracture toughness, fatigue and creep; this is done by measuring the penetration depth from a material surface of an indenter in loading and unloading. The strongest advantage of instrumented indentation testing over conventional mechanical testing is that the specimen volume required is very small, giving IIT the merits of simplicity, economy, non-destructiveness, and in-field applicability. Thus, instrumented indentation testing can be used for various materials from metal alloys to amorphous materials to bio materials, and it can also be used over a wide range of scales from macro to micro/nano. However, because IIT is a new test method, studies of IIT have focused primarily on validating the testing method itself and correlating its results with those of other testing methods. In addition, studies on IIT have largely been carried out at room temperature; research at high and low temperatures or in corrosive environments are relatively few. The reason for

this narrow focus is that, for example, thermal drift (the temperature difference between indenter and specimen) can lead to error in mechanical measurements, making it difficult to ensure stable experimental data.

The goal of this thesis was to reduce the error reported in previous research and to develop a high-temperature instrumented indentation system (HTIIS) appropriate for the macro scale in temperatures up to 650°C. This entailed devising a method to determine the accurate contact area. The pileup phenomenon around the indenter in high-temperature IIT was quantified and its physical meaning was analyzed, and a new calibrating factor $f_{(T)}$ was developed to correct for the pileup effect. Conventional high-temperature Vickers testing was conducted to verify the reliability of HTIIS and the use of $f_{(T)}$. However, the difficulty in determining the contact area function is that the experiments must be performed every time at the same temperature: in other words, the contact area calibration function depends on the sample and on the experimental conditions. Therefore, to break away from that empirical study, an additional compensating study was performed.

In this compensating study, the relationship of hardness and temperature, that is a modified Westbrook's equation, is newly defined using the shape of existing constitutive equations containing thermodynamic foundation. In the mathematical development here, the physical meaning of each parameter is considered. Thus the indentation contact depth for penetration can be expressed as a function of the indentation variables and temperature. In addition, the

contact area using the newly defined equation is compared to that from conventional optical observations. And, to ensure the validity of that compensating study results, hardness values for the same materials obtained from a different institution are compared with hardness results from this study. This sequence of studies suggests a general equation to calculate the contact area and hardness at high-temperatures.

However, high-temperature indentation and material behavior cannot be fully elucidated by these mechanical approaches because the specimens are affected by heat energy. Therefore, a theoretical thermodynamic consideration of heat was necessary. First, the concept of indentation work as defined by Cheng and Cheng can be extended to resilience as a mechanical parameter, and its relationship with stiffness, which can be obtained from the unloading curve in IIT, was investigated. In addition, the relationship was explored between stiffness and internal energy, which is a thermodynamic parameter. The relationship between the stiffness and Helmholtz free energy can be investigated by analyzing the entropy flow during loading and unloading in high-temperature IIT. That is, after indentation, the entropy contributing to elastic recovery of the impression mark is calculated, and it is confirmed that the mechanical factor and the thermodynamic factor can be combined through entropy. these Hence the load-depth (L-h) curve at high temperature can be predicted by the change in the indentation depth according to the temperature and the stiffness-Helmholtz relationship. A calibration method for the predicted L-h curve is suggested using

the maximum IIT load measurable at room temperature. The predicted high-temperature *L-h* curve is verified by comparison with the *L-h* curve measured at the actual temperature. This thesis provides a new perspective on the analysis of the indentation load-depth curve, and posits a mathematical relevance and physical meaning of the parameters that should be considered in high-temperature studies.

Keyword: Instrumented Indentation Testing; Hardness; Stiffness; Entropy; Helmholtz Free Energy; High-Temperature

Student Number: 2008-20649

Contents

List of Tables

List of Figures

Chapter 1

INTRODUCTION

Contents

1.1. Objective of the Thesis

Instrumented indentation testing is more advanced than conventional hardness testing in measuring various mechanical properties of materials. To evaluate these mechanical properties, information about indentation contact area is required. In particular, the deformation behavior of metals at high-temperatures seems to differ from that at room temperature, and thus for accurate evaluation of mechanical characteristics at high-temperatures, the high-temperature contact area should be used. In this thesis, an instrumented indentation system for high-temperatures was developed and measurement-errors caused by equipment temperature were calibrated. In addition, the pileup effect during indentation was studied at different temperatures. A new equation for the high-temperature contact area is proposed. And additional compensated study also was performed. The high-temperature deformation behaviors of eight Cr-Mn alloy steels are investigated over a wide temperature range by instrumented indentation testing. The hardness-temperature relation of the conventional Westbrook model is newly modified to contain more physical meaning by considering the effect of temperature. Additionally, a comprehensive relation equation is developed using indentation-depth

parameters to describe the contact area at high temperatures. From the thermodynamic consideration, this thesis can suggest a new method to predict high-temperature indentation curves using room-temperature macro-scale instrumented indentation testing. Physical investigations on the elastic recovery phenomenon of an indentation mark after unloading confirm that it can be expressed in terms of work, resilience, and indentation stiffness. It is also confirmed that elastic recovery of impression mark can be explained by internal energy or Helmholtz free energy through thermodynamic analysis. Thus, by tracing the entropy flow which dominates the high-temperature indentation process, this thesis can prove experimentally a proportional relationship between stiffness and inverse Helmholtz free energy and can obtain an equation describing this relation. In addition, a temperature-dependent indentation depth function, some geometric assumptions about the indentation curve, and experimental conditions are also introduced for predicting the high-temperature indentation curve.

1.2. Organization of the Thesis

This thesis consists of has eight chapters. After a brief introduction in Chapter 1, Chapter 2 shows a mathematically fundamental theorem on indentation contact. In the chapter 2, we investigate the stress fields by Vector analysis on local force. Chapter 3 gives the solution about the shape of the indentation curve, and Chapter 4 shows the physical interpretation for the elastic-plastic deformation under the indenter. From chapter 2 to chapter 4, the elastic and elastic-plastic contact theory is derived as the basic principle of the instrumented indentation testing in sharp indenter and spherical indenter. Chapter 5 shows the method to determine the contact area considering pileup phenomenon at high-temperature. Chapter 6 is the compensated study of chapter 5. In chapter 6, we suggest the modified Westbrook's model for accurate derivation of contact area and show the high-temperature hardness. Chapter 7 is the most important section in this thesis. In chapter 7, we consider a wide range of principle in thermodynamic, material mechanics, even quantum mechanics to explain the unloading curve of indentation testing. And finally we can propose the method to predict high-temperature load-depth curve. Chapter 8 summarizes the results of this thesis.

Chapter 2

Modeling on Indentation Contact

Contents

2.1. Boussinesq's Problem

To thinking about an elastic contact mechanics, we need to consider previous research that is called "Boussinesq's Problem".

Boussinesq's Problem [2.1] is considering about load, displacement, stress and strain relations when local force is applied on a surface of a certain semi-infinite elastic material like figure 2.1. Basically the material is assumed to be elastic material which behaves linear on stress-strain curve, so material behavior could be simplified to one-dimensional equation. By simplifying the material's behavior, rather material facts would be excluded than we can focus on stress-strain distribution and displacement changes when force is applied on a local area. The reason why Boussinesq's Problem is so important is that the question is throwing fundamental questions about load-displacement curve by obtaining Instrumented Indentation Test (IIT). It requires solutions about physical explain, mathematical relation and geometrical form of load-displacement curve. Namely, load-displacement curve is occurred as a form of power series, Boussinesq's problem treats a root questions such as why curve is showed that form, what's a meaning of the curve.

One of goals of this study is to predict load-displacement curve at high-temperature, to achieve this goal, how to drive load-displacement curve in mathematical logic, and fundamentally what means that curve can be a first step of this study.

To solute Boussinesq's Problem, a wide academic knowledge is required such as second order ordinary differential equation, vector analysis, Bessel equation, Fourier-Bessel transformation, elastic mechanics, and tensor theory. Here Fourier-Bessel transformation is called Hankel transformation. To solve the question, at first mathematical definition is needed and this mathematical definition is started by modeling from natural phenomenon.

2.1.1. Assumption of Boussinesq's Problem

Proper assumptions are needed to modeling the circumstance that local pressure is applied on the surface of a linear elastic body. The assumptions are followed next.

- Material satisfies Hook's Law and differentiable function in linear continuum.
- Material has isotropy mechanical properties.
- Stress field, strain field, and displacement are occurred radial direction when force is applied.

Hook's Law can be written a tensor form like equation (2-1)

$$\sigma_{ij} = \lambda \varepsilon_{kk} \delta_{ij} + 2\mu \varepsilon_{ij} \qquad (2\text{-}1)$$

Here λ and μ are Lame's constant and can be defined equation (2-2) and equation (2-3). λ means elastic properties occurred normal direction. That's why λ is posited in front of ε_{kk}. μ is commonly written G and means elastic properties occurred shear direction. δ is called Kronecker delta and defined equation (2-4). ν means Poisson's ratio.

$$\lambda = \frac{vE}{(1+v)(1-2v)} \tag{2-2}$$

$$\mu = G = \frac{E}{2(1+v)} \tag{2-3}$$

$$\delta_{ij} = \begin{cases} 1, \ if \ \ i = j \\ 0, \ if \ \ i \neq j \end{cases} \tag{2-4}$$

Kronecker delta is not a physical parameter but mathematical operator. Kronecker delta have a role of change *i, j, k, l* to *0* and *1* when multiplication of tensor. There are many times changing order or turn in tensor operation, so using Kronecker delta, calculation could be easy, and complex equation form could be written simple form.

Stress field, strain field, and displacement field are occurred to radial directions, when local pressure applied on elastic body like figure (2.2) and figure (2.3) and have a symmetric along with Z-axis. At this time, load flow applied, like equation (2-5), can be regard as one point by the area being gone to limit 0.

$$P_z = \lim_{a \to 0} \int_{A_a} P_0 dA_a \qquad (2\text{-}5)$$

In the case of axial-symmetric problem, in analysis, total body does not consider in an object of analysis, it is used instead of 2-dimensional plane which is based on revolution. By thinking this, complex 3-dimensional problem could be convert simple 2-dimential problem. Now like figure 2.4, let's consider fields existed on plane and take out one element involved in fields. From now on, changing field and stress state of one element is paid attention.

2.1.2. Vector Field and Gradient

When load applied to local area on elastic body, and so, Load (=force) divides area, then the concept of stress is made. When stress exists much then, the concept of stress field is made. In this stress field, the element has potential energy at each position. Stress field occurs at the same time of load applied, and changes in succession so stress field should be modeled no equilibrium state but changing state itself. To describe these changing states, mathematically differential equation must be adopted. And also, the field has an amount and direction, the concept of vector is needed. Equation (2-6) shows stress field change in Cartesian coordinates and can be known of expressing as a vector differential equation form. Equation (2-7) shows a location of an element posited on coordinates as a function of φ

$$\vec{\nabla} = \frac{\partial}{\partial x}\vec{e}_x + \frac{\partial}{\partial y}\vec{e}_y + \frac{\partial}{\partial z}\vec{e}_z \qquad (2\text{-}6)$$

$$\varphi = \varphi(x, y, z) \qquad (2\text{-}7)$$

Here equation (2-6), $\vec{\nabla}$ is called Nebula. And it is itself a Vector and simultaneously a differential operator. It means a certain change state itself mathematically.

In the changing stress field, element has a different potential energy with closing center of applied pressure and with receding centroid. If gravity which is affected to centroid of element is defined as a body force (*b*), the forces received to element in the field is composed of potential energy and body force. And Gradient arises by a gulf of position of element like figure 2.5. The equilibrium equation about Gradient is showed in equation 2-8. Equation 2-8 means the total sum of body force in a Vector dimension has same value with multiplication of potential function of element.

$$\tilde{b} = -\vec{\nabla}\varphi \qquad (2\text{-}8)$$

$$\vec{\nabla}\varphi = \frac{\partial\varphi}{\partial x}\vec{e}_x + \frac{\partial\varphi}{\partial y}\vec{e}_y + \frac{\partial\varphi}{\partial z}\vec{e}_z \qquad (2\text{-}9)$$

$\tilde{b}$ is a total sum of gravity energy affected to elements, and called body force. $\vec{\nabla}$ is a differential operator which shows changing state, and Vector function. φ means a certain position which element have, and it has a potential energy by having different status, and is a Scalar function. The result of multiplication of $\vec{\nabla}$ and φ is called Gradient and it is a Vector function.

2.1.3. Divergence Theorem and Element

Let's consider the force which is affected to the element inside of stress field. A force is a Vector, so it propagates radial direction from a center of applied load like figure (2.6). If element exists on the line of force movement, amount of force does not accumulate inside of element, whereas element outputs force as much as inputs. Because in elastic theorem, the element is regard as virtual fact that would not be deformed, so the force affected to deformation is considered to be not exist. Therefore, to keep a certain equilibrium state of force, amount of force must go as far as coming. These points can be also explained by Newton mechanics. In the Newton mechanics, element is considered element to be mass-free called mass point. it means element has a mass but has not volume. It is influenced by gravity because of mass however the concept like deformation does not come true because of volume-free. Therefore if there is no volume and no deformation, the amount of incoming force should be equal to the amount of force that goes out. In another way, let's think about those using thermodynamic's 1^{st} law, law of energy conservation, and Newton's 3^{rd} law, action-reaction law. Even if Newton's assumption that there is no volume could not apply to elastic

body, so even though assuming a particle has a very small volume of its size, incoming force, action and reaction of force in atom scale inside of the element, namely the force is worked between attractive and repulsive, so eventually the force inside of element is offset and has a zero value. For this reason, the amount of force that goes out equals the amount of incoming force. And it does not violate law of energy conservation.

Newton mechanics are often used to describe the force between planets and planets in space macroscopically. However the greatness of Newtonian mechanics is still valid when explaining the force between molecular or atomic scale. Even if the element contains very small volume in spite of the fact that Newton's assumption is against it, by applying thermodynamic 1^{st} law and Newton's 3^{rd} law, volume of element has very small and with being able to close to zero. The element in elastic theory satisfies the law of Newtonian 1, 2 and 3. And also it is defined as satisfying the thermodynamic 1^{st} law. The important point is that the mass of the element is close to zero, but the volume is not equal to zero, it is clearly exist.

In these point of view, the force should not accumulate inside of element and exit to outside, when the force comes out outside, it may come out vertically from the plane or it may come out of a certain direction of

which it is not perpendicular. If the force is pulled vertically, Divergence theorem of Gauss' theorem is established. If the force is pulled out of the arbitrary angle, then the boundary condition is determined.

Divergence theorem, that is Gauss' theorem, is that the amount of force which comes into element is equal to the amount of force that comes out from element. Ant then, the amount of force coming through the volume is equal to the amount of force which is goes out through planes. At this point, the direction of the force which goes out though plane has a perpendicular direction with plane. Expressed in equation, it is expressed as follows as equation (2-10).

$$\int_{vol} \vec{\nabla} \cdot \vec{r}\, dv = \int_{sur} \vec{r} \cdot \vec{n}\, ds \qquad (2\text{-}10)$$

When the integral factor is a volume, the total sum of force which enters into the volume has the same amount need to be taken out when the integral factor is a plane of element. At this time, the direction shall be perpendicular to the plane. In equation (2-10), $\vec{n}$ indicates that the direction of the force is perpendicular to the plane. By Divergence theorem, coming force is equal to outing force, so the amount of force

inherent in the element, which is very small, has zero value. Equation 2-11 shows that the position of the element above the changing stress field is represented by a differential equation. While the field always has a value of changing, it shows that the value of the φ function has zero value because any energy or force is accumulated in the element. So equation 2-11 means incoming force and outing force is same and becomes at equilibrium state.

$$\vec{\nabla} \cdot \varphi(\vec{r}, \vec{z}) = 0 \qquad (2\text{-}11)$$

When equation 2-11 deploy in dot product, it can be shown as equation 2-12.

$$\frac{\partial \varphi_r}{\partial r} + \frac{\partial \varphi_z}{\partial z} = 0 \qquad (2\text{-}12)$$

Here φ is a potential function according to location of element. Nebula is a Vector function and φ is also a Vector function however the result of dot product is a Scalar function because of disappear of basis Vector.

2.1.4. Boundary Condition

A head of time, it is known that incoming force has a same amount of outgoing force. And the force can be passed through a plane as a form of perpendicular. However the force does not always divergence vertically, but most often divergence with an arbitrary angle. At this point, inside of elastic body, along with a center, a certain specific point coming force, arrangements of atoms or lattices are varied depending on distance. And an arrangement line of lattice, which differ significantly from the distance, would occur. These differences of arrangement of atoms or lattices cause a density difference when the force is passed. And it by these density differences makes boundary condition. So like a figure 2.7, the force passing through a specific boundary, $\vec{A}_1$, can be changed to $\vec{A}_2$. $\vec{A}_1$ and $\vec{A}_2$ can be express as a form of Vector component, like equation 2-13 and 14.

$$\vec{A}_1 = r\cos\theta(t) + b(n) \qquad (2\text{-}13)$$

$$\vec{A}_2 = r\cos\theta'(t) + b(n) \qquad (2\text{-}14)$$

If thinking that tangential component of two Vectors in equation 2-13 and equation 2-14 is same with equation 2-15, like equation 2-16, relationship between normal components, boundary coefficient, ρ_2 / ρ_1, is appeared by difference of density.

$$\vec{A}_{1,\tan} = \vec{A}_{2,\tan} \qquad (2\text{-}15)$$

$$\vec{A}_{1,nor} = \frac{\rho_2}{\rho_1} \vec{A}_{2,nor} \qquad (2\text{-}16)$$

As shown in figure 2.7. $\vec{A}_{1,nor}$ can be thought as a body force because of a vertical direction from centroid of element. And $\vec{A}_{2,nor}$ can be thought as a potential energy function, φ. Therefore equation 2-16 can be re-write using the relation between total sum of body force all elements have and potential energies of elements. And since the boundary coefficient, ρ_2 / ρ_1, is generated by a density difference fundamentally, it can be expressed as a *D* and written equation 2-16 to equation 2-17.

$$\widetilde{b} = D\varphi(\vec{r}, \vec{z}) \qquad (2\text{-}17)$$

So when a force is applied in a certain single point, boundary condition can be defined like equation 2-17.

2.2. Laplace equation & Airy's Stress Function

2.2.1. Laplace equation

Now using Gradient according to location of element, Divergence theorem passing through element, and boundary condition, about the force that work at certain points, differential equation of element can be produced which is considered field. Let's derive a differential equation by using equation (2-8), (2-11) and (2-17).

$$\tilde{b} = -\vec{\nabla}\varphi \qquad (2\text{-}8)$$

$$\vec{\nabla} \cdot \varphi(\vec{r}, \vec{z}) = 0 \qquad (2\text{-}11)$$

$$\tilde{b} = D\varphi(\vec{r}, \vec{z}) \qquad (2\text{-}17) \text{ where } \varphi = \frac{1}{D}\tilde{b}$$

At first equation (2-17) is modified about φ and substitute into equation (2-11). Then equation (2-18) is derived.

$$\vec{\nabla} \cdot (\frac{1}{D} \tilde{b}) = 0 \qquad (2\text{-}18)$$

And being Substituted body force which defined equation (2-8) into equation (2-18). Then equation (2-19) is derived. Here *D* is disappeared during the process of calculation because of constant which has a different value per each material.

$$\vec{\nabla} \cdot (-\frac{1}{D} \vec{\nabla} \varphi) = 0 \qquad (2\text{-}19)$$

$$\vec{\nabla} \cdot (\vec{\nabla} \varphi) = 0 \qquad (2\text{-}20)$$

Being deployed Nebula in equation (2-20) and operated dot product in Cartesian coordinates, and then equation (2-23) is derived. Equation (2-24) is rewrite form of equation (2-23) by tensor code.

$$\left(\frac{\partial}{\partial x} \hat{x} + \frac{\partial}{\partial y} \hat{y} + \frac{\partial}{\partial z} \hat{z} \right) \cdot \left(\frac{\partial \varphi}{\partial x} \hat{x} + \frac{\partial \varphi}{\partial y} \hat{y} + \frac{\partial \varphi}{\partial z} \hat{z} \right) = 0 \qquad (2\text{-}21)$$

$$\left(\frac{\partial^2\varphi}{\partial x^2}+\frac{\partial^2\varphi}{\partial y^2}+\frac{\partial^2\varphi}{\partial z^2}\right)=0 \qquad (2\text{-}22)$$

$$\nabla^2\varphi=0 \qquad (2\text{-}23) \quad \text{where } \varphi=\varphi(x,y,z)$$

$$\left(\frac{1}{r}\frac{\partial}{\partial r}\left(r\frac{\partial\varphi}{\partial r}\right)+\frac{1}{r^2}\frac{\partial^2\varphi}{\partial\theta^2}+\frac{\partial^2\varphi}{\partial z^2}\right)=0 \qquad (2\text{-}24)$$

The equation (2-23) is a well-known Laplace differential equation and φ function is a Scalar function. Equation (2-24) is a deployed form of equation (2-23) using cylindrical coordinates. Location information of element wherever it is can be known using Laplace equation in semi-infinite elastic body. And though this, it is possible to know where distribution of potential energy which elements have. The Laplace equation is not used in material mechanics only. In mechanics engineering, when heating source is existed, Using Laplace equation, it is possible to determine temperature distributions or heat distributions according to distance. In electronic engineering, when electron source is existed, it is possible to determine electron distributions according to distance. Like this, in material mechanics, when force source is existed, it

can be known force distributions according to distance. Force is a kind of energy like a heat or an electronic, so by grasping the position of element which contains energy like a dish, it can be possible to derive field's shape.

So far, when load is applied to elastic body, a task is conducted to verify the location information of element within the field. Element is on a state of equilibrium of force so an elastic concept of stress and strain can be applied to each element. Therefore, when the force is applied, the stress and strain field can be identified. So this provides critical information to design structure or to identify the safety of structure in use.

In the following chapters, the applying stress and yielding strain factors acting on elements is to be carried out. The key to deriving stress and strain is to use φ function of equation (2-23). The equation (2-23) is the form of a multiplication of square of Nebula and φ function. Nebula square is a Vector itself, but it provides information about coordinates as a differential equation, however the information on how much stress is in the actual coordinates and how much strain is provided with φ function. In order to calculate stress, stain and displacement using φ function, a mathematical equation should be created by introducing a mathematical analysis technique so-called method of complex potential function for

plane elasticity. In this paper, Stress function, a kind of potential function methods, is used by Airy proposed in 1862 years [2.2]. As explained earlier, the Boussinesq's Problem can be replaced by the simple 2-dimensional plane stress-strain problem, because it has a symmetric along with Z-axis. The most common method to solve 2D plane problem is Airy stress function, and the advantage of this method is that the equations such as equilibrium equation, constitution equation, displacement-strain equation, and compatibility condition for stress analysis can be expressed simply as a differential equation with containing a singular unknown function. Airy stress function is capable of deriving the solution much easier than Navier's equation, which is commonly used in 3-dimensional stress analysis problem. Namely the general idea of Airy stress function is to develop a stress field that satisfies equilibrium and yields a single governing equation from the compatibility equation. In this chapter, the introduction of elements is derived from a simple point of view and induced the equation for Laplace equations. However in the following chapter, focus move from the field to the element itself, and consider the Boussinesq's Problem by using the Airy stress function method.

2.2.2. Airy's Stress Function and a Part of Maxwell's equation

The equation (2-25) and equation (2-26) will be used to construct a equilibrium equation by grasping a certain element from a certain field plane, as shown in Figure 2.8.

$$\frac{\partial \sigma_x}{\partial x} + \frac{\partial \tau_{xy}}{\partial y} + b_x = 0 \qquad (2\text{-}25)$$

$$\frac{\partial \sigma_y}{\partial y} + \frac{\partial \tau_{xy}}{\partial x} + b_y = 0 \qquad (2\text{-}26)$$

In the preceding equation, the body force of element on plane could be expressed as a function of a certain potential function like equation (2-8)

$$\tilde{b} = -\vec{\nabla}\varphi \qquad (2\text{-}8)$$

The tensor form of equation (2-8) is translated into a differential equation form like equation (2-27) and (2-28)

$$b_x = -\frac{\partial \varphi}{\partial x} \qquad (2\text{-}27)$$

$$b_y = -\frac{\partial \varphi}{\partial y} \qquad (2\text{-}28)$$

Equation (2-25) and (2-26) can be modified using equation (2-27) and (2-28). And then it can be expressed like equation (2-31) and (2-32)

$$\frac{\partial \sigma_x}{\partial x} + \frac{\partial \tau_{xy}}{\partial y} + \left(-\frac{\partial \varphi}{\partial x} \right) = 0 \qquad (2\text{-}29)$$

$$\frac{\partial \sigma_y}{\partial y} + \frac{\partial \tau_{xy}}{\partial x} + \left(-\frac{\partial \varphi}{\partial y} \right) = 0 \qquad (2\text{-}30)$$

$$\frac{\partial}{\partial x}(\sigma_x - \varphi) + \frac{\partial}{\partial y}\tau_{xy} = 0 \qquad (2\text{-}31)$$

$$\frac{\partial}{\partial x}\tau_{xy} + \frac{\partial}{\partial y}(\sigma_y - \varphi) = 0 \qquad (2\text{-}32)$$

If stress components, $\sigma_x, \sigma_y, \tau_{xy}$, are set as derivative functions, F and G, it is known that the equation (2-31) and (2-32) are automatically satisfied.

$$\sigma_x - \varphi = \frac{\partial F}{\partial y}, \qquad \tau_{xy} = -\frac{\partial F}{\partial x} \tag{2-33}$$

$$\tau_{xy} = -\frac{\partial G}{\partial y}, \qquad \sigma_y - \varphi = \frac{\partial G}{\partial x}, \tag{2-34}$$

However, as shown in Figure 2.8, it can be inferred from equation (2-35) because of $\tau_{xy} = \tau_{yx}$.

$$\frac{\partial F}{\partial x} = \frac{\partial G}{\partial y} \tag{2-35}$$

The equation (2-35) will always be satisfied if the function, F and G defined earlier, is selected using new unknown function ϕ like equation (2-36)

$$F = \frac{\partial \phi}{\partial y}, \qquad G = \frac{\partial \phi}{\partial x} \tag{2-36}$$

When substituting equation (2-36) into equation (2-33) and (2-34), then equation (2-37), (2-38), and (2-39) are obtained.

$$\sigma_x = \frac{\partial^2 \phi}{\partial y^2} + \varphi \tag{2-37}$$

$$\sigma_y = \frac{\partial^2 \phi}{\partial x^2} + \varphi \tag{2-38}$$

$$\tau_{xy} = -\frac{\partial^2 \phi}{\partial x \partial y} \tag{2-39}$$

The new unknown function, ϕ, is called Airy stress function in equation (2-37), (2-38), and (2-39). The significance of the deploying equation is in the equation (2-35). The equation (2-35) infers that one partial differential variable $\partial F / \partial x$ coming from x, except another partial differential variables y component, is same with one partial differential variable $\partial G / \partial y$ coming from y, except another partial differential

variable x. The adequacy of the equation (2-35) can be explained by Maxwell relation, which deals with reversible and irreversible processes. In nature, the irreversible process easily takes place in the direction of increasing entropy. Therefore, it may be obvious that the x component of stress is expressed to $\partial F / \partial y$ and the y component of stress is expressed to $\partial G / \partial x$. However, it is doubtful that reversal process, that is, x component of stress can be expressed to $\partial F / \partial x$, and y component of stress can be expressed to $\partial G / \partial y$. This seems to be a reversible process at first glance, seemingly very difficult, unnatural, and decreasing entropy process. But there is no need to be odd. The answer to this question lies in the material. In previous chapter, it was assumed that material was a linear elastic body which could be calculated in differential. If the material is linear elastic body, the reversible and irreversible process can be occurred in cycles. Mathematically explaining, partial differential of function of F and partial differential of function G shear the same differential $\partial^2 \phi / \partial x \partial y$ and make exact form. The exact form in differential equation means that it can be occurred independent of the path, and this means that when returning to the reversible process again, that exact form can be used as a circular loop. In thermodynamics, the irreversible process occurs spontaneously, whereas any reversible

process that will return to its original state must meet any cost or any required condition. Here the condition is only possible when the each function F and G are shared with a certain unknown function like ϕ. Thus, Airy stress function is an application of Maxwell relation in material mechanics, the key is an introducing a new unknown function which allows irreversible process and reversible process.

If the force of gravity can be applied anywhere so body force of element could be ignored in equation, from equation (2-37), (2-38), and (2-39), the vertical stress component and the shear stress components can be obtained. And if stress is obtained, the strain can also be obtained by using Hook's law. Therefor the important point will be traced back how to determine the unknown function ϕ. However, in order to determine the unknown function ϕ, in the case of obtaining the solution of stress, Airy stress function should satisfy compatibility condition predominately. Compatibility condition, in the 2-dimension plane problem, arises due to the fact that three strain component, $\varepsilon_x, \varepsilon_y, \gamma_{xy}$, do not correspond to the two displacement component. u, v in one-to-one. So in order to connect the strain and displacement, it is necessary to satisfy a certain condition, such as equation (2-40)

$$\frac{\partial^2 \varepsilon_x}{\partial y^2} + \frac{\partial^2 \varepsilon_y}{\partial x^2} = \frac{\partial^2 \gamma_{xy}}{\partial x \partial y} \qquad (2\text{-}40)$$

In case of plane problems, the relationship between stress and strain is shown in equation (2-41), (2-42), and (2-43), where v represents the poisson ratio and E is the elastic modulus.

$$\varepsilon_x = \frac{1+v}{E}[(1-v)\sigma_x - v\sigma_y] \qquad (2\text{-}41)$$

$$\varepsilon_y = \frac{1+v}{E}[(1-v)\sigma_y - v\sigma_x] \qquad (2\text{-}42)$$

$$\gamma_{xy} = \frac{2(1+v)}{E}\tau_{xy} \qquad (2\text{-}43)$$

If equation (2-41), (2-42), and (2-43) substitute into equation (2-40), and eliminate common part then equation (2-44) is derived.

$$\frac{\partial^2}{\partial y^2}[(1-v)\sigma_x - v\sigma_y] + \frac{\partial^2}{\partial x^2}[(1-v)\sigma_y - v\sigma_x] = 2\frac{\partial^2 \tau_{xy}}{\partial x \partial y} \tag{2-44}$$

The equation (2-43) is converted by substituting the equation (2-37), (2-38), and (2-39), which is Airy stress function ignored force of gravity. Then equation (2-45) is derived. Here in Cartesian coordinates used.

$$\frac{\partial^4 \phi}{\partial x^4} + 2\frac{\partial^4 \phi}{\partial x^2 \partial y^2} + \frac{\partial^4 \phi}{\partial y^4} = 0 \tag{2-45}$$

The equation (2-45) is the partial differential governance equation about ϕ function. If this equation is revised, the new form of equation is shown as equation (2-46)

$$\left(\frac{\partial^4}{\partial x^4} + 2\frac{\partial^4}{\partial x^2 \partial y^2} + \frac{\partial^4}{\partial y^4}\right)\phi = \left(\frac{\partial^2}{\partial x^2} + \frac{\partial^2}{\partial y^2}\right)^2 \phi = (\nabla^2)^2 \phi = \nabla^4 \phi = 0 \tag{2-46}$$

The equation (2-46) is represented in the square of Laplace equation, and that kind of differential equation is referred to as a bi-harmonic equation. Therefore, looking for the solution for hi-harmonic equation means

situation where force is applied, and wherein equilibrium state of element, geometrical compatibility, and field change which contains distribution of elements so finally means to obtain stress and strain with considering those factors. But it remains still to be resolved to determine the shape of unknown function, ϕ, in bi-harmonic equation. At the next chapter, in combination with all the consideration discussed so far, Mathematical form of Boussinesq's Problem will be created. Boussinesq's Problem is not a matter of mathematical form, but merely, like Figure 2.1, throws a physical situation where the force is applied on the surface of the semi-infinite elastic body. Therefor it is the responsibility of the researcher to consider what should be considered in these physical circumstances, how to express it mathematically, and how to write properly the problem mathematically.

2.3. Vector Analysis on Local Force

2.3.1. Vector Analysis of Surface Section on Elastic Body

In the previous chapter, when local force applied on the surface of elastic body, field distribution of force and moving behavior of element on field was explained. In addition, when force exerted on element, the equilibrium state of force and geometric compatibility of element was considered. And finally as a result, bi-harmonic equation was derived. in this chapter this bi-harmonic equation will be substituted into coordinates. So far, the development of the thesis has developed by using Cartesian coordinates. The reason is that most of elastic problems at first understand issues using Cartesian coordinates. And after it, the issues convert to a polar coordinates system, or cylindrical coordinates system, to be suitable for objects which are intended for actual situation. Initially, the reason why the Cartesian coordinate is used is that the orthogonal coordinate system can be easily understood in space, and the reason for using polar coordinate system or the cylindrical coordinate system is that

it takes into account the geometry of the real condition, not just three dimensions. By considering the geometric shape of the target (element, field), a more practical factor can be given to mathematical problem. The indentation situation is likely to use polar and cylindrical coordinate system because the distribution of stress and strain is radiated rather than using a rectangular coordinate system. The distribution of force in indentation, it can be divided into distribution of forces on the surface and inside the material.

The distribution of force on the surface can be expressed by means of a Vector, as shown in Figure 2.9. If the force is applied at one point, the distribution of force on the surface will spread in $\vec{r}$ direction, forming an angle of θ degrees around the origin. At this point, the equilibrium equation of force can be regard to be $\sigma_{rr}\sin\theta = \sigma_{yy}$ in 2-diminsinal, then, following mathematical condition is like equation (2-47)

$$P_0 = -\int_0^{\pi} \sigma_{rr}\sin\theta \cdot r \cdot d\theta \qquad (2\text{-}47)$$

The reason for the negative sign in the equation (2-47) means inside direction, on the surface of material and within the boundaries, namely,

technically speaking, because normal stress held positive sign in boundary, and how to set the direction is depend on researcher. The boundary condition can be express like equation (2-48) in all $\vec{r}$ direction. Since the distribution of force at the initial assumption is referred to as axial-symmetric, so when r =*Constant*, then $\sigma_{r\theta} = 0$ and σ_{rr} also can be thought that base is *y* direction, $\vec{e}_y$. That is, it shall have a symmetrical distribution like $\sin\theta$ to $\theta = \pi/2$. And also when P_0 is r =Constant, it have an equilibrium with the sum of force that applied to *y* direction by σ_{rr} which applied to surface. These terms are as follows in equation (2-48 a), and (2-48 b).

$$\sigma_{r\theta} = 0 \ : \{0 < \theta < \pi\} \ \forall r \qquad \text{(2-48 a)}$$

$$\sigma_{rr} = \text{symmetric with respect to } \theta = \pi/2 \qquad \text{(2-48 b)}$$

Earlier, the field change could be explained by Laplace equation. Equation (2-23) is re-written down again for the sake of developing the thesis.

$$\nabla^2\varphi = \vec{\nabla}\cdot\vec{\nabla}\varphi \qquad \text{(2-23)}$$

As the force is applied, it will be deformed, and this deformation occurs with satisfying equation (2-47), (2-48), and (2-23). At the same time, the geometric compatibility also is satisfied. The equation (2-40)~(2-43) shall be written like equation (2-49) in the form of tensor for the sake of convenience.

$$\vec{\nabla} \otimes \vec{\nabla} \varphi \qquad (2\text{-}49)$$

Now condition equation which obtained from surface of elastic body and stress field equation are obtained. The equation (2-48 a) which means boundary condition is substituted into equation (2-23) and if it satisfies equation (2-49) which means geometrical compatibility, then Airy stress function (φ) is expressed as follows in equation (2-50) and (2-51). See Figure 2.9 below for an explaining, and the bottom equation is the expression of each stress component using a polar coordinate system.

$$\sigma_{rr} = \frac{1}{r}\frac{\partial \varphi}{\partial r} + \frac{1}{r^2}\frac{\partial^2 \varphi}{\partial \theta^2} \qquad (2\text{-}50\ a)$$

$$\sigma_{\theta\theta} = \frac{\partial^2 \varphi}{\partial r^2} \qquad \text{(2-50 b)}$$

$$\sigma_{r\theta} = \frac{1}{r^2}\frac{\partial^2 \varphi}{\partial \theta} - \frac{1}{r}\frac{\partial^2 \varphi}{\partial r \partial \theta} \quad \text{where} \quad \sigma_{r\theta} = 0 \qquad \text{(2-50 c)}$$

$$\sigma_{r\theta} = \frac{1}{r^2}\frac{\partial^2 \varphi}{\partial \theta} - \frac{1}{r}\frac{\partial^2 \varphi}{\partial r \partial \theta} = 0 \qquad \text{(2-51)}$$

The equation (2-51) is a differential formula, so let's try to integrate it by θ to seek original form.

$$\int\left(\frac{1}{r^2}\frac{\partial^2 \varphi}{\partial \theta}\right)d\theta = \int\left(\frac{1}{r}\frac{\partial^2 \varphi}{\partial r \partial \theta}\right)d\theta \qquad \text{(2-52)}$$

$$\frac{1}{r}\varphi_{(r,\theta)} = \frac{\partial \varphi_{(r,\theta)}}{\partial r} \qquad \text{(2-53)}$$

If $\varphi_{(r,\theta)}$ puts $\varphi(r,\theta) = R(r)\Theta(\theta)$ then, it is possible to apply the Separation of Variables method.

$$\frac{R(r)\Theta(\theta)}{r} = \frac{\partial[R(r)\Theta(\theta)]}{\partial r} \qquad (2\text{-}54)$$

$$\frac{1}{r}\partial r = \frac{1}{R(r)\Theta(\theta)}\partial[R(r)\Theta(\theta)] \qquad (2\text{-}55)$$

$$\ln r = \ln R(r)\Theta(\theta) \qquad where\ \ \theta = 0 \qquad (2\text{-}56)$$

$$then\ \ R(r) = r \qquad (2\text{-}57)$$

Therefore, when localized force is applied to the surface of elastic body, the force of direction $\vec{r}$ is derived from a constant value r, and θ indicates zero whatever the form of function is. Thus, the force on the surface is expressed as $r\hat{r}$.

2.3.2. Vector Analysis of longitudinal section on Elastic Body

Previous chapter, the distribution of force was considered along the surface of elastic body. Now in this chapter, the distribution of force which is inside the body rather than on surface will be considered. Figure 2.10 shows the situation of longitudinal section when a force is applied at a single point. Previously the distribution of force inside the material as shown in the equation (2-24) could be express using form of Laplace equation.

$$\left(\frac{1}{r}\frac{\partial}{\partial r}\left(r\frac{\partial \varphi}{\partial r}\right)+\frac{1}{r^2}\frac{\partial^2 \varphi}{\partial \theta^2}+\frac{\partial^2 \varphi}{\partial z^2}\right)=0 \qquad (2\text{-}24)$$

From the first assumption, the deformation of elastic body is axial-symmetric, the distribution of force above equation (2-24) shall be zero with direction of θ. Therefore the equation (2-24) can be re-written as follows equation (2-58), it can be known that φ function are easily separated as a function of *R(r)* and *Z(z)*.

$$\left(\frac{1}{r}\frac{\partial}{\partial r}\left(r\frac{\partial\varphi}{\partial r}\right)+\frac{\partial^2\varphi}{\partial z^2}\right)=0 \qquad (2\text{-}58)$$

$$\varphi = R(r)Z(z) \qquad (2\text{-}59)$$

If substituting equation (2-58) into equation (2-59) and deploying it. Equation (2-64) is derived. *k* of equation (2-64) is *Eigen value* for solving differential equation, the terms about *r* and about *z* are represented each *Eigen function (r)* and *Eigen function (z)*.

$$\frac{1}{r}\frac{\partial}{\partial r}\left\{r\frac{\partial}{\partial r}(R(r)Z(z)\right\}+\frac{\partial^2}{\partial z^2}\{R(r)Z(z)\}=0 \qquad (2\text{-}60)$$

$$Z\frac{1}{r}\frac{\partial}{\partial r}\left\{r\frac{\partial R}{\partial r}\right\}+R\frac{\partial^2}{\partial z^2}Z=0 \qquad (2\text{-}61)$$

$$\left(\frac{1}{RZ}\right)Z\frac{1}{r}\frac{\partial}{\partial r}\left\{r\frac{\partial R}{\partial r}\right\}+\left(\frac{1}{RZ}\right)R\frac{\partial^2}{\partial z^2}Z=0 \qquad (2\text{-}62)$$

$$\frac{1}{r}\frac{1}{R}\frac{\partial}{\partial r}\left\{r\frac{\partial R}{\partial r}\right\}+\frac{1}{Z}\frac{\partial^2}{\partial z^2}Z=0 \qquad (2\text{-}63)$$

$$\frac{1}{r}\frac{1}{R}\frac{d}{dr}\left\{r\frac{\partial R}{\partial r}\right\} = -\frac{1}{Z}\frac{\partial^2}{\partial z^2}Z = -k^2 \qquad (2\text{-}64)$$

The equation (2-64) cannot solve itself. Thus, in order to solve differential equation, multiply to both r^2 sides, and if transposing left side to right side, the equation (2-64) is transformed to well-known form of Bessel differential equation.

$$\frac{1}{r}\frac{d}{dr}\left\{r\frac{\partial R}{\partial r}\right\} + k^2 R = 0 \qquad (2\text{-}65)$$ multiplying r^2 in both side, then

$$r^2 R'' + (k^2 r^2)R = 0 \qquad (2\text{-}66)$$

The solution of Bessel differentials is well-written in Engineering Mathematics textbooks, so this study only applies to the results. The solution of equation (2-65) is followed as equation (2-66). (Note that the solution of Bessel differential equation is the Bessel function)

$$C_1 J_0(\xi r) + C_2 Y_0(\xi r) \qquad (2\text{-}67)$$

Here the solution about Y_0 is going to divergent. So the only term of $C_n J_0(\xi r)$ has physical meaning. If composing differential equation about Z term in equation (2-64) which still does not be calculated, 2nd order homogeneous linear differential equation is derived (see eq. (2-68)), and the solution of that also well-define in the engineering mathematics textbook, so in this study only result is described, such as equation (2-69)

$$\frac{d^2}{dz^2}Z - k^2 Z = 0 \qquad (2\text{-}68)$$

$$D_1 e^{+\xi z} + D_2 e^{-\xi z} \qquad (2\text{-}69)$$

$$D_n \cdot \sinh(\xi z) \qquad (2\text{-}70)$$

Finally, in the case of a local force applied to the surface of the elastic body, the force to the longitudinal section direction can be expressed by Vector field potential method mathematically. And if it was defined $\varphi = R(r)Z(z)$ by the method of separation of variables, the solution could be Bessel function and hyperbolic sine function. The total sum of forces which elements are affected on Vector field would come into existence

when assuming the moment which affects to elements is zero. And the result of those is $\nabla^2\phi$.

2.3.3. Mathematical expression of local force on elastic body

In this chapter, mathematical express will be shown by using prepositional consideration about Vector field when force applied on local surface of elastic body and element. Equation (2-71) could be derived by Sturm-Liouville theory.

$$\int_0^\infty r \cdot \nabla^2 \phi \cdot J_0(\xi r) dr = 0 \qquad (2\text{-}71)$$

The *r* in the equation (2-71) represents the vector field of *r* direction on the surface of the elastic body and $\nabla^2 \phi$ refers to the force which element is affected in the field and $J_0(\xi r)$ refers to the Vector field in the direction of inside, in other words, longitudinal section, not the surface direction of elastic body. Where *r* performs the role of norm mathematically, that is, it is played as a *weighted function*, and makes the spatial vertical relationship by multiplying Bessel function (where space is not meant to be a 3-dimentional space, but it means a mathematical space that does not exist in the real world), so, it can be inferred that the results, zero can be derived from the form of an integral equation. The

equation (2-71) means the very thing of the indentation situation, and it is a mathematical description of the physical relationship between the wave of force to the each direction and force which element feel. The expression like the equation (2-71) can refer the fundamental writing of the theory of indentation. Figure 2.11 describes the meaning of the equation (2-71) more easily, and mathematical writing of Boussinesq's Problem. $\nabla^2\phi$ is a function of the effect that the elements is affected by force, and $J_0(\xi r)$ is a Bessel function. Here ξ means the force waves as a scaling factor and it represent the intensity of the force and the *r* is a independent variable of Bessel function. Researchers from various walks of life studied the solution of Boussinesq's Problem, and in this thesis, Sneddon's studies [2.3, 2.4] was noted, because it conforms to the instrumented indentation test results.

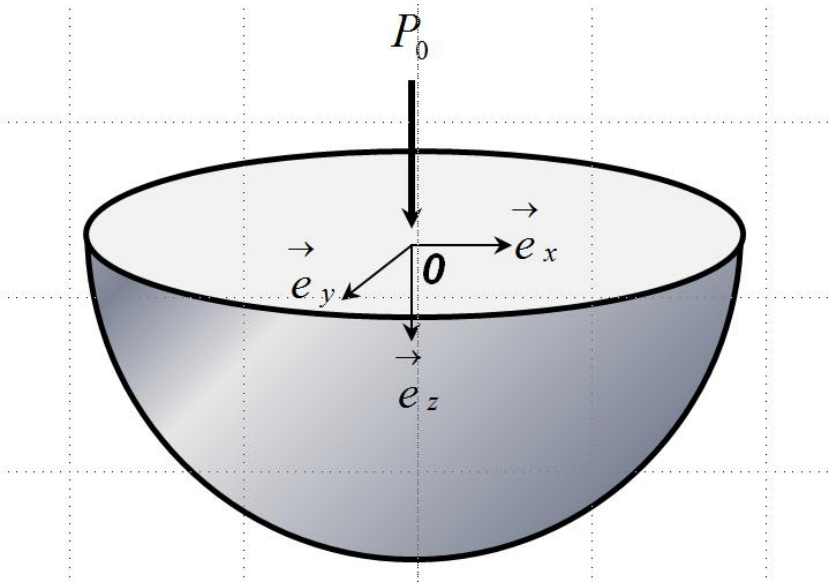

Figure 2.1. A semi-elastic body receiving a central force in its origin of surface

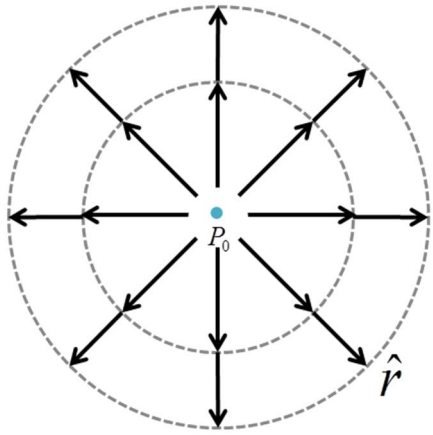

Figure 2.2. Pressure on local point (in polar coordinates)

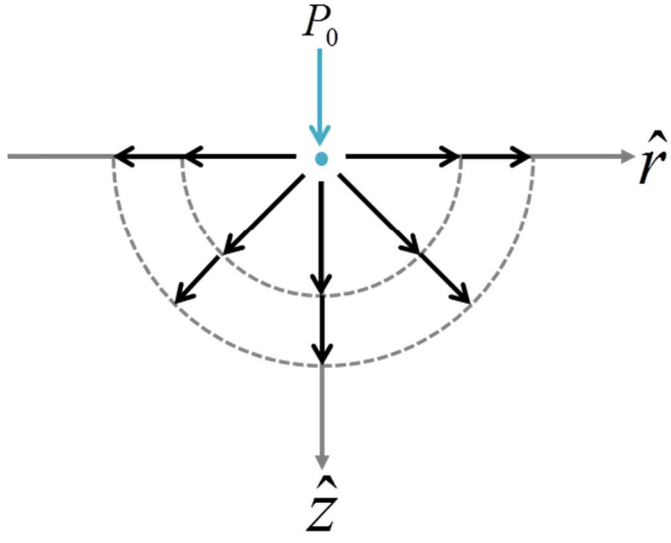

Figure 2.3. Pressure on local point (in Cartesian coordinates)

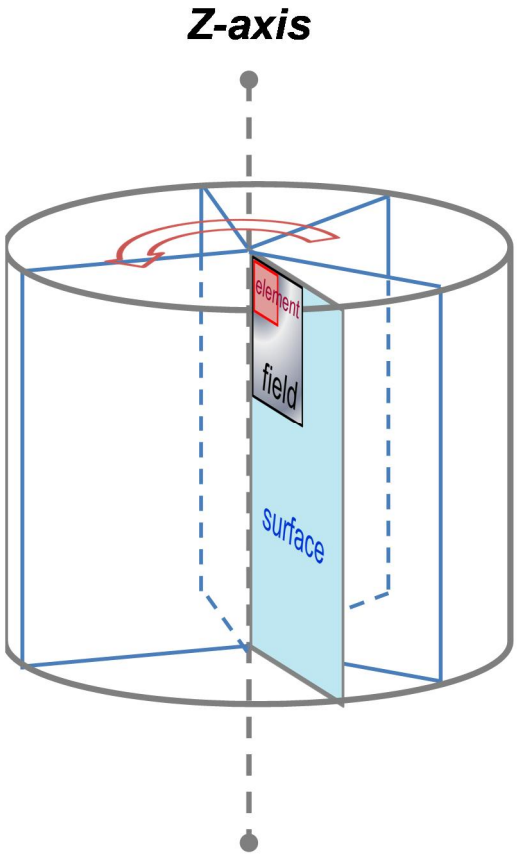

Figure 2.4. Behavior of axial-symmetric and setting element for the 2-dimensional plane

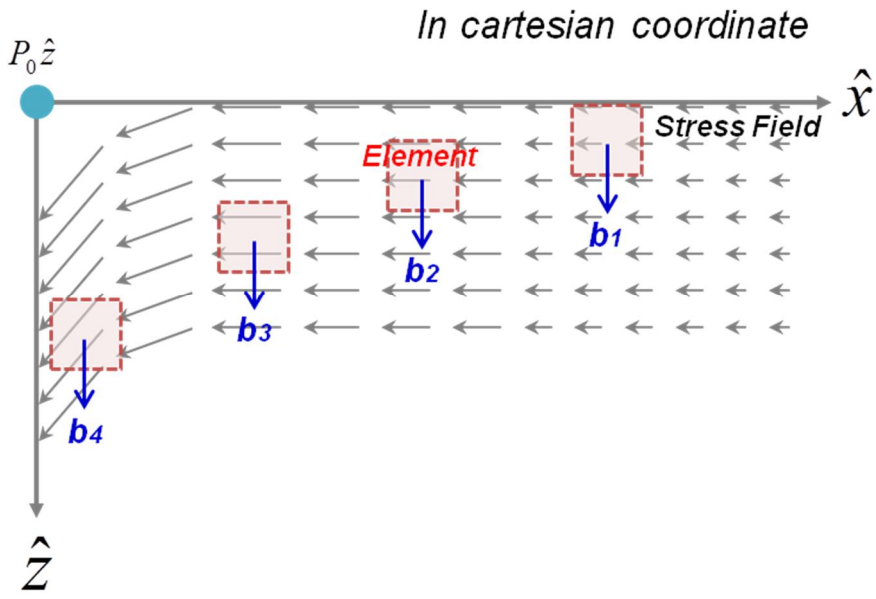

Figure 2.5. Variation of stress field and change of potential energy of Element

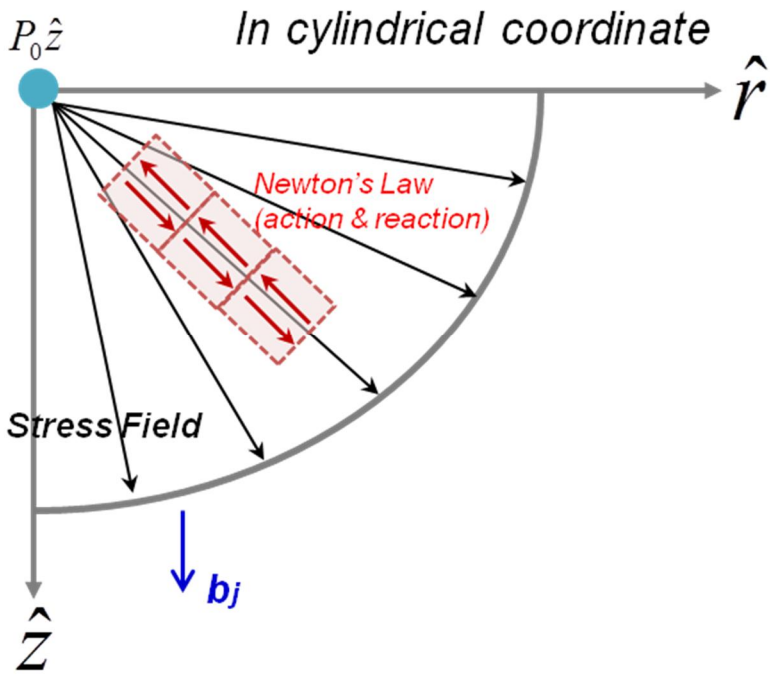

Figure 2.6. Concept of divergence theorem and internal aspects of element

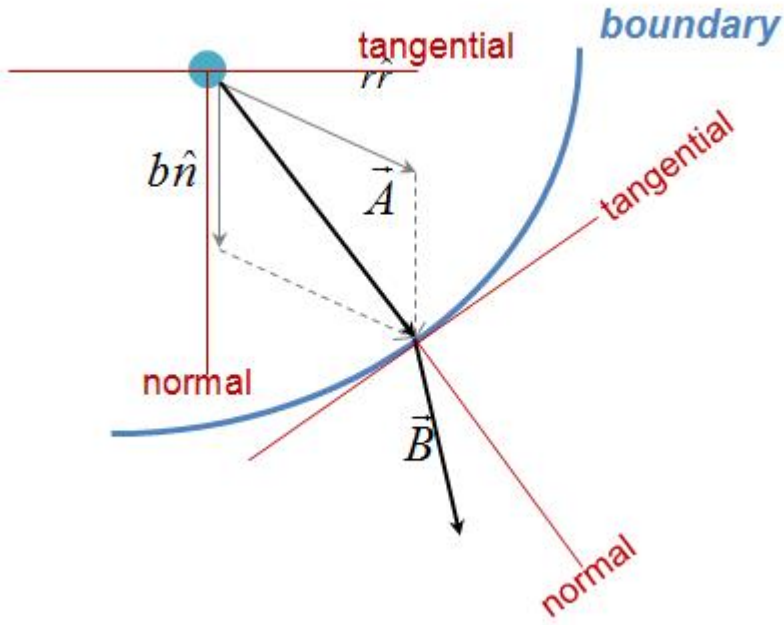

Figure 2.7. Boundary condition

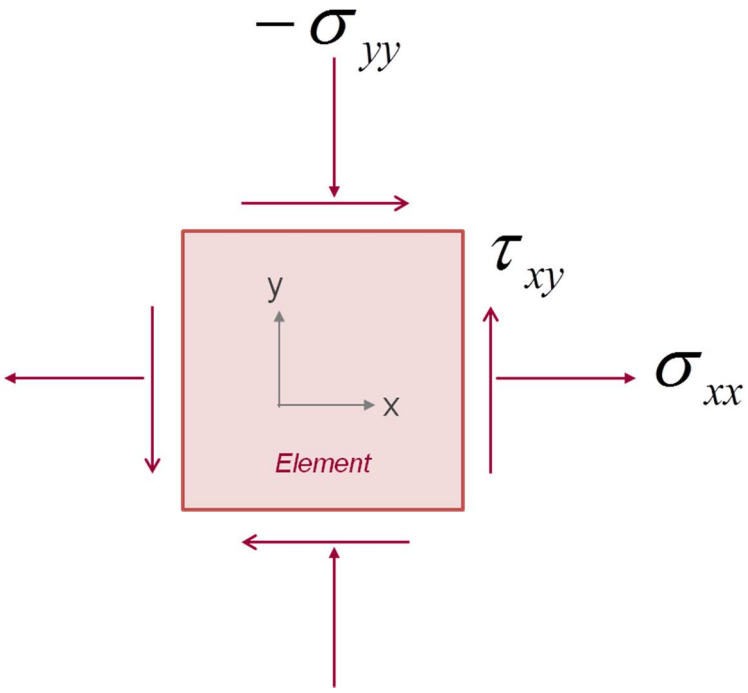

Figure 2.8. Element of 2D plane stress state

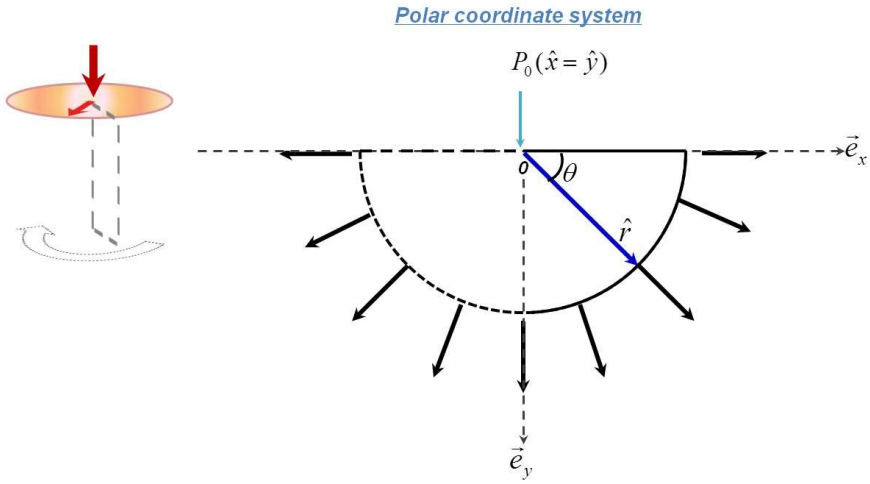

Figure 2.9. Vector analysis of surface

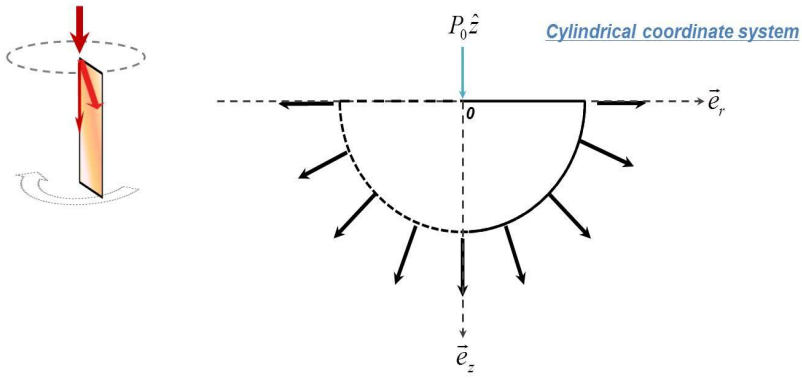

Figure 2.10. Vector analysis of longitudinal section

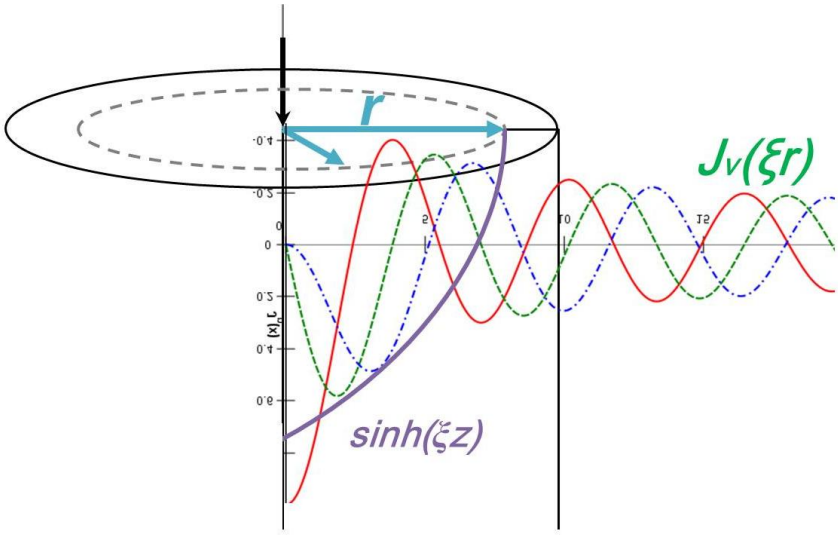

Figure 2.11. Fundamental of Indentation in elastic material

References

[2.1] Boussinesq, J. Applications des potentiels, Paris, 1885

[2.2] Allan F. Bower, Analytical techniques and solutions for linear elastic solid, Chapter 5, *Applied Mechanics of Solids*, CRC Press, 2009

[2.3] lan N. Sneddon; Boussinesq's problem for a rigid cone, *Mathematical Proceedings of the Cambridge Philosophical Society*, 44, (1948), 492-507

[2.4] J. W. Harding and I. N. Sneddon; The elastic stresses produced by the indentation of the plane surface of a semi-infinite elastic solid by a rigid punch, *Mathematical proceedings of the cambridge philosophical society*, 41, (1945), 16-26

Chapter 3

Exploring on Elastic Contact

Contents

3.1. The Solution of Boussinesq's Problem

This section is slightly modified version of the paper published in *Mathematical Proceedings of the Cambridge Philosophical Society* [Volume 41, Issue 01, June 1945, pp 16-26] by J. W. Harding and I. N. Sneddon, titled "The elastic stresses produced by the indentation of the plane surface of a semi-infinite elastic solid by a rigid punch".

To calculate the stress distribution applied to an elastic body, simply write down the equations outlined in the previous chapter, equilibrium equation acting on element (eq. 3-1), geometric compatibility equation (eq. 3-2), stress field equation (eq. 3-3), and boundary condition (eq. 3-4). Those equations constitute a set of engineering problem.

$$\nabla^2 \varphi = 0 \qquad \text{(3-1) Equilibrium equation for element}$$

$$\nabla\nabla\, \varphi = 0 \qquad \text{(3-2) Geometric Compatibility equation}$$

$$\int_0^\infty r \cdot J_0(\xi r) dr = 0 \qquad \text{(3-3) Stress field equation}$$

$$u_z = u_z(r), \quad 0 \le r \le a \qquad \text{(3-4) Boundary condition}$$

$$\sigma_z = 0, \quad (r > a)$$ (3-5) Boundary condition

$$\sigma_{rz} = \tau_{rz} = 0, \quad \forall r$$ (3-6) Boundary condition

The key to solving the above engineering problem is to use an integral transformation. Considering a large picture of solving process, equilibrium equation, compatibility equation and boundary condition would be converted using Fourier-Bessel Transformation (called Hankel Transformation) and in converted world the form of potential function would be determined and then, Potential function could have inversed form using inverse Fourier-Bessel Transformation (called Inverse Hankel Transformation), and then stress-strain distribution could be determined by using all results which performed above. The overall process for solution is shown in figure 3.1.

3.1.1. The elastic equations in cylindrical polar coordinates system

If material is assumed to semi-infinite elastic body, it deformed symmetrically with respect to the axis of revolution. It is therefore convenient to take the axis of revolution to be the z-axis, and employ polar coordinates r,θ to define the position of an element of the material in a plane normal to the axis. The stress components will be denoted by $\sigma_r,\sigma_\theta,\sigma_z,\tau_{\theta z},\tau_{zr},\tau_{r\theta}$ while the components of the displacement Vector will be taken as u_r,u_θ,u_z. If it assumed for the deformation to be symmetrical with respect to the z-axis, then $u_\theta,\tau_{\theta z},\tau_{r\theta}$ are all zero and the equation of equilibrium reduce to equation (3-7)

$$\frac{\partial\sigma_r}{\partial r}+\frac{\partial\tau_{rz}}{\partial z}+\frac{1}{r}(\sigma_r-\sigma_\theta)=0$$

$$\frac{\partial\tau_{rz}}{\partial r}+\frac{\partial\sigma_z}{\partial z}+\frac{\tau_{zr}}{r}=0 \qquad (3\text{-}7)$$

It is of advantage of express all the components of stress in terms of a single function, Φ. It may be verified by direct substitution that the equations of equilibrium are satisfied if equation (3-8) is taken.

$$\sigma_r = \lambda\nabla^2 \frac{\partial\Phi}{\partial z} - 2(\lambda+\mu)\frac{\partial^3\Phi}{\partial r^2\partial z}$$

$$\sigma_z = (3\lambda+4\mu)\nabla^2 \frac{\partial\Phi}{\partial z} - 2(\lambda+\mu)\frac{\partial^3\Phi}{\partial z^3}$$

$$\sigma_\theta = \lambda\nabla^2 \frac{\partial\Phi}{\partial z} - 2(\lambda+\mu)\frac{1}{r}\frac{\partial^2\Phi}{\partial r\partial z} \qquad (3\text{-}8)$$

$$\tau_{zr} = (\lambda+2\mu)\frac{\partial}{\partial r}\nabla^2\Phi - 2(\lambda+\mu)\frac{\partial^3\Phi}{\partial z^2\partial r}$$

Where Φ_{rrz} denotes $\partial^3\Phi/\partial r^2\partial z$, etc. it is then easily verified that the compatibility equation in cylindrical coordinates require that Φ shell be a solution of biharmonic equation like equation (3-9)

$$\nabla^4\Phi = 0 \qquad (3\text{-}9)$$

When, in the case of axial symmetry, ∇^2 can be defined in equation (3-10)

$$\nabla^2 \equiv \frac{\partial^2}{\partial r^2} + \frac{1}{r}\frac{\partial}{\partial r} + \frac{\partial^2}{\partial z} \qquad (3\text{-}10)$$

In the subsequent analysis, Components of displacement in the r, z are readily found to be equation (3-11) and (3-12)

$$u_r = -\frac{\lambda+\mu}{\mu}\frac{\partial^2\Phi}{\partial r\partial z} \tag{3-11}$$

$$u_z = \frac{\lambda+2\mu}{\mu}\nabla^2\Phi - \frac{\lambda+\mu}{\mu}\frac{\partial^2\Phi}{\partial z^2} \tag{3-12}$$

3.1.2. The transformation of the biharmonic equation to an ordinary differential equation

By applying the method of Hankel transformation, biharmonic equation can be reduce in the two independent variables r, z, the place of the variable r being taken by a parameter. The boundary condition must then be treated in the same way, so that instead of having relations concerning partial derivatives with respect to r and z, relations are obtained between the derivatives of an auxiliary function in the sigle variable z. As the result of a series of integration by parts, equation (3-13) can be obtained.

$$\int_0^\infty r\nabla^4\Phi J_0(\xi r)dr = \left(\frac{d^2}{dz^2} - \xi^2\right)^2 \int_0^\infty r\Phi J_0(\xi r)dr \qquad (3\text{-}13)$$

The left side of equation (3-13) is the result of considering the compatibility of the equation described in the lead equation (3-38), the right side of equation (3-13) is the result derived from the exception of satisfying of Cauchy-Euler differential equation. Here the left side meets the Laplace equation again, so if considering quadratic term, the result is zero, the right side would be a multiplied form by which integration equation multiplies to location part, where ξ is the constant containing the magnitude of the waves in Bessel equation.

The equation (3-14) is a definition of Hankel transformation, and the equation (3-15) can be derived by Hankel transformation of integral part of equation (3-13)

$$H\{\varphi(r)\} = \int_0^\infty r \cdot \varphi(r) \cdot J_v(\xi r) \cdot dr = G(\xi) \qquad (3\text{-}14)$$

$$\left(\frac{d^2}{dz^2} - \xi^2\right)^2 G(\xi) = 0 \qquad (3\text{-}15)$$

By performing transformation, a complex equation (3-13) can be converted into a simple differential equation, such as equation (3-15). Now let's deploy square term in equation (3-15) and after multiplying *G* function, and if (d^2G/dz^2) replaces into *U*, the equation (3-13) can be defined as the ordinary differential equation like well-known equation (3-16)

$$U'' - 2\xi^2 U + \xi^4 = 0 \qquad (3\text{-}16)$$

$$G = (A + Bz)e^{\xi z} + (C + Dz)e^{-\xi z} \qquad (3\text{-}17)$$

Now, the problem is thus reduced to a boundary value problem for the ordinary differential equation, the treatment of which is much simpler than is that of the corresponding problem for partial differential equation (eq. 3-9, $\nabla^4\Phi = 0$). The general solution of equation (3-16) is equation (3-17). Among the undetermined coefficients, *A*, *B*, *C*, *D*, the coefficient *A* and *B* need not consider, because $e^{\xi z}$ will be divergent. The meaning coefficient is *C* and *D*, where the arbitrary constants *C*, *D* which will in general be function of ξ are to be determined from the imposed boundary condition. Once these constants have been determined, *G* is known as a function of *z* and of the parameter ξ. The expression for potential function Φ may then be obtained directly from inverse transformation of Hankel theorem. Therefor potential function is given like equation (3-19) and equation (3-18) is definition of Inverse Hankel transformation.

$$H^{-1}\{G(\xi)\} = \int_0^\infty \xi \cdot G(\xi) \cdot J_v(\xi r) \cdot d\xi = \varphi(r) \qquad (3\text{-}18)$$

$$\Phi = \int_0^\infty \xi \cdot G \cdot J_0(\xi r) \cdot d\xi \qquad (3\text{-}19)$$

$$G = (C + Dz)e^{-\xi z} \qquad (3\text{-}20)$$

3.1.3. The boundary conditions and corresponding integral equations

The first boundary condition to know the undetermined coefficient C and D is equation (3-6) stated above. With the Hankel transformated boundary condition, the coefficient *C* and *D* have relations with following equation (3-21). And *G* function can be decided if equation (3-21) is put into equation (3-20). Hence, *G* like a equation (3-22) can be expressed as a function of *D* only which contains undetermined coefficient.

$$(\lambda + \mu)C = \xi\lambda D \tag{3-21}$$

$$G = \frac{D}{\xi}\left[\frac{\lambda}{\lambda + \mu} + \xi z\right]e^{-\xi z} \tag{3-22}$$

Where λ, μ is Lame's constant and defined in equation (3-23) and equation (3-24), ν, E mean poisson's ratio and elastic modulus

$$\lambda = \frac{vE}{(1+v)(1-2v)} \tag{3-23}$$

$$\mu = \frac{E}{2(1+v)} \tag{3-24}$$

If using other boundary conditions, equation (3-4) and equation (3-5) which also transformed by Hankel theorem, put them into equation (3-8), previously mentioned, which also transformed by Hankel theorem, then it is possible to obtain strain(eq. 3-25) and stress(eq. 3-26) on the z direction.

$$u_z(r) = -\frac{\lambda + 2\mu}{\mu}\int_0^\infty \xi^2 D J_0(\xi r) d\xi, \qquad 0 \le r \le a \tag{3-25}$$

$$\sigma_z = \int_0^\infty \xi^3 D J_0(\xi r) d\xi = 0, \qquad r \le a \tag{3-26}$$

What matter here is the Bessel function $J_0(\xi r)$, As shown in Figure 3.2, the value of the Bessel function characteristically may have a several zero. So when $r = a$, that is, when the condition $\sigma_{rz} = 0$ is satisfied, $J_0(\xi r)$ can be converted into $J_0(\xi a)$, at the same time if ξa was defined to *K* newly, it could be $\xi = K / a$. So finally ξ can be expressed as parameters r, a of indentation test. A series of processes mentioned above were shown in equation (3-27), (3-28), and (3-29)

$J_0(\xi r)$ (3-27) *when* $(r = a)$, $\sigma_{rz} = 0$

$$J_n(\xi a) = J_0(\xi r) = 0 \qquad (3\text{-}28) \quad k = \xi a, \quad \xi = \frac{k}{a}$$

$$J_0(\xi r) = J_0(k\frac{r}{a}) \qquad (3\text{-}29)$$

Now, wait a second, let's consider again equation (3-25) and equation (3-26). As mentioned earlier, equation (3-25) and (3-26) respectively, the Hankel transformed shape of equation (3-8) according to z-axis. For example, the stress in the z direction is as follows:

$$\sigma_z = (3\lambda + 4\mu)\nabla^2 \frac{\partial \Phi}{\partial z} - 2(\lambda + \mu)\frac{\partial^3 \Phi}{\partial z^3} \qquad (3\text{-}8)$$

Conducting equation (3-8) to Hankel transformation then,

$$\sigma_z = \int_0^\infty \xi^3 D J_0(\xi r) d\xi = 0, \quad r \le a \qquad (3\text{-}26)$$

Because parameters that make equation (3-25) and (3-26) cannot be obtained by a instrumented indentation test, ξa replaces to *K* with the equation (3-27), (3-28), and (3-29) which mentioned in preceding chapter, and replacing

$-\frac{\mu a^4}{\lambda+2\mu}[u_z(r)]_{z=0}$ contained in displacement term (eq. 3-25) with $g\left(\frac{r}{a}\right)$, replacing $\xi^2 D$ with $f(K)$, and deploying equations, the equation (3-28) and (3-29) become to equation (3-30) and (3-31).

$$u_z(r)=\int_0^\infty f(k)J_0(k\frac{r}{a})dk=g\left(\frac{r}{a}\right),\qquad 0\le\frac{r}{a}\le 1 \tag{3-30}$$

$$\sigma_z=\int_0^\infty kf(k)J_0(k\frac{r}{a})dk=0,\qquad \frac{r}{a}>1 \tag{3-31}$$

3.2. The Solution of Integral Equation

Dual integral equation of the type mentioned above in equation (3-30) and (3-31) have been considered by Titchmarch[3.1] and Busbridge[3.2]. It was shown by the latter that the solution of these equatios could be put in the form like equation (3-32).

$$f(k)=\frac{2}{\pi}\cos r\int_0^1 y(1-y^2)^{-1/2}g(y)dy+\frac{2}{\pi}\int_0^1 y(1-y^2)^{-1/2}dy\int_0^1 g(yu)ru\sin(ru)du \quad (3\text{-}32)$$

In the particular case in which using the theory of superposition following equation 3-32.

$$g(\frac{r}{a})=\sum_n A_n(\frac{r}{a})^n \quad (3\text{-}33)$$

The coefficient A_n being constant, it is easily found that the equation (3-33) reduce to equation (3-34)

$$f(k)=\frac{1}{\sqrt{\pi}}\sum_{n}\frac{\Gamma\left(\frac{1}{2}n+1\right)}{\Gamma\left(\frac{1}{2}n+\frac{3}{2}\right)}A_n\left\{\cos k+k\int_0^1 u^{n+1}\sin(ku)du\right\} \qquad (3\text{-}34)$$

The equation (3-34) is a mathematical method in which the Titchmarsh and Busbridge designed to solve the dual integration problem. It has a characteristic that complexity of Bessel function is disappear instead it is represented by Gamma function which means foundation of Bessel function. And the equation (3-34) can be developed like Fourier series by put constant 1, 2, 3…… into *n* variable. Using a appropriate notation, equation (3-34) can change the form with the following equation (3-35). And equation (3-35) may indicate the compositions of stress and strain in elastic body.

$$I_n^m=\int_0^\infty k^n\cdot f(k)\cdot e^{-k\xi}J_m(k\frac{r}{a})dk \qquad (3\text{-}35)$$

Therefor using equation (3-35), complex Bessel function $J_n(\xi r)$ of equation (3-8), (3-11), and (3-12) can be expressed in notation about I_n^m. And these are general solution for the stress and strain components of elastic body as followed in equation (3-36) ~ (3-41)

$$\sigma_z = \frac{2(\lambda+\mu)}{a^5}\left[I_1^0 + \xi I_2^0\right] \tag{3-36}$$

$$\sigma_\theta = \frac{2\lambda}{a^5} I_1^0 + \frac{2\mu}{(\frac{r}{a})a^5}\left[I_0^1 - \frac{\lambda+\mu}{\mu}\xi I_1^1\right] \tag{3-37}$$

$$\tau_{zr} = \frac{2(\lambda+\mu)}{a^5}\xi I_2^1 \tag{3-38}$$

$$\sigma_r + \sigma_\theta = \frac{2}{a^5}\left[(2\lambda+\mu)I_1^0 - (\lambda+\mu)\xi I_{21}^0\right] \tag{3-39}$$

$$u_r = \frac{1}{a^4}\left[I_0^1 - \frac{\lambda+\mu}{\mu}\xi I_1^1\right] \tag{3-40}$$

$$u_z = -\frac{1}{a^4}\left[\frac{\lambda+2\mu}{\mu} I_0^0 + \frac{\lambda+\mu}{\mu}\xi I_1^0\right] \tag{3-41}$$

Summarizing again the above sequence of processes, $f(k)$ suggested by Titchmarsh and Busbridge is a function that is dominated by displacement. In other words, it means that any geometric deformation can produce stress and strain if displacement model is well established. λ and μ are Lame's

constant, and those parameters are dominated in elastic constitute equation if material is elastic body, or are dominated in elastoplastic constitute equation if material is elastoplastic body. I_n^m is a kind of natation which is irrelevant to material, namely, it is an independent parameter which describes the deformation and movement of element in the field and corresponding change of field of it. Biharmonic equation ($\nabla^2\Phi$) which explains the force affected to element, was converted into $f(k)$, and in addition, I_n^m is what is considered beyond element. Figure 3.3 shows a series of process for solution. At first, the set of problems was given the equilibrium equation, field equation, and boundary conditions. Then, to solve biharmonic equation, 4order differential equation is converted by Hankel transformation and Inverse Hankel transformation, and derived it to *G* function. And next, using boundary condition, *G* function is converted to *D* function. And it is converted properly having a physical indentation variables, instead of being abstract and difficult to measure variables. And next using the method of Titchmarsh and Busbridge, finally, it is known that all stress and strain component can be derived.

3.3. Application to Conical Punch

In the case where the deforming rigid body is a circular cone with an assumption, as in the previous analysis, that the axis of the cone coincides with z-axis, the vertex pointing downwards into the interior of the elastic body. the strained surface of the elastic body will be assumed to fit the cone over the area between the vertex of the cone and a circular section of radius *a*, as shown figure 3.5, for the z-component of the displacement is followed as equation (3-42)

$$\left[u_z(r)\right]_{z=0} = b + \varepsilon(1 - \frac{r}{a}) \qquad (z=0,\ 0<r<a) \qquad (3\text{-}42)$$

And where initial condition are followed

$$\left[\sigma_z(r)\right]_{z=0} = 0 \qquad (z=0,\ r>a) \qquad (3\text{-}42)$$

$$\left[\tau_{rz}(r)\right]_{z=0} = 0 \qquad (z=0,\ r\geq a) \qquad (3\text{-}42)$$

Where, as before, *a* is a circular section of radius, *b* is a parameter as yet undetermined. In the notation from the equation (3-25) ~ (3-29), the equation (3-42) can be re-written as equation (3-43)

$$u_z(r,0) = b + \varepsilon - \varepsilon(\frac{r}{a}) \qquad (z=0,\ 0<r<a) \qquad (3\text{-}43)$$

Where $(b+\varepsilon)$ can be replaced as A, and $(-\varepsilon)$ can be replaced as B, then equation (3-43) will be changed as equation (3-44).

$$g(\frac{r}{a}) = A + B(\frac{r}{a}) \qquad (3\text{-}44)$$

Where $A = -\frac{\mu}{\lambda+2\mu}a^4(b+\varepsilon)$ and $B = \frac{\mu}{\lambda+2\mu}a^4\varepsilon$

Putting $n=0$, $A_0 = A$, $n=1$, $A_1 = B$ into equation (3-34) mentioned previous chapter.

$$f(k) = \frac{1}{\sqrt{\pi}}\sum_n \frac{\Gamma\left(\frac{1}{2}n+1\right)}{\Gamma\left(\frac{1}{2}n+\frac{3}{2}\right)}A_n\left\{\cos k + k\int_0^1 u^{n+1}\sin(ku)du\right\} \qquad (3\text{-}34)$$

The equation (3-34) can have the form of equation (3-45)

$$f(k) = 2\left(\frac{A}{\pi}+\frac{B}{2}\right)\frac{\sin k}{k} + B\frac{\cos k - 1}{k^2} \qquad (3\text{-}45)$$

Steps up to equation (3-45) are meant that first initial condition is used for potential function $f(k)$. Now let's use the second initial condition. The normal component of stress σ_z at the surface of the elastic body $z=0$ was shown previous chapter as the equation (3-36) and the notation also defined as the equation (3-35)

$$\sigma_z = \frac{2(\lambda+\mu)}{a^5}\left[I_1^0 + \xi I_2^0\right] \qquad (3\text{-}36)$$

$$I_n^m = \int_0^\infty k^n \cdot f(k) \cdot e^{-k\xi} J_m(k\frac{r}{a})dk \qquad (3\text{-}35)$$

If second initial condition, $\sigma_z(r,0)=0 \quad z=0, r \geq a$, and equation (3-45) are used into equation (3-35) then equation (3-46) is derived.

$$\frac{a^5}{2(\lambda+\mu)}\sigma_z(r)_{z=0,r/a=1} = 2\left(\frac{A}{\pi}+\frac{B}{2}\right)\int_0^\infty k\frac{\sin k}{k}J_0(k\frac{r}{a})dk - B\int_0^\infty k\frac{1-\cos k}{k^2}J_0(k\frac{r}{a})dk$$

(r=a) (3-46)

The normal stress, σ_z must, on physical grounds, remain finite round the circle $\frac{r}{a}=1$, but the former of the two integrals is divergent. Hence in order that σ_z may remain finite, so the term $\frac{A}{\pi}+\frac{B}{2}$ of equation (3-46) should be taken to zero. So equation (3-47) is derived.

$$\frac{A}{\pi}+\frac{B}{2}=0 \qquad (3\text{-}47)$$

Inserting the values of *A* and *B* defined above, the relation is equivalent to the condition $b=\varepsilon\left(\frac{1}{2}\pi-1\right)$, which fixed the value of the parameter b; this is in agreement with the expression obtained otherwise by Love[3.3]. Thus function of $f(k)$ can be obtained as equation (3-48)

$$f(k)=B\frac{\cos k-1}{k^2} \qquad (3\text{-}48)$$

The equation (3-48) will be used later in the step of determination of σ_z.

Now let's consider again about displacement from equation (3-43)

$$u_z(r,0)=b+\varepsilon-\varepsilon(\frac{r}{a}) \qquad (z=0,\ 0<r<a) \qquad (3\text{-}43)$$

As defined above, $A = b + \varepsilon$, $B = -\varepsilon$, and a condition $b = \varepsilon\left(\frac{1}{2}\pi - 1\right)$, the displacement equation of z-direction (eq. 3-43) can be rewritten as equation (3-49) and (3-50)

$$u_z(r,0) = \varepsilon\left(\frac{\pi}{2} - 1\right) + \varepsilon\left(1 - \frac{r}{a}\right) \quad (z=0,\ 0<r<a) \tag{3-49}$$

$$u_z(r) = \varepsilon\left(\frac{\pi}{2} - \frac{r}{a}\right) \quad (z=0,\ 0<r<a) \tag{3-50}$$

As shown in Figure 3.8, the variables, b, ε, u_z, can also be defined easily by geometrically. $b = \varepsilon\left(\frac{1}{2}\pi - 1\right)$, $\varepsilon = a\cot\theta$, and $u_z(r) = \varepsilon\left(\frac{\pi}{2} - \frac{r}{a}\right)$. So the equation (3-51) is derived by combination of these variables.

$$u_z(r) = \left(\frac{\pi}{2} - \frac{r}{a}\right) a\cot\theta \tag{3-51}$$

θ can regard to be a constant. Because, in conical punch, the shape of punch is determined beforehand to make and it means the angle of punch can be known previously. And indentation displacement depends on variable '*a*' which

contains contact area with punch and surface of elastic body. The contact area and displacement are proportional to each other.

Now Let's start by substituting equations (3-35), (3-48) and condition, $b = \varepsilon\left(\frac{1}{2}\pi - 1\right)$, and definition $\varepsilon = a\cot\theta$ into the equation (3-36) in order to obtain stress component of z-direction more specifically. Then the equation (3-52) can be derived.

$$I_n^m = \int_0^\infty k^n \cdot f(k) \cdot e^{-k\xi} J_m(k\frac{r}{a})dk \qquad (3\text{-}35)$$

$$f(k) = B\frac{\cos k - 1}{k^2} \qquad (3\text{-}48)$$

$$\sigma_z = \frac{2(\lambda+\mu)}{a^5}\left[I_1^0 + \xi I_2^0\right] \qquad (3\text{-}36)$$

$$\left(\frac{\lambda+2\mu}{2\mu(\lambda+\mu)}\right)\sigma_z(r)_{z=0} = 2\frac{\varepsilon}{a}\int_0^\infty \frac{\cos k - 1}{k} J_0(k\frac{r}{a})dk \qquad (3\text{-}52)$$

In the equation (3-52) which also means stress component on boundary plane *z=0*, the left side can be solved by Lame's constant theory as defined equation (3-53) ~ (3-56)

$$\lambda = \frac{\upsilon E}{(1+\upsilon)(1-2\upsilon)} \qquad (3\text{-}53)$$

$$\mu = G = \frac{E}{2(1+\upsilon)} \qquad (3\text{-}54)$$

$$\lambda + 2\mu = \frac{2\mu(1-\upsilon)}{1-2\upsilon} \qquad (3\text{-}55)$$

$$\lambda + \mu = \frac{E}{2(1+\upsilon)(1-2\upsilon)} \qquad (3\text{-}56)$$

Then, the term $\left(\frac{\lambda + 2\mu}{2\mu(\lambda+\mu)}\right)$ of equation (3-52) can be given as equation (3-57), and rewritten as equation (3-58).

$$\frac{2(1-\upsilon^2)}{E} \qquad (3\text{-}57)$$

$$\frac{2(1-\nu^2)}{E}\sigma_z(r)_{z=0} = 2\frac{\varepsilon}{a}\int_0^\infty \frac{\cos k - 1}{k} J_0(k\frac{r}{a})dk \qquad (3\text{-}58)$$

By using Fourier-Bessel series, the term, $\int_0^\infty \frac{\cos k - 1}{k} J_0(k\frac{r}{a})dk$,of right side of equation (3-58) can be converted to $-\cosh^{-1}\left(\frac{a}{r}\right)$ when satisfying the condition $0 < r < a$, and if $r > a$, the value of $\int_0^\infty \frac{\cos k - 1}{k} J_0(k\frac{r}{a})dk$ is zero. And if $a > r$, then $-\cosh^{-1}\left(\frac{a}{r}\right)$ is $\ln\left[\left(\frac{a}{r}\right)+\sqrt{\left(\frac{a}{r}\right)^2 - 1}\right]$. So finally the equation (3-58) can be deduced as equation (3-59).

$$\sigma_z(r)_{z=0} = -\frac{E}{2(1-\nu^2)}\frac{\varepsilon}{a}\cosh^{-1}\frac{a}{r} \qquad 0 < r < a \qquad (3\text{-}59)$$

Then, the total pressure P_m on the pressed area $0 < r < a$ is given gy equation (3-60)

$$P_m = -2\pi\int_0^a r[\sigma_z]_{z=0}dr \qquad (3\text{-}60)$$

Substituting equation (3-59) into equation (3-60), then the relationship between local pressure and displacement is shown as the equation (3-61)

$$P_m = \frac{\pi E}{2(1-\nu^2)} a\varepsilon = \frac{E}{2(1-\nu^2)} \pi a^2 \cot\theta = \frac{2\tan\theta}{\pi(1-\nu^2)} E\varepsilon^2 \quad (3\text{-}61)$$

$$P = \frac{2\tan\theta}{\pi(1-\nu^2)} Eh^2 \quad (3\text{-}62)$$

where P is the load measured by the indenter, E and ν are the Young's modulus and Poisson's ratio of the material that is being indented, α is the half angle of the indenter, and $h(=\varepsilon)$ is the displacement of the indenter.

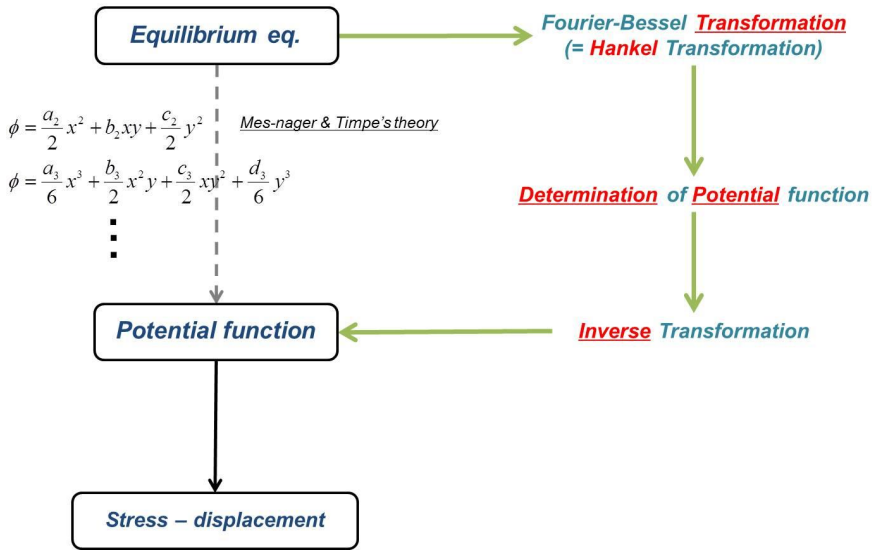

Figure 3.1. Strategy for solution

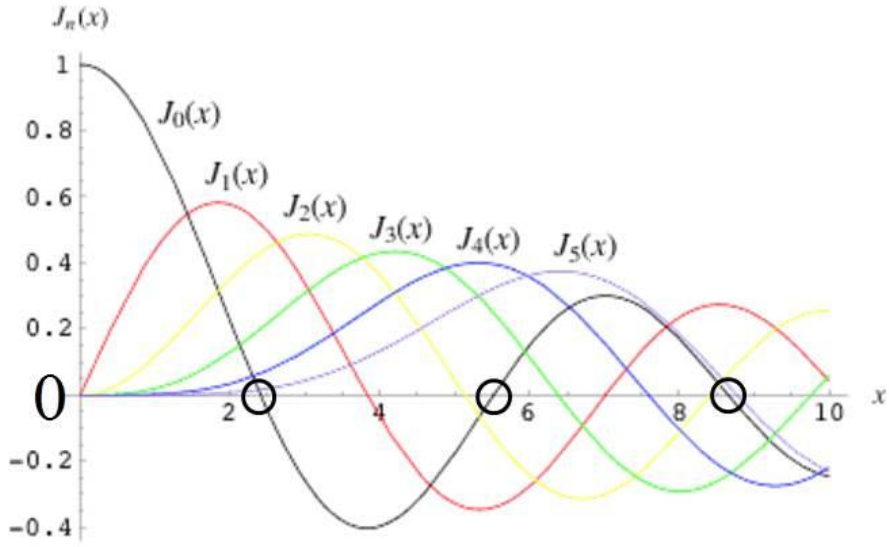

Figure 3.2. Bessel function

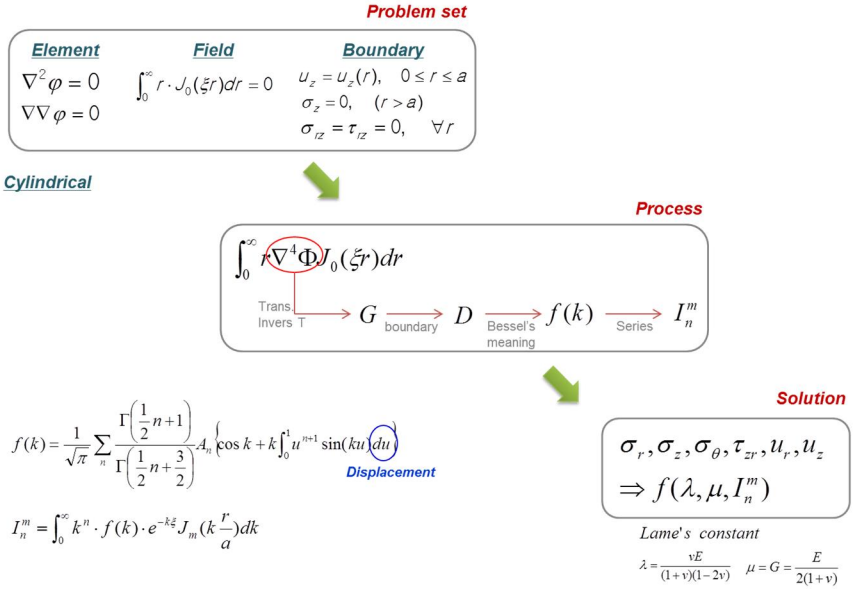

Figure 3.3. Process to solve the dual integral equation

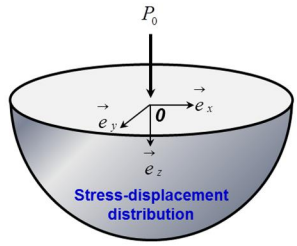

$$f(k)=\frac{1}{\sqrt{\pi}}\sum_n \frac{\Gamma\left(\frac{1}{2}n+1\right)}{\Gamma\left(\frac{1}{2}n+\frac{3}{2}\right)}A_n\left\{\cos k+k\int_0^u u^{n+1}\sin(ku)du\right\}$$

$$I_n^m=\int_0^\infty k^n\cdot f(k)\cdot e^{-k\xi}J_m(k\frac{r}{a})dk$$

General solution

$$\sigma_z=\frac{2(\lambda+\mu)}{a^5}\left[I_1^0+\xi I_2^0\right] \qquad u_r=\frac{1}{a^4}\left[I_0^1-\frac{\lambda+\mu}{\mu}\xi I_1^1\right]$$

$$\sigma_\theta=\frac{2\lambda}{a^5}I_1^0+\frac{2\mu}{(\frac{r}{a})a^5}\left[I_0^1-\frac{\lambda+\mu}{\mu}\xi I_1^1\right] \qquad u_z=-\frac{1}{a^4}\left[\frac{\lambda+2\mu}{\mu}I_0^0+\frac{\lambda+\mu}{\mu}\xi I_1^0\right]$$

$$\tau_{zr}=\frac{2(\lambda+\mu)}{a^5}\xi I_2^1$$

$$\sigma_r+\sigma_\theta=\frac{2}{a^5}\left[(2\lambda+\mu)I_1^0-(\lambda+\mu)\xi I_{21}^0\right]$$

Figure 3.4. Stress-displacement distribution

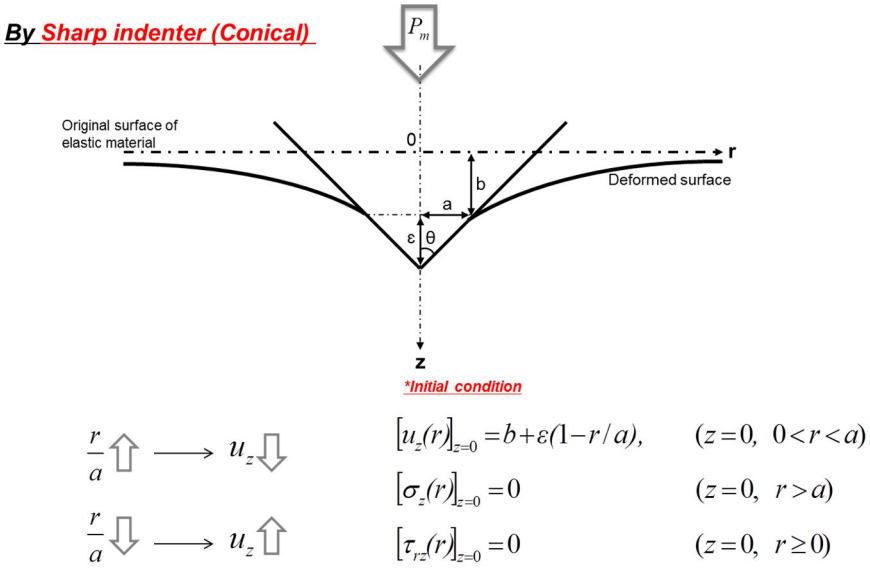

Figure 3.5. Geometric condition of indentation

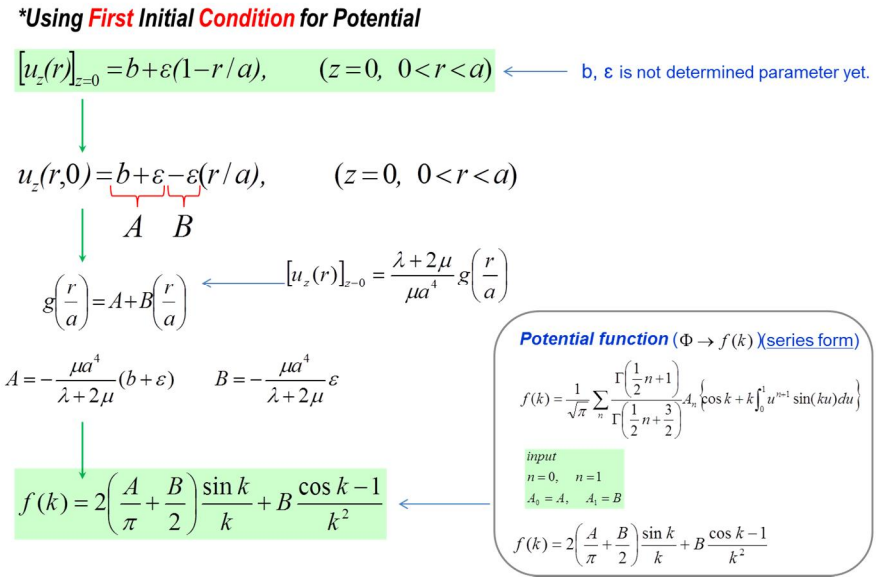

Figure 3.6. Determination of potential function by displacement

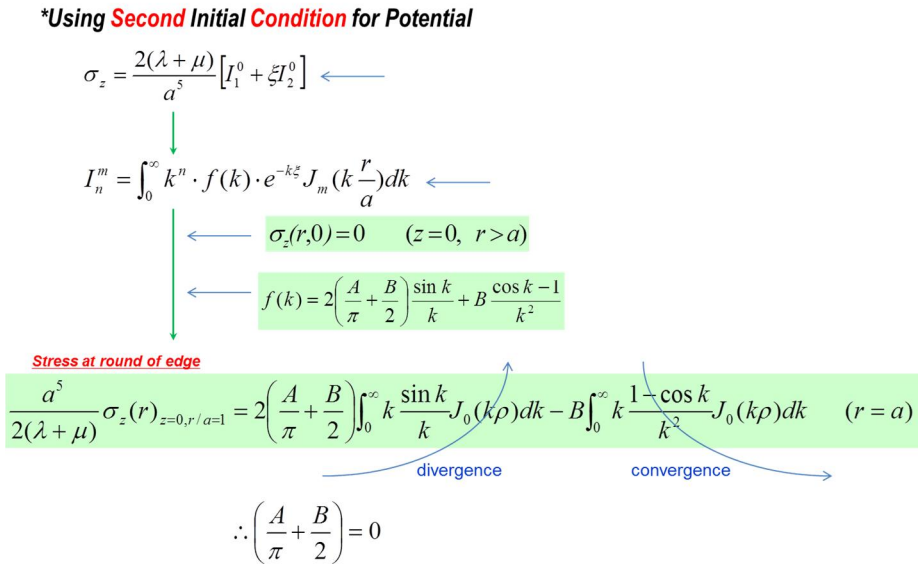

Figure 3.7. Determination of potential function by stress

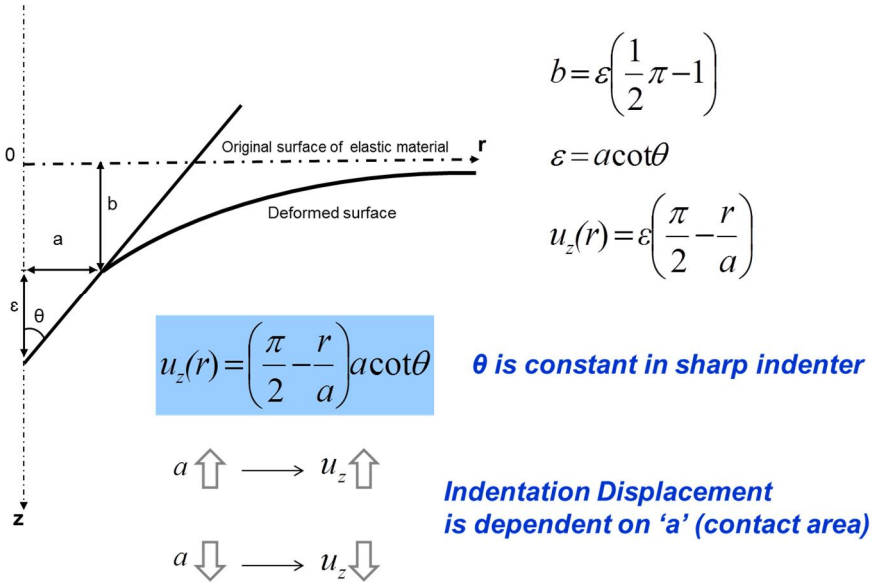

Figure 3.8. Determination of Displacement by geometric relation

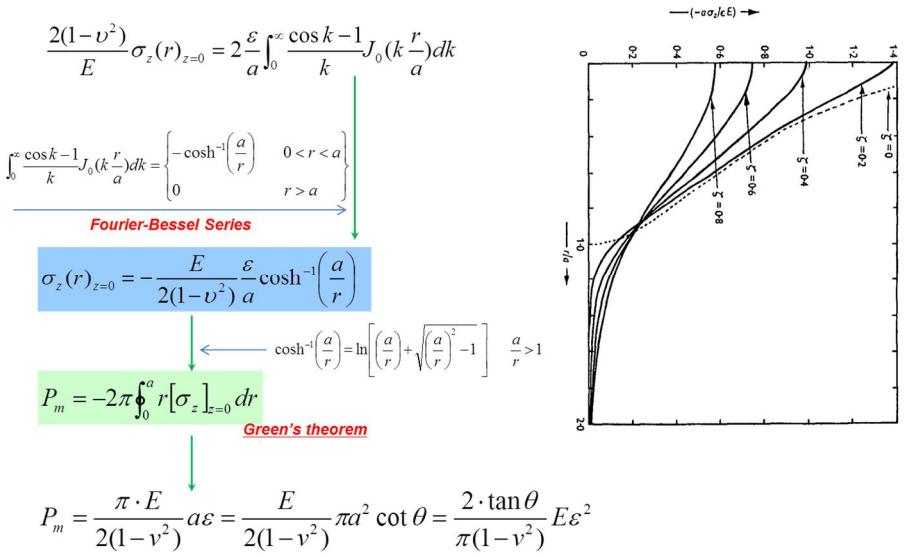

Figure 3.9. Determination of Z-direction Stress

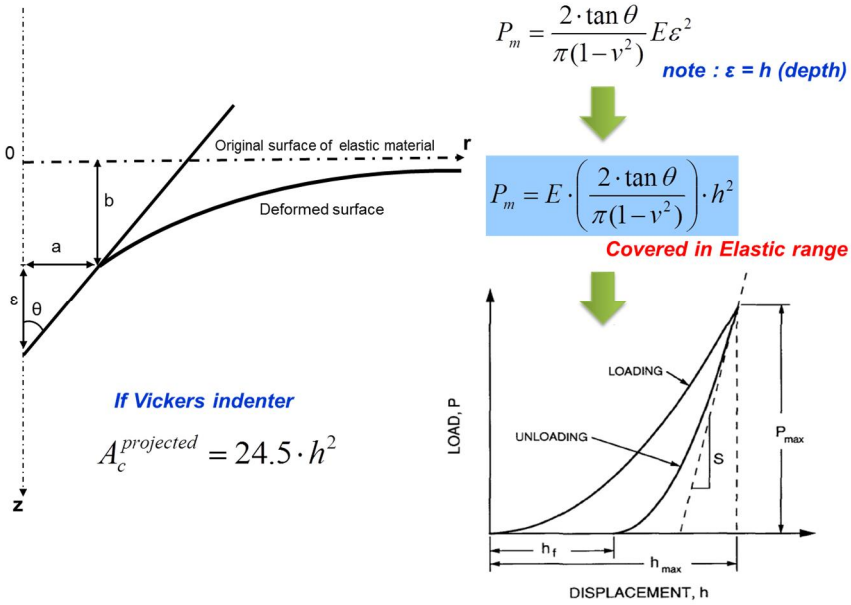

Figure 3.10. Relation load-displacement in indentation in elastic range

References

[3.1] Titchmarsh, E. C. An introduction to the theory of Fourier integrals (*Oxford*, 1937), p334.

[3.2] Busbridge, I. W. *Proc. London Math. Soc*. (2), 44 (1938), 115-30

[3.3] Love, A. E. H. *Quart. J. Math*. 10, (1939), 161

Chapter 4

Exploring on Elastic-Plastic Contact

Contents

4.1. Slip-line field theory

In the slip-line field solution, developed originally in two dimensions by Hill, Lee, and Tupper [4.1], the volume of material displaced by the indenter is accounted for by upward flow, as shown in Fig. 4.1.

The material in the region ABCDE flows upward and outward as the indenter moves downward under load. Because frictionless contact is assumed, the direction of stress along the line AB is normal to the face of the indenter. The lines within the region ABDEC are oriented at 45° to AB and are called slip lines(lines of maximum shear stress). This type of indentation involves a cutting of the specimen material along the line OA and the creation of new surfaces that travel upward along the contact surface.The contact pressure across the face of the indenter is given by

$$p_m = 2\tau_{\max}(1+\alpha) = H, \qquad (4\text{-}1)$$

where τ_{max} is the maximum value of shear stress in the specimen material and α is the cone semi-angle (in radians).

Invoking the Tresca shear stress criterion, where plastic flow occurs at $\tau_{max} = 0.5\sigma_y$, and substituting into Eq. (4-1) gives

$H = \sigma_y(1+\alpha)$, where $\psi = (1+\alpha)$. (4-2)

The constraint factor determined by this method is referred to as ψ_{flow}. For values of between 70°and 90°, Eq. (4-2) gives only a small variation in ψ_{flow} of 2.22 to 2.6. Friction between the indenter and the specimen increases the value of ψ_{flow}. A slightly larger value for ψ_{flow} is found when the von Mises stress criterion is used (where $\tau_{max} \approx 0.58\sigma_y$). For example, at $\alpha = 90°$, Eq. (4-2) with the von Mises criterion gives $\psi = 3$.

4.2. Expanding Cavity Model

Johnson [4.2, 4.3] postulated that the analysis for the expansion of a spherical cavity in an elastic-plastic material could be applied to the hemispherical radial mode of deformation observed in indentation tests by replacing the cavity with an incompressible, hemispherical core of material directly beneath the indenter of radius equal to the contact circle. Surrounding the core is a hemispherical plastic zone, which connects with the elastically strained material at some larger radius c. As shown in Fig. 4.2, penetration of the indenter causes material particles at the outer boundary of the core, $r = a$, to be displaced radially outward an amount $du(a)$ so that the volume swept out by the movement of these particles is equal to the volume of material displaced by the indenter. As the indenter penetrates the specimen, the radius of the core, assumed to be equal to the radius of the circle of contact, increases an amount da, which is greater than $du(a)$. Material particles formerly at the outer boundary of the core are now in the interior, the core boundary having moved outward beyond them. But, it is important to note that it is the radial displacements of particles at the initial core boundary and not the movement of the boundary that gives rise to the volumetric compatibility with the

movement of the indenter. The elastic-plastic boundary, at radius *c*, also extends an amount *dc*, which depends on the type of indenter. For geometrically similar indentations, such as a conical indenter, the ratio *c/a* is a constant for all values of load and penetration depths.

The volume of the material displaced by the indenter is accommodated by radial displacements *du(a)* of material at the moving boundary of the rigid, hydrostatic core. These displacements give rise to stresses that are sufficiently high to cause plastic deformation in the surrounding material, *i.e.* the plastic zone. Assumption of Johnson's model [4.2, 4.3] is summarized as following: 1) volume conservation through plasticity, 2) the additional volume displaced by the indenter is equal to the additional volume of the indentation core, and 3) there is no elastic recovery of the volume displaced by the indenter.

Within the plastic zone, $a < r < c$, the stresses are given by Hill [4.4, 4.5] as:

$$\frac{\sigma_r}{\sigma_{ys}} = -2\ln\left(\frac{c}{r}\right) - \frac{2}{3} \tag{4-3a}$$

$$\frac{\sigma_\theta}{\sigma_{ys}} = -2\ln\left(\frac{c}{r}\right) + \frac{1}{3} \tag{4-3b}$$

The yield criterion in this case is simply σ_r - σ_θ = σ_{ys}. At the core boundary, $r = a$. the radial stress given by Eq. (4-3) is equal to the pressure p_i within the core (with a change in sign) so that:

$$\frac{p_i}{\sigma_{ys}} = \frac{2}{3} + 2\ln\left(\frac{c}{a}\right) \tag{4-4}$$

Outside the plastic zone, r ≥ c. and:

$$\frac{\sigma_r}{\sigma_{ys}} = -\frac{2}{3}\left(\frac{c}{r}\right)^3 \tag{4-5a}$$

$$\frac{\sigma_\theta}{\sigma_{ys}} = \frac{1}{3}\left(\frac{c}{r}\right)^3 \tag{4-5b}$$

Thus, within the plastic zone, the radial stress decreases in magnitude from that within the core, p_i, to -2/3σ_{ys} and the hoop stress correspondingly increases to satisfy the yield criterion to reach a maximum value of 1/3σ_{ys} at the elastic-plastic boundary. Outside the plastic zone, both stresses decrease with increasing r, and the yield criterion is no longer met.

Radial displacement of material at the boundary of the core $r = a$, according to Hill [4.4, 4.5], can be found from:

$$\frac{du(a)}{dc} = \frac{\sigma_{ys}}{E}\left[3(1-\nu)\frac{c^2}{a^2} - 2(1-2\nu)\frac{c}{a}\right] \tag{4-6}$$

Now, for an increment of penetration *dh*, the volume displaced by the indenter is equivalent to that of the movement of material particles on the boundary of the hydrostatic core, hence, for a conical indenter:

$$2\pi a^2 du(a) = \pi a^2 dh = \pi a^2 \tan\beta \, da, \tag{4-7}$$

where β is the angel of inclination of the indenter with the specimen surface.

Since:

$$\frac{du(a)}{dc} = \frac{du(a)}{da}\frac{da}{dc}, \tag{4-8}$$

we have:

$$\frac{\sigma_{ys}}{E}\left[3(1-\nu)\frac{c^2}{a^2} - 2(1-2\nu)\frac{c}{a}\right] = \frac{1}{2}\tan\beta\frac{da}{dc} \tag{4-9}$$

For geometrically similar indentations, such as with a conical indenter, the radius of the plastic zone increases at the same rate as that of the core, hence, *da/dc* = *a/c*. Using these results in Eq. (4-9) and substituting the

resulting expression for *c/a* into Eq. (4-4) we obtain:

$$\frac{p_i}{\sigma_{ys}} = \frac{2}{3}\left[1 + \left(\frac{(E/\sigma_{ys})\tan\beta + 4(1-2\nu)}{6(1-\nu^2)}\right)\right], \tag{4-10}$$

where p is the pressure within the core. The core pressure is directly related to the mean contact pressure beneath the indenter and according to Johnson [4.2, 4.3] is given by:

$$p_m = p + \frac{2}{3}\sigma_{ys}, \tag{4-11}$$

and this leads to an value for the constraint factor *C*. When the free surface of the specimen begins to influence appreciably the shape of the plastic zone, and the plastic material is no longer elastically constrained, the volume of material displaced by the indenter is accommodated by upward flow around the indenter. The specimen then takes on the characteristics of a rigid-plastic solid, because any elastic strains present are very much smaller than the plastic flow of unconstrained material. Plastic yield within such a material depends upon a critical shear stress, which may be calculated using either of the von Mises or Tresca failure criteria.

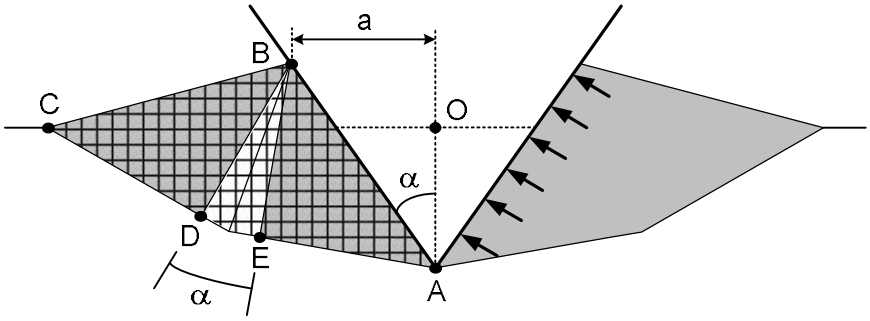

Fig. 4.1. Slip-line theory.

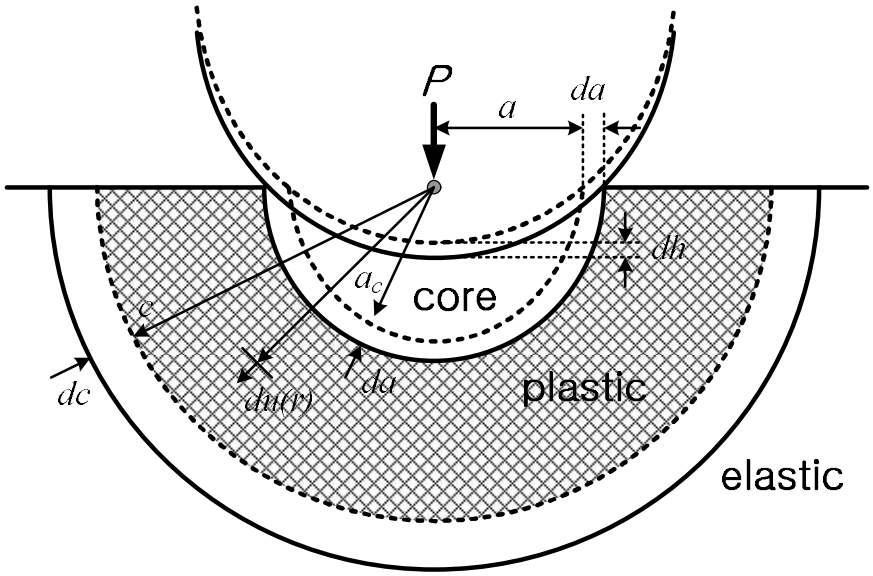

Figure 4.2. Expanding cavity model schematic.

References

[4.1] R. Hill, E. H. Lee, S. J. Tupper, The theory of wedge indentation of ductile materials, *Proc, R. Soc. Lond*. A 188, 273 (1947)

[4.2] K.L. Johnson, Contact Mechanics, *Cambridge University Press*, Cambridge (1985).

[4.3] K.L. Johnson, *J. Mech. Phys*. Sol.18, 115 (1970).

[4.4] R. Hill,The Mathematical Theory of Plasticity, *Clarendon Press*, *Oxford* (1950).

[4.5] R.F. Bishop, R. Hill, N.F. Mott, The theory of indentation and hardness tests, *Proceeding, Physics Society* 57, 147 (1945).

Chapter 5

Determination of Contact Area at High-Temperature

Contents

This section is slightly modified version of the paper published in *Materials Science and Engineering A* [Volume 650, (2016), pp 15-19] by Chan-Pyoung Park etc. titled "Evaluation of high-temperature Vickers hardness using instrumented indentation system".

5.1. Introduction

Instrumented indentation testing (IIT) improves on conventional hardness testing by allowing various mechanical properties to be evaluated by analysis of the load-depth curve during indentation. IIT has a simple procedure and the advantage of measuring a local area such as a weldment, so it has been used extensively to evaluate in-field safety of power and petrochemical plants [5.1-5.4]. In recent years, IIT has also evaluated not only hardness and elastic modulus but also strength, fracture toughness, and residual stress. Evaluating all these mechanical characteristics requires knowledge of the contact area [5.5-5.11]; this is obtained by measuring a penetration depth from the material surface in loading and reflects the geometrical shape of the indenter, whereas the contact area in conventional hardness testing is obtained by observing the indentation mark [5.1-5.2].

Studies to determine contact area have performed through finite element analysis or experiments considering the elastic-plastic behavior of several

materials. However, most of these studies have been limited to room temperature [5.12-5.16]; the high-temperature contact area has been determined by using the equation developed at room temperature or a modified equation reflecting high-temperature effects. The difficulty is that most high-temperature studies entail development and calibration of equipment. In addition, previous studies have been performed on the nano scale and at relatively low temperatures, usually below 200 °C [5.17-5.21].

In this study, a high-temperature instrumented indentation system (HTIIS), available on macro scale up to 650 °C, was developed. In addition, frame compliance (C_{frame}), i.e. the mechanical measurement-errors occurring at high-temperatures, was calibrated. To determine the contact area accurately using this new equipment, the pileup phenomenon occurring around the contact area during indentation, was quantified and its physical meaning was analyzed. A new calibration factor $f_{(T)}$ is suggested to correct for the pileup effect at high-temperatures, and conventional high-temperature Vickers testing was conducted to verify the reliability of HTIIS and the contact area from $f_{(T)}$.

5.2. Experiments

To carry out the high-temperature indentation experiments, a high-temperature chamber was constructed and IIT equipment was attached. The inside of the chamber contained a halogen lamp, thermocouples and stage. Specimen oxidation and thermal draft, reported in previous research, were prevented by vacuum conditions [**5.**17-**5.**19]. A radiation shield and cool water circulation were set up around the stage and around the connecting shaft of IIT. All specimen faces were heated equally by the halogen lamp. Thermocouples enabled real-time temperature detection in the indenter, specimen surface, and stage, and the movement of the stage was controlled externally. Figure 5.1 and table 5.1. show the features of the HTIIS and its specifications.

One experiment was performed to calibrate the frame compliance, as caused by elastic deformation of HTIIS during indentation [**5.**1, **5.**2]. A standard hardness specimen (HV300) was used, and the Vickers indenter had face-to-face angle 136°. The indentation rate was constant at 0.3 mm/min [**5.**8, **5.**15, **5.**16] and the indentation depth was 80 μm. The temperature was varied at 100 °C intervals from room temperature to 600 °C in vacuum condition, and the indentation load-depth curve was measured five times at each temperature. Stiffness was determined from the data at the start of the unloading curve.

Another experiment was performed under the same conditions to evaluate the contact area using HTIIS for nine kinds of carbon steels: SKS3, S45C, SKH51,

SUJ2, SKD61, SK3, SKD11, SCM4 and SCM21 at 25 ℃, 200 ℃, 400 ℃ and 600 ℃. The specimen surface was polished to 1 μm.

Lastly conventional high-temperature Vickers hardness testing was performed to verify HTIIS experimental results for the same nine carbon steels. AVK-HF (Akashi, Japan) was used for conventional Vickers hardness testing at 25 ℃, 200 ℃, 400 ℃ and 600 ℃ at the Technology Innovation Center for Fine Ceramics (FCTIC, Korea).

5.3. Results and Discussion

The measured indentation depth when the load is applied is affected by forces acting normal to the specimen and by forces of the same size acting in the opposite direction to the equipment. Hence errors can arise in the measured indentation depth. Determining the deformation from the forces acting normal to specimen is called calibration of frame compliance. Figure 5.2 shows the total frame compliance (C_{total}) of the HTIIS from room temperature to 600 °C. Following in Oliver and Pharr's footsteps [**5.**1-**5.**2], C_{total} can be determined from the stiffness by analyzing data from the unloading curve. The value of C_{total} increases with increasing temperature because the shaft of HTIIS and the specimen are heated at the same time by the halogen lamp, so the elastic modulus of shaft and specimen are reduced to facilitate the deformation. In other words, the elastic modulus of both shaft and specimen decreases with increasing temperature: C_{total} has an inverse relationship with elastic modulus and thus tends to increase linearly. (Oliver and Pharr could consider C_{total} as constant because their work was performed only at room temperature.) Thus, through the relationship between the calculated C_{total} and the observed contact area, the indentation depth can be calibrated by calculating the frame compliance (C_{frame}) as in equation (5-1) [**5.**1, **5.**2]:

$$C_{total} = C_{frame} + \frac{\sqrt{\pi}}{2E_r} \cdot \frac{1}{\sqrt{A_c}} \qquad (5\text{-}1)$$

Where C_{total} is the total frame compliance of the equipment, E_r is the reduced elastic modulus and A_c is the contact area. Extension of this method in this study confirms that the value of C_{total} is linear with temperature, so the indentation depth at high-temperatures can be corrected using equation (5-2) derived from the data fitting in Figure 5.2:

$$C_{total} = 6.763 \times 10^{-5} \cdot T(^{\circ}C) + 0.172 \qquad (5\text{-}2)$$

Equation (5-2), proposed in this study, gives the compliance change of all modules of HTIIS as a function of temperature. In addition, it was difficult to observe the contact area directly in the chamber during the high-temperature experiments. Therefore, assuming that the hardness value that normalizes the load to the contact area is always constant, it is applied to the equation as in equation (5-3), by replacing A_c with the ratio of the hardness (H) and maximum load (L_{max}):

$$C_{total} = C_{frame} + \frac{\sqrt{\pi}}{2E_r} \cdot \frac{\sqrt{H}}{\sqrt{L_{\max}}} \qquad (5\text{-}3)$$

Another issue in studying HTIIS is precise determination of the contact area, since this is used as a basic parameter in evaluating mechanical properties.

Figure 5.3 shows that h_c is the vertical depth along which contact is made, and h_m is the depth at maximum load. h_f is the final depth which occurs after unloading; elastic recovery of material. Contact area is derived from indentation depth. Thus, to determine an accurate indentation depth, it is important not only to calibrate the frame compliance but also to quantify the effect of pileup, i.e. atoms accumulating on the periphery of the indenter during plastic deformation. According to previous studies, ignoring the pileup effect can lead to differences in contact area of up to fifty percents [**5.**22, **5.**23]. Various studies have been conducted to quantify the pileup effect. Among these are studies using f as a pileup calibration factor, where f is defined in equation (5-4) and it is a dimensionless factor:

$$f = \frac{h_c}{h_m} \qquad (5\text{-}4)$$

The factor f expresses the height of the pileup as the ratio of the real indentation depth (h_c), which is considered to be from plastic accumulation, and the maximum indentation depth (h_m), which can be measured from the equipment. Previous studies have reported that f is associated with material properties and

can be expressed using tensile parameters as well as indentation parameter as in equation (5) [**5.**3, **5.**12, **5.**14-**5.**16]:

$$f \approx \frac{\sigma_y}{E} \approx \frac{H}{E} \approx \frac{W_e}{W_{total}} \approx \frac{h_m}{h_m - h_f} \qquad (5\text{-}5)$$

However, so far, only at room temperature have studies of pileup been performed for quantification. At high-temperatures, yield strength, elastic modulus, and work-hardening values are generally reduced, so it can be inferred that the effect of increasing temperature should be reflected.

Figure 5.4 shows the increase in pileup with increasing temperature and the relation between pileup and the indentation parameter and demonstrates the linearity between pileup and indentation parameter, as found in previous room-temperature studies. However, what happens when temperature increases? As temperature increases, the slope of this linearity gradually decreases and the values of intercept increase dramatically:

$$f_{(T)} = A_{(T)} \cdot (\frac{h_m}{h_m - h_f}) + B_{(T)} \qquad (5\text{-}6)$$

Here h_m is maximum indentation depth and h_f is final indentation depth. As shown in equation (5-6), the slope ($A_{(T)}$) is the ratio of the variation of

indentation parameter against the variation of increasing pileup with increasing temperature. In this study, h_m is constant at 80 μm. Thus, the $A_{(T)}$ is related to the indentation variable (h_m-h_f), which represents the amount of elastic recovery after unloading. Figure 5.5 shows that the change of slope at each temperature in Figure 5.4 relates to the amount of elastic recovery in the specimen; in other words, at each temperature the slope could change depending on whether or not the specimens show large elastic recovery. For instance, comparing the slope and elastic recovery at each temperature in SCM21 and SKD61 in Figures 5.4 and 5 shows that the amount of elastic recovery decreases with increasing temperature. The decrease in elastic recovery is related to pileup, so this confirms that the slope is gradually decreased.

Note that in the case of S45C and SK3 in Figure 5.6, the relation of pileup and indentation parameter does not seem to be linear, unlike in Figure 5.4. The S45C and SK3 specimens undergo a phenomenon called blue shortness or blue brittleness, which usually occurs from 200 ℃ to 400 ℃: the surface color becomes blue and hardness or strength temporarily increases. The results in Figure 5.6 may confirm the experimental results of Riaz and Atiqah [**5.**24]. This phenomenon is relevant to deformation behavior of metal at high-temperatures. Metals under short-term deformation at high-temperatures can be hardened due to easy dislocation proliferation and cross-slip, and can at the same time recover due to recrystallization or dislocation extinction or rearrangement. Hardening and recovery offset each other at once during high-temperature deformation, so

that elastic-plastic deformation proceeds in balance. However, in this specific temperature range, the offset and the balance no longer occur, hardening dominates recovery, and consequently the metal is strengthened [**5.**25]. Therefore, the hardness value of S45C and SK3 at 400 ℃ becomes higher than the value at 200 ℃.

Figure 5.4 shows that the value of the intercept ($B_{(T)}$) increases with increasing temperature. This is because fitting is carried out in one dimension, as in equation (6). The increase in pileup with increasing temperature could be also represented as an increase of $B_{(T)}$. Thus, this study proposes a new equation calibrating pileup effect by taking temperature into account:

$$f_{(T)} = [\alpha \cdot (^{\circ}C) + \beta] \cdot (\frac{h_m}{h_m - h_f}) + [\gamma \cdot (^{\circ}C) + \delta] \qquad (5\text{-}7)$$

Where, [α·(℃)+β] is [$-4.225 \cdot 10^{-6}$·(℃)+0.004] and, [γ·(℃)+δ] is [$2.322 \cdot 10^{-4}$·(℃)+0.989]. Equation (5-7) is derived by fitting from the data in Figure 5.4 about a decreased slope and an increased intercept aspect with increasing temperature. Using equation (5-7) yields the real indentation depth (h_c,) and thus makes it possible to determine the real contact area at high-temperature.

Figure 5.7 shows hardness results as evaluated by HTIIS using equation (5-7) and by conventional methods (optical observation). Conventional Vickers hardness is defined in equation (5-8) and (5-9) by considering the geometrical

shape of indenter [**5.**16, **5.**26]:

$$HV(^{\circ}C) = \frac{L_{\max}}{26.43 \cdot (h_c^2)} \qquad (5\text{-}8)$$

$$h_c = \frac{d}{2\sqrt{2}\tan\theta^{\circ}} \qquad (5\text{-}9)$$

where L_{max} is the maximum load, and Θ is the half angle of the Vickers indenter here 68^{o} and d is the diagonal length of the indentation mark. The relationship between the diagonal and contact depth at high-temperature is defined here by using equation (5-7) and $f_{(T)}$; where ($h_c = f_{(T)} \cdot h_{max}$). Generally HV can be evaluated by measuring diagonal length of indentation mark directly even high-temperature.

However, HV can also be evaluated by measuring indentation depth and considering geometrical shape of indenter. Because contact area is a function of indentation depth and HV is a function of the maximum load and contact area. It can be seen that the Figure 5.7 compares HV resulting from calibrated and un-calibrated indentation depth (h_c). In other words, if $h_c = h_{max}$ is derived from d by optical observation at high-temperature, the conventional method is indicated. But, if $h_c = f_{(T)} \cdot h_{max}$ is derived from equation (5-7), the pileup calibration method at high-temperature studied here is meant.

The results match within 10% error. It is difficult, however, to agree that equation (5-7) describes the pileup behavior completely at high-temperature, even though the hardness results agree well. Because a peculiar hardening behavior occurs at high-temperature (blue brittleness in Fig. 6), in order to solve this problem, the effect of temperature on the hardening behavior, which has been ignored in some in previous studies, must be studied in more detail.

5.4. Summary

This study investigates the real contact area, which is a basic indentation parameter in evaluating various mechanical properties at high-temperatures, using a newly constructed high-temperature instrumented indentation system (HTIIS). The elastic deformation of the HTIIS was calibrated according to increasing temperature. Pileup behavior was measured with changing temperature and was quantified using an indentation parameter. The hardness value yielded by the proposed pileup calibration factor $f_{(T)}$ for high-temperatures is in agreement within 10% error with conventional high-temperature hardness testing.

Table 5.1 Specifications

	Specification		
IIT	Load	Maximum	300 kgf
		Resolution	5.6 gf
	Depth	Stroke	40 mm
		Resolution	0.1 um
	IIT shaft	Length	192 mm
H.T chamber	Vacuum	Rotary pump	0.01 Torr
	Heat	Source	Halogen lamp
		Range	0 ℃ ~ 650 ℃
	Thermal couple	K-type	Indenter; Specimen; Stage

Table 5.2 Mechanical properties of specimens

	E (GPa)	YS (MPa)	UTS (MPa)	n	HV
SKS3	210	435	756	0.22	195
S45C	212	363	774	0.26	171
SKH51	223	295	784	0.26	222
SUJ2	217	404	822	0.24	199
SKD61	214	371	781	0.24	201
SK3	207	315	707	0.26	165
SKD11	217	343	808	0.26	230
SCM4	235	723	994	0.13	229
SCM21	194	271	653	0.22	137

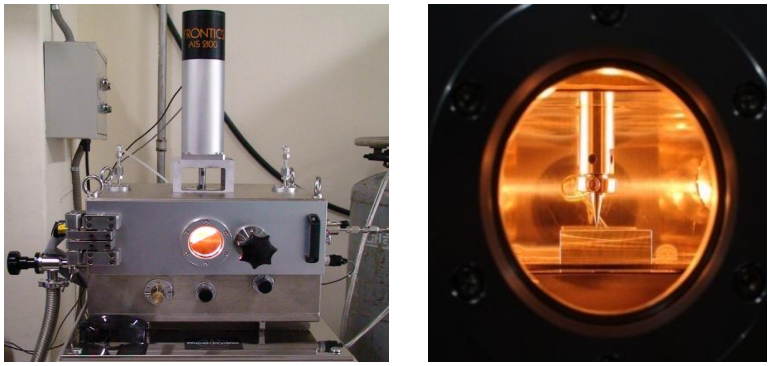

Fig. 5.1. Structure of HTIIS

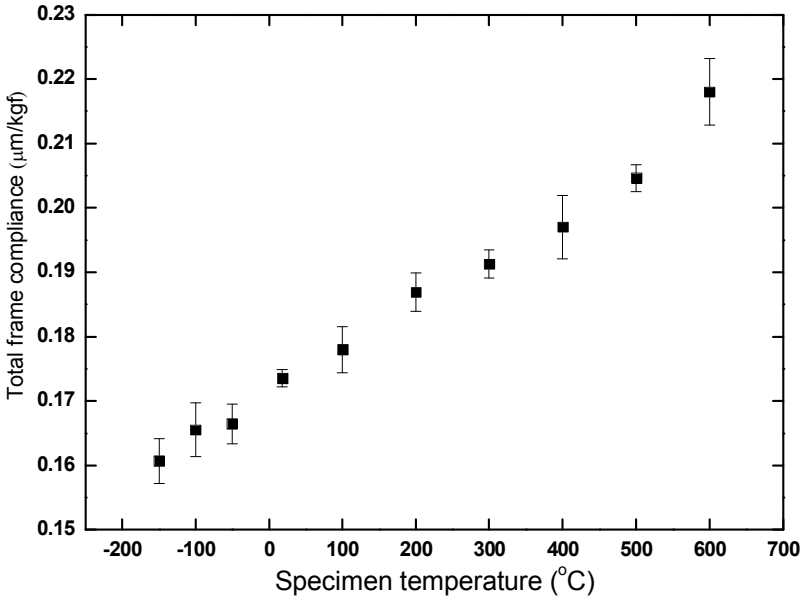

Fig. 5.2. Total frame compliance C_{total} (μm/kgf) at 25 ℃ - 600 ℃

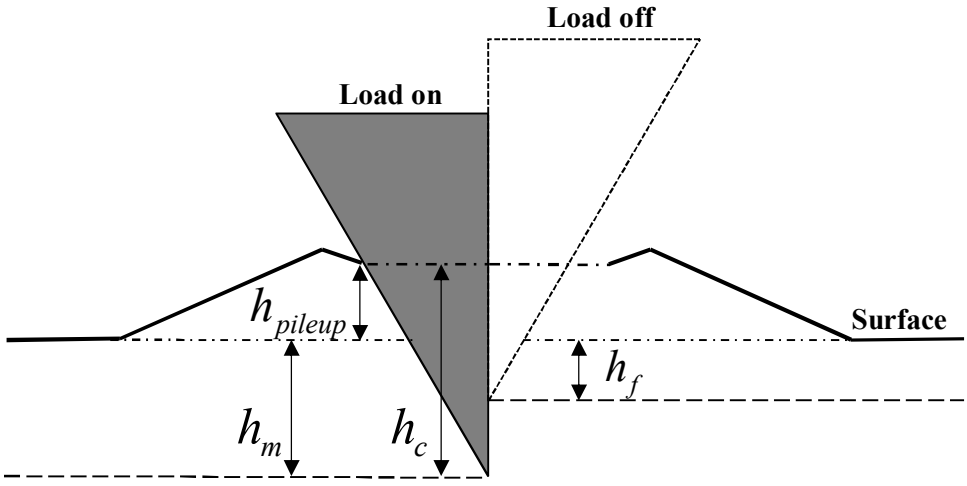

Fig. 5.3. Contact morphology with pile-up

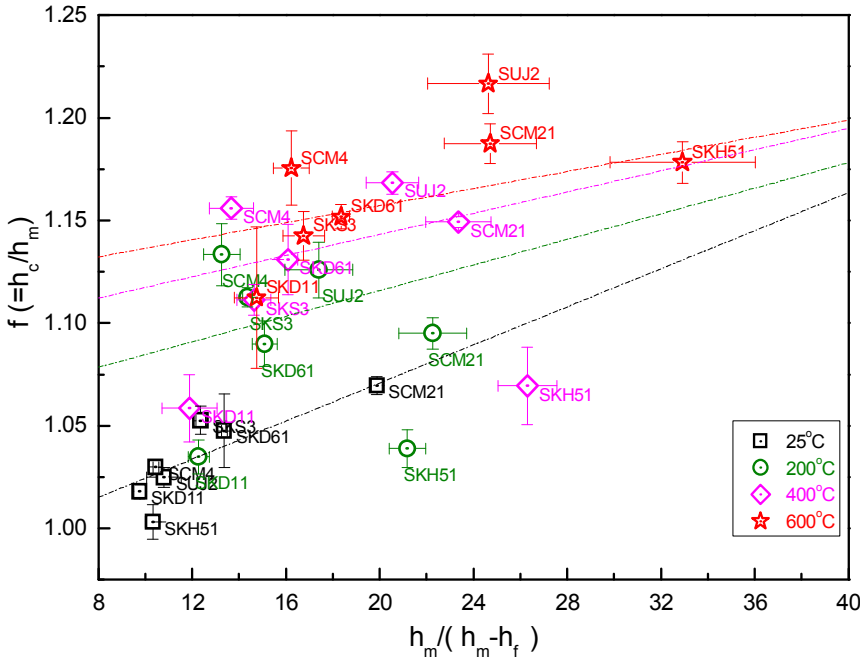

Fig. 5.4. Relationship of f and $h_m/(h_m-h_f)$ at 25 ℃, 200 ℃, 400 ℃, 600 ℃

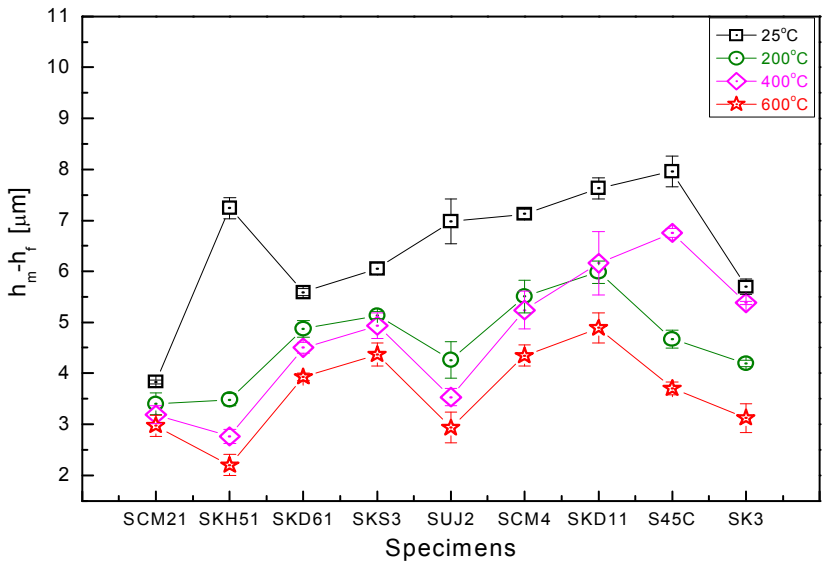

Fig. 5.5. Elastic recovery h_m-h_f (μm) for specimens at 25 ℃, 200 ℃, 400 ℃, 600 ℃

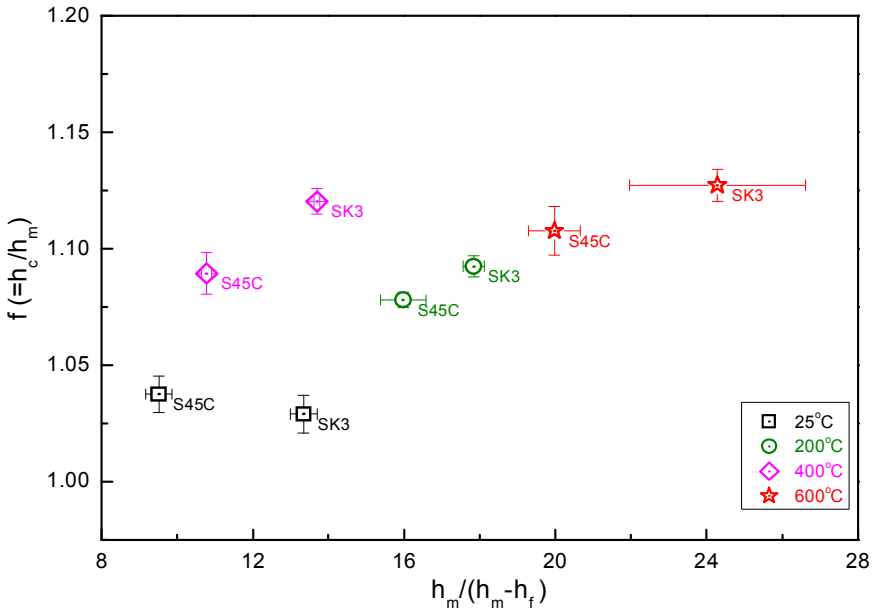

Fig. 5.6. S45C and SK3: relationship of f and $h_m/(h_m-h_f)$ at 25 ℃, 200 ℃, 400 ℃, 600 ℃

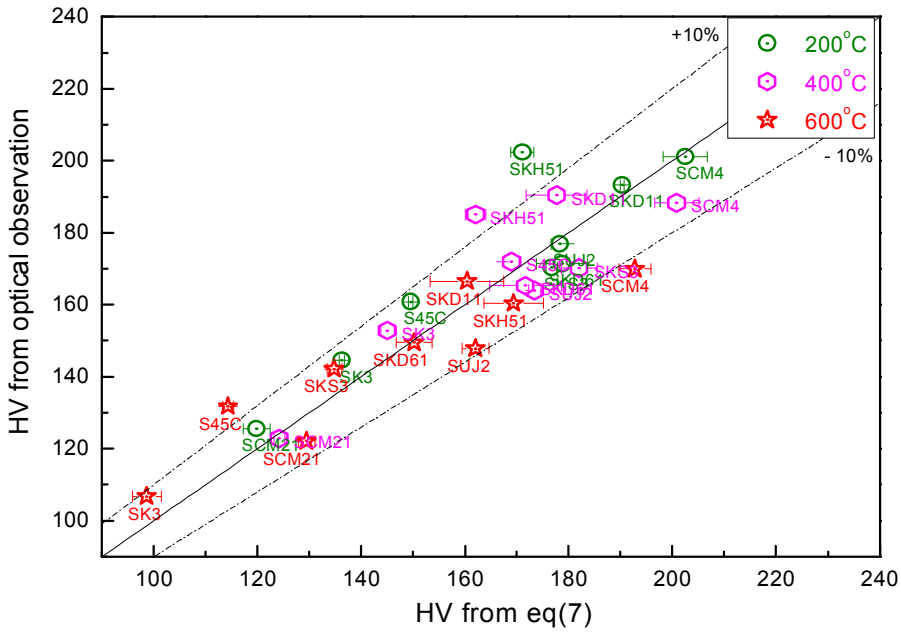

Fig. 5.7. Comparison of hardness results by conventional method and by HTIIS using eq. 5-7

References

[5.1] W.C. Oliver and G.M. Pharr: An improved technique for determining hardness and elastic-modulus using load and displacement sensing indentation experiments. *J. Mater. Res*. 7, 1564 (1992).
[5.2] W.C. Oliver and G.M. Pharr: Measurement of hardness and elastic modulus by instrumented indentation: Advances in understanding and refinements to methodology. *J. Mater. Res*. 19, 3 (2004).
[5.3] A. Bolshakov and G.M. Pharr: Influences of pileup on the measurement of mechanical properties by load and depth-sensing indentation techniques. *J. Mater. Res*. 13, 1049 (1998).
[5.4] Y.-H. Lee, D. Kwon: Estimation of biaxial surface stress by instrumented indentation with sharp indenters, *Acta Mater*. 52, 1555 (2004)
[5.5] S.I. Bulychev, V.P. Alekhin, M.Kh. Shorshorov and A.P. Ternovskii: Mechanical properties of materials studied from kinetic diagrams of load versus depth of impression during microimpression. *Prob. Prochn.* 9, 79 (1976)
[5.6]. J.C. Hay, A. Bolshakov and G.M. Pharr: A critical examination of the fundamental relations used in the analysis of nanoindentation data. *J. Mater. Res*. 14, 2296 (1999)
[5.7] E.G. Herbert, G.M. Pharr, W.C. Oliver, B.N. Lucas, J.L. Hay: On the measurement of stress-strain curves by spherical indentation. *Thin Solid Films.* 398–399, 331 (2001).
[5.8] J.S. Lee, J.I. Jang, B.W. Lee, Y. Choi, S.G. Lee, D. Kwon: An instrumented indentation technique for estimating fracture toughness of ductile materials: A critical indentation energy model based on continuum damage mechanics. *Acta Mater*. 54, 1101 (2006)

[5.9] S. Suresh, A.E. Giannakopoulos: A new method for estimating residual stresses by instrumented sharp indentation. *Acta Mater.* 465, 755 (1998)
[5.10] K.L. Johnson: Contact Mechanics, *Cambridge University Press*, Cambridge, UK (1985)
[5.11] J.-H. Ahn, Y. Choi and D. Kwon: Evaluation of plastic flow properties of materials through the analysis of indentation load-depth curve. *Kor. Inst. Met. & Mat*. 38, 16067 (2000)
[5.12] Y.T. Cheng and C.M. Cheng: Relationships between hardness, elastic modulus, and the work of indentation. *Appl. Phys*. Lett. 73, 614 (1998).
[5.13] Y.T. Cheng and C.M. Cheng: What is indentation hardness? *Surf. Coat. Technol*. 133–134, 417 (2000).
[5.14] J. Alcala, A.C. Barone, and M. Anglada: The influence of plastic hardening on surface deformation modes around Vickers and spherical indents. *Acta Mater*.
48, 3451 (2000).
[5.15] Y. Choi, H.S. Lee, and D. Kwon: Analysis of sharp-tip-indentation load-depth curve for contact area determination taking into account pile-up and sink-in effects. *J. Mater. Res*. 19, 3307 (2004).
[5.16] S.K. Kang, J.Y. Kim, C.P. Park, H.U. Kim and D. Kwon: Conventional Vickers and true instrumented indentation hardness determined by instrumented indentation test. *J. Mater. Res* 25, 2 (2010).
[5.17] C.A. Schuh, C.E. Packard, and A.C. Lund: Nanoindentation and Contact Mode Imaging at High-Temperatures. *J. Mater. Res.* 21(3), 725 (2006)
[5.18] B.D. Beake and J.F. Smith: High-temperature nanoindentation testing of fused silica and other materials. *Philos. Mag*. A82, 2179 (2002)
[5.19] J.F. Smith and S. Zheng: High-temperature nanoscale mechanical property measurement. *Surf. Eng*. 16, 143 (2000)
[5.20] B.N. Lucas and W.C. Oliver: Indentation Power-Law Creep of High

Purity Indium. *Metall. Mater. Trans.* 30A, 601 (1999)
[5.21] C.A. Schuh, J.K. Mason, and A.C. Lund: Quantitative insight into dislocation nucleation from high-temperature nanoindentation experiments. *Nat. Mater*. 4. 617 (2005)
[5.22] Y.Y. Lim, A.J. Bushby and M.M. Chaudhri: Nano and macro indentation studies of polycrystalline copper using spherical indenters. *Mater. Res. Soc. Symp. Proc.* 522, 145 (1998)
[5.23] Y.Y. Lim, M.M. Chaudhri and Y. Enomoto: Accurate determination of the mechanical properties of thin aluminium films deposited on sapphire flats using nanoindentation. *J. Mater. Res.* 14, 2314 (1999)
[5.24] M. Riaz and N. Atiqah: A study on the mechanical properties of S45C medium type carbon steel specimens under lathe machining and quenching condition. *IJRET*. 3, 12 (2014)
[5.25] George E. Dieter: Mechanical Metallurgy (third edition), *University of Maryland*, McGraw-Hill Inc, USA (1986)
[5.26] ISO/FDIS 14577-1: Metallic Materials-Instrumented Indentation Test for Hardness and Materials Parameters; Part 1, Test Method, *International Organization for Standardization*, Geneva, Switzerland, (2002)

Chapter 6

Evaluation of Hot Hardness at High-Temperature

Contents

6.1. Introduction

It is well known that the mechanical behavior of most metals and alloys is dependent on temperature. X20CrMoV12.1 [6.1] and Alloy617 [6.2] are used in boiler and turbine rotors on a macro scale Al-Si particles [6.3] and Sn-Ag-Cu [6.4] are used in solar cells and solder balls on a micro/nano scale. These materials experience complex temperature histories both in industrial forming processes and under environmental conditions of use. An understanding of the high-temperature mechanical properties of these alloys and metals over a wide range of temperature is very important with the ever-increasing demand for materials suitable for high-temperature use.

One of the simplest and quickest means of understanding the mechanical behavior of materials is by evaluation of hardness [6.5, 6.6], since tensile properties, creep rupture, and residual stress have often been correlated with hardness in many investigations [6.7]. However, the practical conventional methods for evaluating such properties require specific specimen shapes and large equipment under standard codes, and these are both time and sample consuming procedures.

Hardness, on the other hand, is easy and inexpensive to assess. The use of Instrumented Indentation Testing (IIT) at high temperatures yields more information than conventional high-temperature hardness testing. At high temperatures IIT gives accurate measurements of the continuous variation of

indentation load as a function of indention depth. Its great merit is that contact area can be determined by interpreting the load-depth curve, i,e. without optical observation. However, it is not easy to determine the exact contact area because of complex elastic-plastic deformation behavior (pileup and sink-in) around the indentation impression [6.8].

A previous study [6.9], introduced a calibration function "*f*" for high-temperature contact area for each experimental temperature to determine the exact contact depth; the contact area can be derived from contact depth [6.10]. The function "*f*" (which is geometrically the pileup height) was configured using parameter of maximum indentation depth (h_{max}) and final indentation depth (h_f). Using the combination of h_{max} and h_f can compensate for errors in indentation contact depth (h_c).

The problem in the prior study is that the shape of calibration function must be obtained empirically at every experimental temperature: this study indicated that the calibration function may vary depending on experimental conditions and individual experimental samples, and thus may not be regarded as a general solution for determining the exact contact area at high temperatures.

To break away from previous empirical study, this study modifies Westbrook's equation. Originally Westbrook [6.11] suggested that the temperature dependence of hardness could be expressed as

$$H = A\exp^{-BT} \qquad (6\text{-}1)$$

where H is hardness, T is temperature, and A, B are constants. Westbrook obtained results by which plotting $log\ H$ versus temperature for pure metals generally produced two straight lines of different slope. The A derived from the low-temperature branch of the curve can be considered to be the intrinsic hardness of the metal, that is, H at $0\ K$. The constant B, derived from the slope of the curve, is the temperature coefficient of hardness and was related in a rather complex way to the rate of change in heat content with increasing temperature.

Although great progress in elucidating the hardness-temperature relationship was made by Westbrook, the physical meaning of constants A and B is still not clear enough to account for the complexity of the dynamic response of metals at high temperatures. Furthermore, the original equation can accurately calculate hardness over only one-half the melting-point ranges of pure metals [6.12]. Additionally, according to a study of the *AlCoCrFeMoNi* alloy [6.13], although Westbrook's equation was satisfied by some amount of the cobalt composition, the lower the cobalt content, the higher (less accurate) the hardness value.

This study first newly defines the relationship of hardness and temperature, the modified Westbrook's equation, on the basis of the shape of existing constitutive equations that comprise the thermodynamic foundation. Second, the physical meaning of each parameter is considered through mathematical development. Third, the indentation contact depth for penetration is expressed as a function of

indentation variables and temperature. Fourth, the amount of contact area converted from the newly defined equation is compared to the contact area obtained from conventional optical observations. Finally, to ensure the validity of our results, hardness values obtained from a different institute for the same materials are compared with those from this study. Through this sequence of studies, a form of the comprehensive equation is suggested for calculating contact area and hardness at high temperatures.

6.2. Experiments

Eight kinds of Body Centered Cubic (BCC) structure, Cr-Mn alloy steels of chemical composition shown in table 6.1 was used in the experiments. Disc-shaped or rectangular bulk indentation specimens were used, in accordance with ASTM standards E 92-82 (2003). The disc-shaped specimens had diameter 40 *mm* and thickness 15 *mm*, the rectangular specimens had a length 40 *mm* and thickness 15 *mm*. High-temperature instrumented indentation tests (IIT) were conducted on the Frontics machine (model AIS2100, Korea) and self-developed chamber using Vickers indenter. The equipment was described in detail in in the preceding study [6.9] and further details are omitted here. The indentation rate was constant at 0.3 *mm/min* [6.9, 6.14, 6.15, 6.16] and the indentation depth was 80 μm by the depth-control method. The temperature was varied at *100 K* intervals from room temperature to *873.15 K* in vacuum condition. The penetration depth, that is indentation displacement, was measured using the linear variable displacement transducer (LVDT) method.

Another experiment on hardness at high-temperature was performed under the same conditions and specimens at a different institution, the Technology Innovation Center for Fine Ceramics (FCTIC, Korea). Whether tested in this study or in another institution, the impression contact area produced by the indentation test was measured with an optical microscope on an Akashi machine (model AVK-HF, Japan).

6.3. Results and Discussion

6.3.1. High-temperature deformation mechanism with hardness and load-depth curve

Hardness values can be easily obtained by observing the indentation impression. Fig. 6.1 shows the typical hardness-temperature relation obtained from conventional Vickers hardness test, not IIT, in FCTIC of the alloy steels studied.

It is noted that the hardness is strongly dependent on the temperature: it decreases with increasing temperature. The degradation of mechanical properties at high temperature is well known. The SKH51, AISI E52100, SKD61 and SCM21 specimens reflect a reduction in properties with temperature; however, the SKS3, S45C, AISI D2 and AISI W1 specimens show hardness values that increase in a certain temperature range around *673.15 K*. These phenomena can be explained by the material deformation behavior according to temperature. When a material is subjected to external force at high temperature, two mutually competitive mechanisms operate simultaneously: work hardening, mainly by external force and recovery, mainly by thermal energy. Metals can harden due to easy dislocation proliferation and cross-slip, and can at the same time recover due to recrystallization or dislocation extinction or rearrangement. Hardening and recovery can offset each other

during high-temperature deformation, so that elastic-plastic deformation proceeds in balance. However, in particular temperature ranges, balance can no longer occur, hardening dominates recovery, and consequently the metal is strengthened [6.12, 6.17, 6.18]. Therefore, the hardness of SKS3, S45C, AISI D2 and AlSI W1 at around *673.15 K* becomes higher than at *473.1 K*.

Fig. 6.2 shows the load-depth curve of AISI E52100 and S45C obtained by IIT at different temperatures. All IIT experimental specimens in this study were tested by the depth-control method to ensure that the penetration depth was 80 μm.

For SKH51, SKD61, and SCM21 specimens, as shown in Fig. 6.2 (a) for AISI E52100, it is ascertained that the maximum indentation load gradually decreases with increasing temperature. It can thus be inferred that the hardness values also decrease gradually with increasing temperature. For SKS3, AISI D2, and AISI W1, as shown in Fig. 6.2 (b) for S45C, we see that, despite the increased temperature, in a certain range the maximum indentation load gradually increases, and we can infer that material hardening also occurs in that range.

In light of the results in Figs. 6.1 and 6.2, the IIT test results are seen to be compatible with the results for high-temperature hardness. So the deformation mechanism associated with the isothermal IIT is a thermally activated process, and the measured load-depth curve also represents the competitive relation of work hardening and recovery.

6.3.2. Westbrook's model

Equation (6-1) above is the relationship between hardness and temperature suggested by Westbrook. In order to use equation (6-1), the constants A and B must be determined from experimental data.

The constant A corresponds mathematically to the y-axis intercept, so a way to obtain A is to take the logarithm hardness of Fig. 6.1, and plot it with temperature variables. To determine constant B, we must plot log hardness values with temperature after the transition point; the slope is the value of B. Here the transition point is generally the hardness at a temperature corresponding to one-half the melting temperature.

According to a suggestion by Westbrook, the constant of B cannot be derived from this study, because hardness values measured above 900 K are required for the specimens in this study and Figure 6.1 shows no obvious transition point. However, subsequent studies [6.19, 6.20, 6.21] show that the values for constant A and B can be determined regardless of transition point. For example, it is shown that, before and after the mechanism changes, the values of A and B also divided into $A1$, $B1$ and $A2$, $B2$. Table 6.2 shows the A and B values determined from the results of Fig 6.1 and adds the hardness measured at room temperature (H^{RT}).

The A values measured at 0 K are known to imply an intrinsic hardness, so it is appropriate that it have a higher value than at room temperature if the material

can become brittle at low temperatures. However, apart from the analysis results, the important point is that A and B have different values for each material. Using the results of other research [6.22, 6.23] in Westbrook's model shows that when the material changes, the values of A and B also change. So A and B must always be determined experimentally. Therefore, to address this issue, the equation must be modified to generalize the relationship between hardness and temperature.

6.3.3. The modified hardness-temperature relation

6.3.3.1. Modification of Westbrook's equation

When the material is in a high-temperature state, thermal energy flows into its interior and is absorbed by atoms. The probability that atom is in a certain energy state due to absorbed energy is closely related to the Boltzmann factor [6.24]. Any material consists of millions or more of atoms, so that applying Avogadro's number means that the Boltzmann factor can be thought of as expanding into activation energy. Thus, the activation energy term is included in such temperature-related equations as the Arrenius equation [6.25], stress-temperature equation [6.12], strain rate-temperature equation [6.26, 6.27], shear deformation-temperature equation [6.28], and dislocation-temperature equation [6.29].

Westbrook states that in his work, the parameter B is related to changes in heat content. However, according to later studies of George-Marisac Hwab [6.30], O. D. Sherby, etc [6.31], and Kirity Bhusan Khana, etc [6.7], the value of B can also be considered as a parameter related to the activation energy term. Such an activation energy term influences the force that moves the dislocations.

Equation 2 is well known dislocation equation that indicates the temperature dependence of the average velocity of shear deformation [6.12]:

$$\bar{v}_d = \alpha \cdot \sigma_d \cdot e^{-\frac{Q}{RT}} \qquad (6\text{-}2)$$

where $\bar{v}_d$ is the mean velocity of the dislocation, σ_d represents the required stress for dislocation movement, Q is the activation energy, R is the gas constant, T is the temperature, and α is a proportional constant to equalize the left and right sides.

If σ_d in equation (6-2) is transposed to the left side, the equation can be written so as to include the hardness that occurs at a certain critical stress:

$$H = \sigma_{critical} = \frac{\bar{v}_{critical}}{\alpha \cdot e^{-\frac{Q}{RT}}} = \left(\frac{\bar{v}_{critical}}{\alpha} \right) e^{\frac{Q}{RT}} = \left(\frac{\dot{\gamma}_{(f)} / b\rho}{\alpha} \right) e^{\frac{Q}{RT}} \qquad (6\text{-}3)$$

where H is hardness and $\dot{\gamma}_{(f)}$ indicates the shear deformation velocity, which is affected by the thermal frequency; b is the Burgers vector and ρ is the dislocation density.

Equation 6-3 states that when material is heated, the energy is transferred as the wave form and affects the shear deformation velocity.

If we imagine a certain material with constant volume and density, the variable in equation (6-3) could be heat, and its frequency might cease at *0 K*, so the Multiplicity (Ω), defined by Boltzmann's entropy equation, can have only one

case and the entropy is zero.

Therefore, in the macroscopic perspective it seems appropriate to express the $(\dot{\gamma}_{(f)} / b\rho)/ \alpha$ as an intrinsic hardness described in Westbrook's original form. However, it seems appropriate to use H_0 instead of A to contain more physical meaning. So, to sum up, it is believed that the relationship between the hardness and temperature is appropriately expressed by (6-4) rather than (6-1):

$$H = H_0 \cdot e^{+\frac{Q}{RT}} \qquad (6\text{-}4)$$

6.3.3.2. Development of contact area equation from modified Westbrook's model

One of the purposes of this study, as mentioned earlier, is to accurately determine the contact area after IIT at high temperatures. The reason why contact area is more important than hardness is that it can affect physical properties such as elastic modulus, tensile properties and residual stress [6.32-6.36].

In the newly defined equation (6-4), the hardness on the left side can be thought of as a substitute for *F/A*, depending on the definition of hardness, where *F* is the load imposed on the specimen and *A* is contact area.

The contact area (A_c) can be expressed as the product of a constant (C_1) and the square of the indentation contact depth (h_c^2), according to the work of Oliver and Pharr's [6.10]. Then, taking the logarithm on both sides to eliminate the exponential, the equation (6-4) can be rewritten as:

$$\ln\left(C_1 h_c^2\right) = \ln F - \ln H_0 - \frac{Q}{RT} \qquad (6\text{-}5)$$

where the constant C_1 relating the penetration depth and projected area has the value 24.5 [6.10]. For metals, C_1 can be easily calculated using the triangular function, since the contact area is followed by the shape of Vickers indenter

with face-to-face angle of 136[a].

It is difficult to determine H_0, the intrinsic hardness in equation (6-5), at absolute zero (*0 K*). We thus use the results of Tse's study [6.37], according to which the intrinsic hardness of a material is proportional to its shear modulus, *G*. Therefore, after replacing H_0 with *G* and writing *G* as a combination of elastic modulus (*E*) and Poisson's ratio (*v*), equation (6-5) becomes:

$$\ln\left(C_1 h_c^2\right) = \ln\left(\frac{1}{C_2}\cdot 2(1+v)\cdot\frac{F}{E}\right) - \frac{Q}{RT} \qquad (6\text{-}6)$$

where C_2 is a proportional constant connecting the intrinsic hardness and shear modulus. The *F/E* term in equation (6-6) can be changed by the tensile test parameters of the cross-sectional area (A_{ten}) and original length (l_0), and the changed length (δ) according to Hooke's law. We thus obtain:

$$\ln\left(C_1 h_c^2\right) = \ln\left(\frac{A_{ten}}{C_2}\cdot 2(1+v)\cdot\frac{\delta}{l_0}\right) - \frac{Q}{RT} \qquad (6\text{-}7)$$

$$\frac{\delta}{l_0} = \frac{\delta_e}{l_0} + \frac{\delta_p}{l_0} \qquad (6\text{-}8)$$

The most important part in equation (6-7) is δ/l_0, which can be divided into

strain in the elastic range (δ_e/l_0) and strain in the plastic range (δ_p/l_0), because the force F in equation (6-6) influences both the elastic and plastic deformation. The δ/l_0 in equation (6-8) is a tensile parameter and thus must be replaced by parameters with IIT. Because δ/l_0 cannot be obtained by IIT directly. In the tensile stress-strain curve, the elastic strain (δ_e/l_0) is the same as the yield strain, which equates to the ratio of yield stress and elastic modulus.

According to work by Tabor [6.38] and Chen [6.39], the tensile parameter (σ_{ys}/E) is relevant to the (h_{max}-h_f) /h_{max} parameter in IIT because (h_{max}-h_f)/h_{max} represents the degree of elastic deformation of material during IIT. Thus, the elastic parameter δ_e/l_0 in equation (6-8) can be expressed as equation (6-11) of IIT by equations (6-9) and (6-10):

$$\frac{\delta_e}{l_0} = \frac{l_0 - l_e}{l_0} = 1 - \frac{l_e}{l_0} = \varepsilon_{ys} = \frac{\sigma_{ys}}{E} \qquad (6\text{-}9)$$

$$\frac{\sigma_{ys}}{E} \approx \frac{h_{\max} - h_f}{h_{\max}} = 1 - \frac{h_f}{h_{\max}} \qquad (6\text{-}10)$$

$$\therefore \left(1 - \frac{l_e}{l_0}\right) = C_3\left(1 - \frac{h_f}{h_{\max}}\right) \qquad (6\text{-}11)$$

In equation (6-9), δ_e is the change in length from the original length (l_0) to the

elastically deformed length (l_e) in tensile specimen; in equation (6-10), σ_{ys} is yield stress, E is elastic modulus, h_{max} is the maximum indentation depth, and h_f is the final indentation depth after specimen unloading.

Equations (6-9) and (6-10) have the same physical dimensions because they describe deformation in the elastic range. Therefore, one can infer that they can be related to each other as in equation (6-11), where C_3 is a proportional constant. When elastic deformation part of equation (6-8) is expressed as equation (6-11), equation (6-7) becomes

$$\ln\left(C_1 h_c^2\right) = \ln\left[\frac{A_{ten}}{C_2}\cdot 2(1+\nu)\cdot\left(C_3\left(1-\frac{h_f}{h_{\max}}\right)+\frac{\delta_p}{l_0}\right)\right]-\frac{Q}{RT} \qquad (6\text{-}12)$$

Equation (6-12) shows that the part of elastic deformation of equation (6-7) is changed to the IIT parameter, and the part of plastic deformation is described as the tensile test parameter.

If C_1 on the left is taken to the right side, the indentation contact area can be expressed as a function of temperature and the IIT depth parameters (h_{max} and h_f):

$$\ln h_c^{2(HT)} = -\frac{Q}{R}\cdot\frac{1}{T} + \ln\left[\frac{\frac{A_{ten}}{C_2}\cdot 2(1+v)\cdot\left(C_3\left(1-\frac{h_f^{HT}}{h_{\max}^{HT}}\right)+\frac{\delta_p}{l_0}\right)}{C_1}\right] \qquad (6\text{-}13)$$

6.3.3.3. Determining activation energy and material constants

Equation (6-13) is a linear function, and thus, it is possible to determine the activation energy of the specimens from the squared term of indentation contact depth and temperature. R is a gas constant with value 8.314 $J{\cdot}K^{-1}{\cdot}mol^{-1}$.

Fig. 6.3 shows the relationship between the square of the indentation contact depth (h_c^2) and the temperature. Indentation contact depth (h_c) refers to the true depth taking into account pileup and sink-in effects. The linearity of this relationship implies two things. First, the activation energy can be determined from the slope. Second, the y-intercept indicates the value of parts containing the indentation variables in equation (6-13). The analytic results of Fig. 6.3 are summarized in Table 6.3.

The results in table 6.3 are interesting. For specimens, the activation energies produced during IIT can have various values, whereas the values of the y-intercept are similar. Considering that the specimens used in this study all have the BCC structure, this is very impressive. Activation energy affects many aspects of a material, including dislocation movement, diffusion, and recrystallization. Table 6.3 shows that although the crystal structure is identical, the reaction of each specimen to heat is markedly different.

In contrast, it is seen that having similar y-intercept values means that the reactions of specimens to an external force are similar even at high temperatures. Thus, the effect of external force in high-temperature IIT appears to be static,

whereas the effects of heat seem to be much more dynamic.

Since the activation energy has been determined by the slope of the data, the rest of equation (6-13) can also be determined. Both sides of equation (6-13) are divided into *Q/RT* to determine the part containing indentation parameters as a logarithm shape. Then, both the left and right sides involve temperature: in terms of deformation and temperature, the physical dimensions are identical on both sides.

Fig. 6.4 shows the plot after dividing the left and right sides of equation (6-13) into the activation energy and temperature. Here the values of the activation energy used are those in Table 6.3.

The square of the indentation depth including the temperature from the results of Fig. 6.4 is known to have a good linear relationship with the IIT parameters. Using this linearity, the following equation can be derived by modification of equation (6-13):

$$\frac{\ln h_c^{2(HT)}}{\left(-\frac{Q}{R}\cdot\frac{1}{T}\right)}+1=-2.83564\times\left[\frac{\ln\left(1-\frac{h_f^{HT}}{h_{\max}^{HT}}\right)}{\left(-\frac{Q}{R}\cdot\frac{1}{T}\right)}\right]-9.78901 \qquad (6\text{-}14)$$

Each undetermined parameter (C_1, C_2, C_3, A_{ten}, ν, δ_p/l_0) in equation (6-13) has been determined by plotting results of Fig. 6.4 as the constant 2.83564 and

9.78901 in equation (6-14). These constants contain the meaning of the elastic and plastic deformation of specimens in the IIT process, beyond the simple plotting constants.

In order further to generalize equation (6-14), the most unnecessary variable in terms of practicality is the activation energy. (Just for the record, it is for practical use, not for physical use.) As shown in Table 6.3, activation energy has various values depending on the specimen. However, for the materials studied here, it is known that the deviations of six types of specimens (excluding S45 and AISI 52100) are at least relatively low. Therefore, in practical terms, the values of activation energies are assumed to be constant at their mean value (excluding S45C and AISI 52100). The average slope of SKS3, SKH51, AISI D2, SKD61, AISI W1 and SCM21 can be defined as -60.1, and the mean of the activation energy can be defined as 499.43. Using these assumptions simplifies the shape of equation (6-14).

After substituting -60.1 into $-Q/R$ in equation (6-14) and rearranging terms, we have:

$$\ln h_c^{2(HT)} = -2.83564 \cdot \ln\left(1 - \frac{h_f^{HT}}{h_{\max}^{HT}}\right) + \left(588.319 \cdot \frac{1}{T}\right) \qquad (6\text{-}15)$$

Multiplying the exponential on both sides of equation (6-15) produces:

$$h_c^{2(HT)} = e^{-2.836 \cdot \ln\left(1 - \frac{h_f^{HT}}{h_{\max}^{HT}}\right) + \left(588.319 \cdot \frac{1}{T}\right)} \qquad (6\text{-}16)$$

Equation 6-16 is the final form proposed in this study. Using equation 6-16, it is possible to ignore the effects of pileup and sink-in, which introduce difficulties in calculating the exact contact area in IIT. Since (h_c^2) can be obtained directly, we need no longer attempt to measure or calculate pileup height and sink-in depth. If only the maximum indentation depth (h_{max}), the final indentation depth (h_f) and the testing temperature are measured from the IIT equipment, the contact area at high temperature can be calculated directly.

Multiplying the above-mentioned constants, 24.5 for the projected area or 26.43 for the surrounding area [6.16], by the calculated h_c^2 yields the contact area. In addition, the hardness is also easily calculated by dividing applied load in IIT by the contact area.

Table 6.4 compares the contact area determined by equation (6-16) with that measured by optical microscope. Representative results among the eight types of specimens tested, those for SKD61, are shown. Other specimens, including SKD61, can also be found to match within 10% error range in comparison with the contact area. Typical trends in the percent error in contact area are up to 13%~14% at 273 *K* and 373 *K*. However, at temperatures above 473 *K*, contact area errors are less than 10%.

In addition, Table 6.5 show the Vickers hardness errors between those calculated by equation (6-16) and those measured by optical microscope at another institution (FCTIC, as mentioned above) at the experimental temperature used here. The typical error in hardness is under 10%. The reason why fewer errors occur in the hardness than in the contact area is that, since hardness is defined as load divided by contact area, it is a normalized value and mathematical ratio. Hence, of course, the error range is inevitably smaller. The results in Table 6.5 indicate that the modified Westbrook's equation found in this study can give an accurate estimate of the Vickers hardness for the materials studied and can be used to calculate other material properties, such as elastic modulus, tensile properties, and residual stress at high temperature.

6.4. Summary

High-temperature deformation characteristics are investigated by the hardness and load-depth curves as measured by IIT. It is found that the effects of deformation temperature on the hardness of the specimens studied are more significant than effects of external applied force. Due to the mutually competitive mechanisms of work hardening and recovery, hardness values typically decrease with increasing temperature, and these trends are also well reflected in the IIT load-depth curve. Moreover, the unusual phenomenon of increasing hardness with increasing temperature is also well reflected in the IIT curve.

These experimental results suggest modification of Westbrook's equation. The modified relationship obtained here, which expresses the effects of heat and force on hardness and temperature is newly suggested.

Additionally, a comprehensive relation equation is developed to describe the contact area in IIT at high temperatures. It is confirmed that the contact area from the newly defined hardness-temperature relation can be expressed by a combination of testing temperature and indentation depth parameters.

The good agreement between the measured and calculated contact areas indicates that the equation developed here can accurately estimate the Vickers hardness for eight types of BCC, Cri-Mo alloy steels.

Table 6.1 Chemical composition of specimens [%]

	C	Cr	Cu	Fe	Mn	Ni	P	Mo	Si	S	W	V
SKS3	0.9	0.54	-	96	1.2	-	0.03	-	0.5	0.03	0.5	0.3
S45C	0.42	0.2	0.30	98.06	0.60	0.20	0.03	-	0.15	0.04	-	-
SKH51	0.85	4.15	-	81.02	0.30	-	-	5.0	0.30	0.03	6.4	1.95
AISI D2	1.55	11.8	-	84.35	0.40	-	-	0.80	0.30	-	-	0.80
AISI E52100	0.98	1.3	-	97.28	0.25	-	0.02	-	0.15	0.02	-	-
SKD61	0.39	5.2	-	90.60	0.40	-	-	1.4	1.1	0.002	-	0.9
AISI W1	0.6	0.15	-	98.65	0.25	-	0.025	-	0.2	0.025	-	0.1
SCM21	0.48	0.80	-	98.25	0.75	-	0.03	0.2	0.2	0.04	-	-

Table 6.2. Material constants from Westbrook's model

	A	B	H^{RT}
SKS3	221.132	-4.75789E-4	195
S45C	193.8317	-3.56812E-4	171
SKH51	259.0264	-5.31223E-4	222
AISI D2	256.3414	-4.89235E-4	230
AISI E52100	225.1169	-4.81145E-4	199
SKD61	221.7787	-4.57683E-4	201
AISI W1	195.4902	-5.4488E-4	165
SCM21	141.0635	-1.86108E-4	137

Table 6.3. Activation energy of specimens

Specimen	Slop	*y*-axis intercept	Q (J/mol)
SKS3	-59.4	8.88	493.61
S45C	-28.2	8.82	234.34
SKH51	-87.4	8.89	726.29
AISI D2	-40.3	8.77	334.89
AISI E52100	-96.2	9.01	799.42
SKD61	-60.3	8.90	501.09
AISI W1	-65.0	8.93	540.15
SCM21	-48.2	8.94	400.54

Table 6.4. Comparison of A_c from equation (6-16) with that found by optical observation

Specimen	T [*K*]	Ac from eq. (16) [μm^2]	Ac from O.M [μm^2]	Error (%)
SKD61	273.15	5464.595	6138.245	10.97
	373.15	6927.118	6109.918	-13.37
	473.15	6355.809	6416.477	0.95
	573.15	6367.589	6930.349	8.12
	673.15	7255.026	6694.386	-8.37
	773.15	7471.109	6796.956	-9.92
	873.15	7061.27	6898.525	-2.36

Table 6.5. Comparisons of calculated and measured Vickers hardness

Specimen	T [*K*]	H_v from eq.(16)	H_v from O.M [FCTIC]	Error (%)
SKS3	273.15	187.90	195.1	3.69
	473.15	183.34	170.3	-7.66
	673.15	182.09	170.12	-7.04
	873.15	135.35	142.12	4.76

Specimen	T [*K*]	H_v from eq.(16)	H_v from O.M [FCTIC]	Error (%)
S45C	273.15	150.20	170.9	12.11
	473.15	176.05	160.87	-9.44
	673.15	177.84	171.96	-3.42
	873.15	125.24	131.76	4.95

Specimen	T [*K*]	H_v from eq.(16)	H_v from O.M [FCTIC]	Error (%)
SKH51	273.15	205.23	221.82	7.48
	473.15	190.95	202.34	5.63
	673.15	176.48	185.02	4.62
	873.15	150.37	160.38	6.24

Specimen	T [*K*]	H_v from eq.(16)	H_v from O.M [FCTIC]	Error (%)
AISI D2	273.15	243.47	229.58	-6.05
	473.15	242.53	193.24	-25.51
	673.15	201.32	190.42	-5.73
	873.15	150.79	166.5	9.44

Specimen	T [*K*]	H_v from eq.(16)	H_v from O.M [FCTIC]	Error (%)
AISI E52100	273.15	176.24	198.68	11.29
	473.15	189.25	176.9	-6.98
	673.15	151.19	164.02	7.82
	873.15	133.43	147.84	9.75

Specimen	T [*K*]	H_v from eq.(16)	H_v from O.M [FCTIC]	Error (%)
SKD61	273.15	222.60	200.6	-10.97
	473.15	186.51	170.9	-9.13
	673.15	152.53	165.3	7.72
	873.15	136.51	149.5	8.69

Specimen	T [*K*]	H_v from eq.(16)	H_v from O.M [FCTIC]	Error (%)
AISI W1	273.15	149.31	165.4	9.73
	473.15	163.21	144.6	-12.87
	673.15	156.86	156.2	-0.43
	873.15	110.54	112.1	1.39

Specimen	T [*K*]	H_v from eq.(16)	H_v from O.M [FCTIC]	Error (%)
SCM21	273.15	118.80	137.22	13.42
	473.15	139.70	125.57	-11.25
	673.15	126.45	122.84	-2.94
	873.15	109.55	122.1	10.28

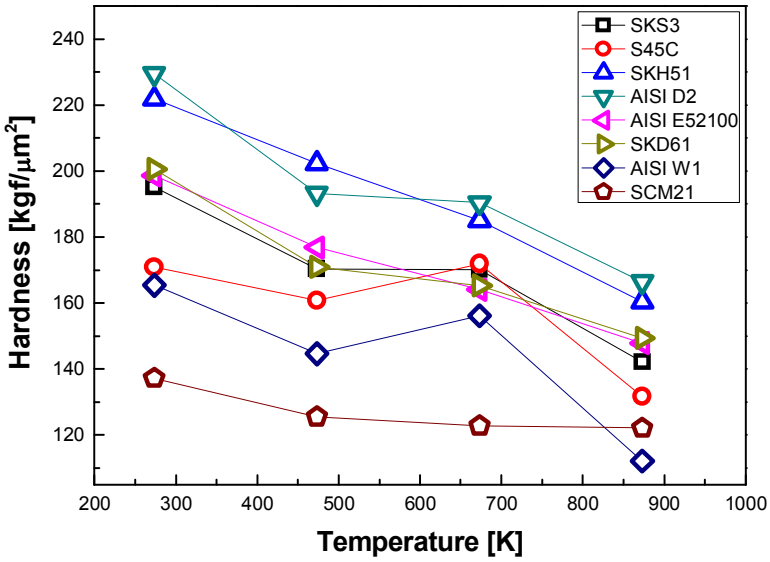

Fig. 6.1 Variation of hardness with temperature

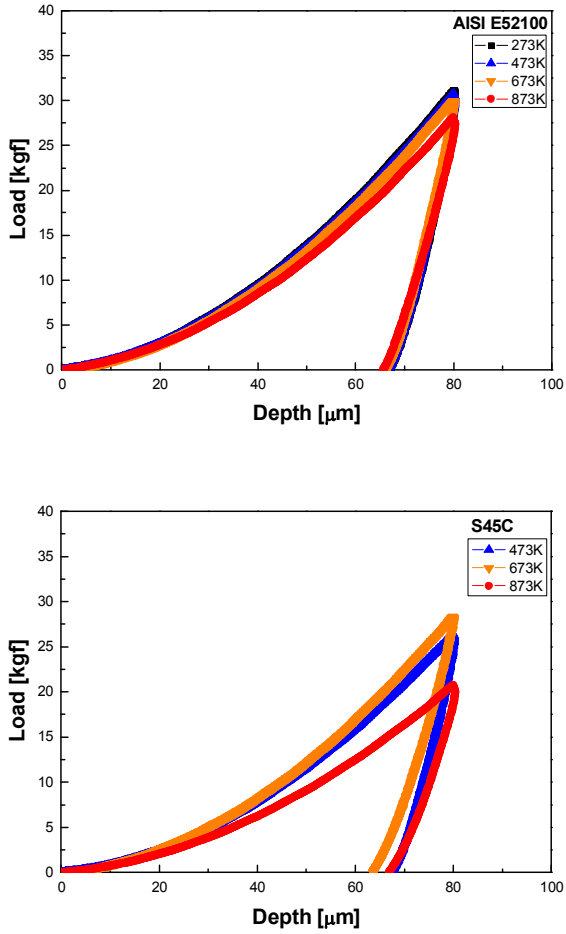

Fig. 6.2 Load-depth curve at different temperatures: (a) AISI E52100; (b) S45C

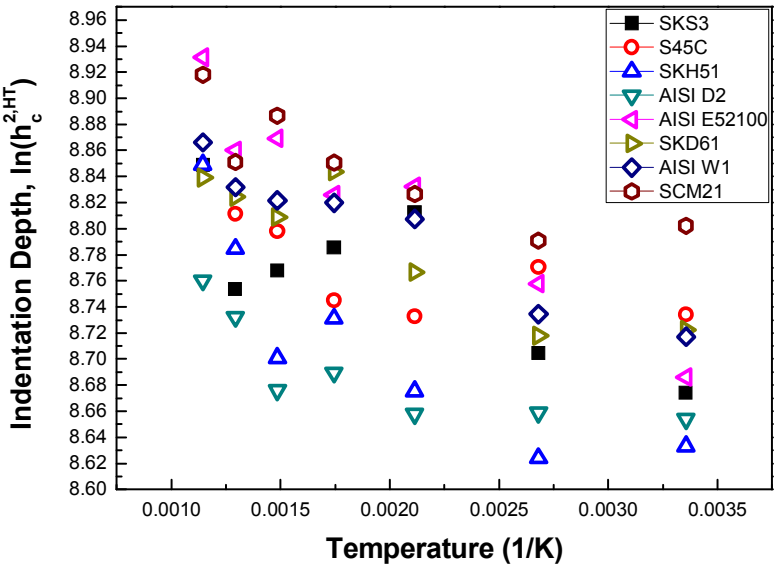

Fig. 6.3 Logarithmic square of indentation depth plotted against inverse temperature

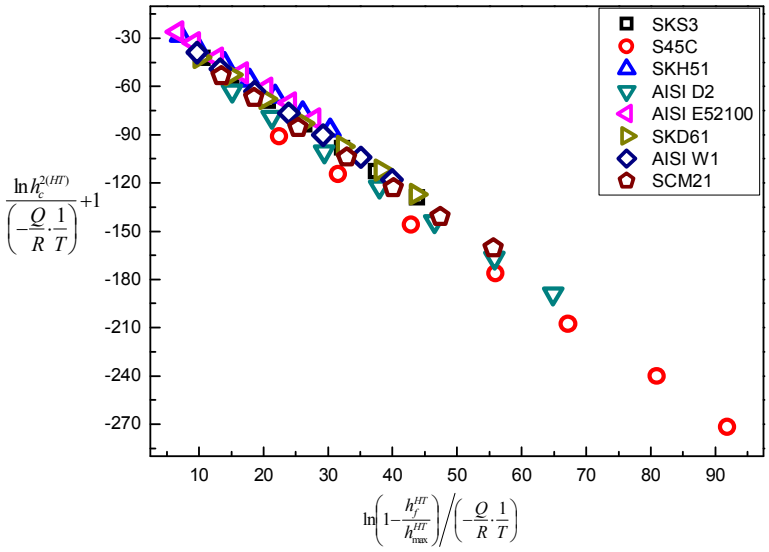

Fig. 6.4 Relationship between the square of indentation depth and the IIT parameters, including temperature

References

[6.1] Danijela Anica Skobir,Matjaz Godec,a Monika Jenkoa and Bostjan Markoli; Characterization of the carbides in the steel X20CrMoV12.1 used in Thermal power plants; *Surf. Interface Anal*. 40, (2008), 513–517

[6.2] W. L. MankinsJ. C. HosierT. H. Bassford; Microstructure and phase stability of INCONEL alloy 617; *Metallurgical Transactions*, 5, (1974), 2579 -2590

[6.3] V. A. Popovich, M. P. F. H. L. van Maris, M. Janssen, I. J. Bennett, I. M. Richardson; Understanding the properties of silicon solar cells aluminium contact layers and its effect on mechanical stability; *Materials Sciences and Applications*, 4, (2013), 118-127

[6.4] D. R. Kim, S. M. Yang and H. S. Y; Material property evaluation of high temperature creep for Pb-free solder joints of Sn-Ag-(Cu) types; *KSME*, (2012), 313-318

[6.5] E. R. Petty; Hardness and Other Physical Properties of Metals in Relation to Temperature; *Metallurgia*, 56, (1957), 337, 231-236.

[6.6] D. Tabor; A simple theory of static and dynamic hardness; *Proc R Soc. London A* 192, (1948), 247–274.

[6.7] Kirity Bhusan Khan, T. R. G. Kutty, M. K. Surappa; Hot hardness and indentation creep study on Al-5% Mg alloy matrix-B_4C particle reinforced composites; *Materials Science and Engineering A* 427, (2006), 76-82.

[6.8] Yichun Zhang, Tielin Shi, Zirong Tang, Guanglan Liao; An improved method to estimate Young's modulus of Zr-based BMGs accounting for pile-up during nanoindentation; *Journal of Non-Crystalline Solids*, 427, (2015), 20-25.

[6.9] Chan-Pyoung Park, Jung-Jun Lee, Seung-Kyun Kang, Young-Cheon Kim, Kwan-Sik Woo, Seung-Won Jeon, Dongil Kwon; Evaluation of high-temperature Vickers hardness using instrumented indentation system; *Materials Science and Engineering A*, 650, (2016), 15-19.

[6.10] W. C. Oliver, G. M. Pharr; An improved technique for determining hardness and elastic-modulus using load and displacement sensing indentation experiments; *J. Mater. Res*, 7, (1992), 1564.

[6.11] J. H. Westbrook; Temperature dependence of hardness of the equi-atomic iron group aluminides; *Journal of the Electrochemical Society*, 103, (1956), 54-63.

[6.12] George E. Dieter; Mechanical Metallurgy; *McGraw-Hill Book Company (UK) Si Metric Edition*, (1988).

[6.13] Chin-You Hsu, Woei-Ren Wang, Wei-Yeh Tang, Swe-Kai Chen and Jien-Wei Yeh; Microstructure and mechanical properties of new AlCoxCrFeMo0.5Ni high-entropy alloys; *Advanced Engineering Materials*, (2010), 44-49

[6.14] J.S. Lee, J.I. Jang, B.W. Lee, Y. Choi, S.G. Lee, D. Kwon; An instrumented indentation technique for estimating fracture toughness of ductile materials: A critical indentation energy model based on continuum damage mechanics; *Acta Mater.* 54, (2006), 1101.

[6.15] Y. Choi, H.S. Lee, D. Kwon; Analysis of sharp-tip-indentation load-depth curve for contact area determination taking into account pile-up and sink-in effects; *J. Mater. Res*. 19, (2004), 3307.

[6.16] S.K. Kang, J.Y. Kim, C.P. Park, H.U. Kim, D. Kwon; Conventional Vickers and true instrumented indentation hardness determined by instrumented indentation test; *J. Mater. Res*. 25, (2010), 2.

[6.17] T. Maki, I. Tamura; Deformation behaviors of metals and alloys at Elevated temperatures: 2. dynamic recrystallization and its related phenomena; *Journal of the Society of Materials Science*, 30, (1981), 329, 211-217

[6.18] S. E. Ion, F. J. Humphreys, S. H. White; Dynamic recrystallisation and the development of microstructure during the high temperature deformation of magnesium; *Acta Metallurgica*, 30, (1982), 10, 1909-1919.

[6.19] H. D. Merchant, G. S. Murty, S. N. Bahadur, L.T. Dwivedi, Y. Mehrotra;

Hardness-temperature relationships in metals; *Journal of Materials Science*, 8, (1973), 437-442

[6.20] Akio Kagawa, Taira Okamoto, Kazuo Saito, Minoru Ohta; Hot hardness of $(Fe, Cr)_3C$ and $(Fe, Cr)_7C_3$ carbides; *Journal of Materials Science*, 19, (1954), 2546-2554

[6.21] V. A. Borisenko; Investigation of the temperature dependence of the hardness of molybdenum in the range of 20-2500°C; *Translated from Poroshkovaya Metallurgiya*, 2, (1962), 55-61.

[6.22] Chin-You Hsu, Woei-Ren Wang, Wei-Yeh Tang, Swe-Kai Chen and Jien-Wei Yeh; Microstructure and mechanical properties of new AlCoxCrFeMo0.5Ni high-Entropy alloys; *Advanced Engineering Materials*, 12, (2010), 44-49.

[6.23] Schweitzer, E; Goken, M; The grain boundary hardness in austenitic stainless steels studied by nanoindentations; *Zeitschrift Fur Metallkunde*, 95, (2004), 492-498.

[6.24] Kittel, Charles, Herbert Kroemer; Thermal Physics 2nd edition; *New York Freeman and Company*, (1980).

[6.25] Arrhenius, S.A.; Über die Dissociationswärme und den Einfluß der Temperatur auf den Dissociationsgrad der Elektrolyte; *Z. Phys. Chem.* **4,** (1889), 96–116.

[6.26] Zener, C., Hollomon. J. H; Effect of strain rate upon plastic flow of steel; *Journal of Applied Physics*, 15, (1944), 22-32.

[6.27] C. M. Sellars, W. J. Mc Tegart; On the mechanism of hot deformation; *Acta Metallurgica*, 14, (1966), 1136-1138.

[6.28] Z. S. Basinski; Activation energy for creep of aluminium at sub-atomspheric temperature; Acta Metallurgica, 5, (1957), 684

[6.29] V. Vitek and F. Kroupa; Dislocation theory of slip geometry and temperature dependence of flow stress in B. C. C. Metals; *Phys. Stat. Sol.* 18, (1966), 703

[6.30] George-Maria Schwab; Some new aspects of the strength of alloys;

Transactions of the Faraday Society, 45, (1949), 385.

[6.31] O. D. Sherby and P. E. Armstrong; Prediction of activation energies for creep and self-diffusion from hot hardness data; *Metallurgical Transactions*, 2, (1971), 3479.

[6.32] S.I. Bulychev, V.P. Alekhin, M.K. Shorshorov, A.P. Ternovskii, and G.D. Shnyrev; Determining Young's modulus from the indentor penetration diagram; *Zavod. Lab*. 41, (1975), 1137.

[6.33] M.F. Doerner and W.D. Nix; A method for interpreting the data from depth-sensing indentation instruments; *J. Mater. Res*. 1, (1986), 601.

[6.34] J.L. Bucaille, S. Stauss, E. Felder, and J. Michler; Determination of plastic properties of metals by instrumented indentation using different sharp indenters. *Acta Mater*. 51, (2003), 1663.

[6.36] Yun-Hee Lee and Dongil Kwon; Residual stresses in DLC/Si and Au/Si systems: Application of a stress-relaxation model to the nanoindentation technique*; J. Mater. Res*, 17, (2002), 901-906.

[6.37] J. S. Tse; Intrinsic hardness of crystalline solids; *Journal of Superhard Materials*, 32, (2010), 177-191.

[6.38] N. A. Stilwell and D. Tabor; Elastic recovery of conical indentations; *Proc.Phys. Soc*. 78, (1961), 169.

[6.39] Y.T. Cheng and C.M. Cheng; Relationships between hardness, elastic modulus, and the work of indentation. *Appl. Phys. Lett*. 73, (1998), 614.

Chapter 7

Prediction of Load- Depth curve at High-Temperature

Contents

7.1. Introduction

Instrumented indentation testing (IIT) can be used to measure many mechanical properties, from basic properties such as elastic modulus and hardness [7.1] to advanced properties such as tensile properties, fracture toughness, fatigue and creep [7.2-7.5], by measuring the penetration depth from the material surface in loading and unloading. IIT's strongest advantage over conventional mechanical testing is that the specimen volume it requires is very small. This characteristic of IIT yields the merits of simplicity, economic, non-destructiveness, and in-field application. Thus, IIT can be applied to materials from metal alloys to amorphous materials and biological materials [7.6-7.9], and also can be used at scales from macro to micro/nano [7.10-7.11]. However, IIT studies have mostly been carried out at room-temperature: research in special environments such as high-temperature, low-temperature, or corrosion is relatively sparse. The reasons for this are, for example, that thermal drift (the temperature difference between indenter and specimen) can lead to error in mechanical measurements, making it difficult to obtain stable experimental data [7.12]. Therefore, while the internal stress and strain distribution and deformation mechanisms caused by the indenter have been thoroughly investigated experimentally and by the finite-element method at room-temperature [7.13, 7.14, 7.15], at high-temperatures these data are not yet clearly established. The insufficient experimental data and research on high-

temperature mechanisms have also hampered exploration of the constitutive equation.

Typically, in high-temperature tensile testing, the Johnson-Cook constitutive equation is established, and many studies have validated this model [7.16, 7.17]. In the Johnson-Cook model, the hardening and softening behavior of the material can be described and the stress-strain curve at high-temperature can be predicted empirically. However, although IIT has many advantages, it lacks a typical constitutive equation, even a load-displacement equation, at high-temperatures. It is very important to predict the load and the resulting strain at high-temperatures, since in order to design new materials safely we must know their mechanical behavior in advance. In addition, the best way to evaluate the high-temperature mechanical properties of structures already in use is to test at the actual use temperature, but this is inevitably a destructive process. Therefore, if the mechanical behavior at the actual service temperature can be predicted, then a structure's replacement period can be assessed by considering just the operating time. In other words, the structure's life-time can be evaluated in a nondestructive manner. Therefore, this study addresses the use of IIT in predicting/describing instrumented indentation load-depth curves at high-temperatures. To our knowledge, this is the first attempt in this area in the indentation research field. If high-temperature load-depth curves can be accurately predicted, the mechanical properties at the actual service temperature of the structure can be assessed nondestructively and locally, so vulnerable parts

can be identified and the effective lifetime determined. In addition, this study combines thermodynamic theory with current mechanical indentation theory, contributing to the convergence of the two disciplines.

In this study, the IIT process (loading and unloading in combination with temperature effects) is newly interpreted in terms of thermodynamics. First, the concept of indentation work, defined in Cheng and Cheng [18], can be extended to resilience as a mechanical parameter. The relationship with stiffness, which can be obtained from the unloading curve of IIT, can also be investigated. Second, we investigate the relationship between stiffness and internal energy, a thermodynamic parameter, and conclude that internal energy, which is based on quantum mechanics, is also dependent on elasticity. Third, the relationship between the stiffness and the Helmholtz free energy (hereafter simply Helmholtz energy) can be explored by analyzing the flow of entropy during loading and unloading in IIT at high-temperatures. That is, after IIT, the entropy contributing to the elastic recovery of the impression mark is derived, and it is confirmed that the mechanical and thermodynamic factors can be combined through the entropy. (Here the Helmholtz energy is another converted form of internal energy, as explained in detail in the discussion.) Finally, the load-depth (L-h) curve at high- temperatures can be predicted by the change in indentation depth according to temperature and the stiffness-Helmholtz energy relationship. Also, a method for calibrating the predicted L-h curve is suggested using the

maximum load of IIT measurable at room-temperature. The predicted high-temperature *L-h* curve is verified by comparison with the measured *L-h* curve.

7.2. Experiments

7.2.1. Specimens

SKS3, SKH51, SKD11, SUJ2, SKD61 and SK3 are the primary high-temperature materials used here. These high-carbon tool steels contain 0.6~1.5% carbon with few impurities and have suitable hardness and strength to withstand plastic working above 573 K. We use these six body-centered cubic (BCC) metal alloys to derive the relationship between stiffness (a mechanical parameter) and inverse Helmholtz energy (a thermodynamic parameter) and thus to predict the *L-h* curve at high-temperatures. Uniaxial tensile tests were carried out at room -temperature using ASTM standard E8/E8M (2016) to obtain the basic mechanical properties of these materials. The results are summarized in Table 1. In addition, samples of S45C (also BCC) were tested to validate the study results.

7.2.2. Differential scanning calorimeter (DSC) testing

The differential scanning calorimeter (DSC) measures the energy of a specimen undergoing a physical or chemical change under constant pressure; here energy takes the form of the heat entering and exiting the specimen. That is, this test using the zeroth law of thermodynamics (the law of thermal equilibrium) measures the behavior of a reference material that does not undergo any change with increasing temperature and the behavior of a changing specimen. DSC was conducted on a Netzsch machine (model 200 F3 Maia, Germany); sapphire was the reference material. SKS3, SKH51, SKD11, SUJ2, SKD61, SK3 and S45C were the target specimens. Disc-shaped small specimens were used of diameter 0.5 mm and thickness 0.075 mm. The specimens were carefully laser-cut to have similar size and mass to sapphire, the reference material. The mass of the specimen was measured using an electronic scale; the average value was 0.01 g. The specimens and the sapphire were heated from room-temperature to 773.15 K by conduction and the heat flow into and out of the system were measured. The heating rate was set at 5 K/min and thus required an experimental time of 100 minute per specimen. Heating was done by flowing current to the pan and liquefied N_2 was used for accurate temperature implementation. Heat flow, Q/t, can be obtained from DSC, where Q is heat and t is time. The heating rate, $\Delta T/t$, can be obtained, where ΔT is the increase in temperature. The heat capacity, C_p, can be obtained under constant pressure (1 atm) from Q and ΔT. The internal

energy can be obtained by using the first law of thermodynamics ($\Delta U=Q-W$), where ΔU is the internal energy and W is the work done on the surroundings by the system. Work is the product of the pressure and volume change in the system; here the system is the specimen, the pressure is constant at 1 atm, and the volume change is calculated using the thermal expansion coefficients in the literature [7.19]. The internal energy obtained from DSC can be converted into Helmholtz energy using a Legendre transformation. Since ΔQ and T are measurable, the entropy change of the entire specimen can be obtained using classical thermodynamics' second law ($\Delta S=\Delta Q/T$), where ΔS is the change in entropy.

7.2.3. Instrumented indentation testing (IIT)

7.2.3.1. Room-temperature IIT

Instrumented indentation testing evaluates a variety of mechanical properties from the load–depth curve, a continuous record of indentation depth, load and unloading at an indenter. The following specimens were used to investigate the relationship between IIT work, resilience, and stiffness: seventeen kinds of BCC and FCC steels (SKD11, SKD61, SK4, SCM415, SCM440, SUJ2, S45C, S20C, SUS410, SUS420J2, SUS440C, SUS303, SUS304, SUS304L, SUS316, SUS316L, Ti-6Al-4V). For room-temperature IIT, 20 × 20 × 20-mm specimens were machined and the surface was finely polished using 1 μm alumina powder. The testing equipment was Advanced Indentation System 2100 (AIS 2100), an instrumented indentation tester manufactured by Frontics Inc. to the ISO 14577-1 standard. A spherical tungsten carbide (WC) indenter of radius 0.25 mm was used. The maximum indentation depth was 150 μm and the indentation rate was 0.3 mm/min. The elastic modulus of *WC* is 600 GPa and its Poisson's ratio is 0.04. A 15-times multi-indentation test was performed in which the load was removed and reloaded every 50% of the indentation depth 10 μm.

7.2.3.2. High-temperature IIT

High-temperature IIT was conducted on the Frontics machine (model AIS2100, Korea) and self-developed high-temperature chamber [7.6] in which indenter and specimen are placed inside the chamber (Fig. 7.1). The inside of the chamber contained a halogen lamp, thermocouples and stage. The specimen oxidation and thermal draft reported in previous research [7.20-7.22] were prevented by vacuum conditions. Radiation shield and cool-water circulation system were set up around the stage and the IIT connecting shaft. All specimen faces were heated equally by the halogen lamp and the movement of the stage was controlled externally [7.6].

Although a diamond indenter is typically used, in this study, tungsten carbide was used because two problems arise with commercial Vickers indenters. First, the IIT at 573.15 K or more resulted in separation of the diamond portion from the SUS steel holder. Second, it was impossible to obtain from the manufacturer the mechanical properties of the diamond portion. Hence, the indenter and holder portion were integrally manufactured using tungsten carbide, which is quite hard, has little elasticity, has a high melting point (3,695 K) and deforms little at high-temperature. The indenter used was a tungsten carbide (WC) Vickers indenter with 136° face-to-face angles; tungsten carbide was chosen because it is quite hard, has little elasticity, has a high melting point (3,695 K) and deforms little at high-temperature. Its mechanical properties are the same

with the spherical indenter. Experiments were carried out to obtain the high-temperature mechanical properties and the load-depth curve. The specimens were, as in the DSC test, SKS3, SKH51, SKD11, SUJ2, SKD61, SK3 and S45C. Disc-shaped or rectangular bulk specimens were used, in accordance with ISO 14577-1 (2002). The disc-shaped specimens had diameter 40 mm and thickness 15 mm; the rectangular specimens had length 40 mm and thickness 15 mm. The indentation rate was constant at 0.3 mm/min [7.23, 7.24, 7.25] and indentation depth was 80 μm by the depth-control method. The temperature was varied at 100 K intervals from room-temperature to 773.15 K in 10^{-2} torr vacuum condition. The penetration depth (indentation displacement) was measured by the linear variable displacement transducer (LVDT) method.

At both room-temperature and high-temperatures, the impression contact area produced by IIT was measured with an optical microscope on an Akashi machine (model AVK-HF, Japan) and the stiffness, S^{IIT}, was obtained from the IIT load-depth curve. Here stiffness is defined as the measured slope, dL/dh, of the upper portion of the unloading curve, where L is load and h is depth [7.26]. Second, hardness was calculated by dividing the indentation load by the contact area, in accordance with ASTM standard ASTM E 92-82 (2003). Third, elastic modulus was calculated. According to Oliver-Pharr [7.26], the reduced elastic modulus of material can be calculated as the ratio of stiffness and contact area, $E_r = (\sqrt{\pi}/2)(S/\sqrt{A_c})$, This reduced elastic modulus, according to Sneddon [7.13, 7.38], is composed of the sum of material's elastic modulus and Poisson's

ratio and indenter's elastic modulus and Poisson's ratio, $1/E_r = (1 - v_s^2/E_s) + (1 - v_i^2/E_i)$, Hence the elastic modulus of a material can be calculated from the indenter's elastic modulus and Poisson's ratio.

7.3. Results

The heat capacity, C, of a material is defined as the amount of heat required to raise the temperature by 1 K when either the volume, C_v, or the pressure, C_p, is constant. The DSC test yields the heat capacity at constant pressure and the internal energy change due to the temperature change can be observed. The heat capacity of our specimens is summarized in Table 2.

The isobaric heat capacity can be obtained by dividing the heat entering and leaving the system by the temperature change. Here, since the pressure is constant, the heat quantity is the sum of the internal energy change and the work done by specimen on its surroundings (by the first law of thermodynamics). In general, for solid metals, the amount of work can be regarded as zero since the rate of thermal expansion is very small. Therefore, heat capacity is a temperature-dependent thermal property that increases and decreases as the temperature increases and decreases.

Figure 7.2 shows the heat capacity of the specimens as measured in this study. In most specimens, heat capacity and temperature have proportional relationship, but the SUJ2 specimen does not follow this proportional relationship in the 523 ~ 623 K range. Figure 7.3 shows the relationship between internal energy and temperature, obtained from heat capacity. Internal energy is a general term for all the energy inside the material. In thermodynamics, it means the sum of the kinetic energy and the potential energy of the oscillating atoms; in material

mechanics, it means the inter-atom or inter-lattice bonding energy. The exact physical meaning of a solid metal's internal energy is treated further in the discussion section below; we note here that it must take into account the quantization of atoms and the elastic property of the material. As can be seen . 7.3 the internal energy increases with increasing temperature. This does not violate the previous theory that the internal energy is temperature-dependent. However, we see that in the SUJ2 specimen, the internal energy decreases in the 523 K ~ 623 K range. The reduction of the heat capacity and the internal energy is the specific temperature range can be analyzed according to general thermodynamic theory and can be further explained by the research of Mustak [7.27]. According to thermodynamic theory, when pressure is constant, the heat capacity (Fig. 7.2) is the enthalpy, *H*. When material receive heat, its internal energy increases and at the same time its volume expands. At this point, the volume expansion can be defined as work. This work does not proceed indefinitely but continues only until the internal expansion of the specimen and the external contraction around it satisfy the equilibrium relation of the mechanical force. Therefore, in order to satisfy the first law, that the total energy is conserved, the works necessary for the internal expansion of the specimen and for its external contraction are equal and so they offset each other. Therefore, only other types of work can occur in the specimen, such as electrical and chemical work and phase transition. So, the fact that heat capacity and internal energy change in the 523 ~ 623 K range of SUJ2 indicates that work was

performed other than the volumetric expansion. According to Mustak [7.27], it can be inferred that the other work may be a phase transformation. Mustak investigated the temperature at which SUJ2 starts to undergo phase transformation from austenite into a martensite phase through actual heat-treatment experiments and computer simulation. The commercial SUJ2 material has an initial microstructure of pearlite, pro-eutectoid cementite, alloy carbide and partially austenite phases. These partially retained austenites are transformed into martensite phases by rearranging the carbide size and distribution to suit the intended use. According to [7.17], the austenite phase of SUJ2 begins to transform into the martensite phase at 473 ~ 523 K, and the lower the temperature, the higher the martensite fraction. Although, the temperature is somewhat different in Mustak's study and here (within ±150 K), it is worth highlighting that experimental data are usually compared not for exactly the same steel grade but for similar steel grades or for a family of steels. Also, since the dilatometer (DIL 805A/D, TA-Baehr) was used in [7.17] to measure the thermal properties, it is possible to explain why the heat capacity and internal energy of SUJ2 fluctuate at a certain temperature. The other five specimens (SKS3, SKH51, SKD11, SKD61 and SK3) are well described by the general principle that the heat capacity and internal energy increase with increasing temperature. Internal energy can be converted into Helmholtz free energy by using a Legendre transformation. Why we should use the transformed parameter is explained in Section 4 below.

Stiffness is defined as the degree to which a material resists a given strain when an external force is applied. However, in order fully to explore stiffness, it is necessary to consider the deformation of the material within the elastic range. Stiffness is proportional to elastic modulus and represents the degree of resistance to deformation per unit length. Therefore, a large stiffness means that the deformation-restoring force per unit length is large. Hardness, a more general concept than stiffness, includes a plastic deformation; it is obtained by dividing the load by the "area" deformed. Hardness has a good proportional relationship with yield strength and is often a convenient way to express mechanical property. Hardness also includes the concept of rigidity on the material's surface. Figures 7.4 and 7.5 show stiffness and hardness results, which decrease with increasing temperature. The degradation of mechanical properties with increasing temperature cannot be explained by a single mechanism, since many variables such as temperature, time, applied stress, strain rate, grain size, and precipitation must be considered. However, if, as in this study, the experimental conditions are fixed over a short time (within two minutes) and constant displacement, the degradation of mechanical properties can be explained as due to non-thermal and thermal stresses. To understand the mechanical properties of materials at high-temperature, it is necessary to consider both these stress components. In dislocation theory, the non-thermal stress is often called internal stress. This is because the obstacles to dislocation movement occur at such a long range that the dislocation cannot overcome them

despite thermal activation. (The thermal stress is often called effective stress, since the difference between the applied stress and the internal stress is effective on thermally activated dislocation motion [7.28].) No theory yet allows us to distinguish between internal stress and effective stress and determine their quantitative amounts. Previous studies [7.29-7.33] have found that both internal stress and effective stress are temperature dependent. As the temperature increases, the dislocation tries to find an equilibrium state. This dislocation behavior causes a recovery and recrystallization of the microstructure that reduces the internal stress. In addition, thermally activated dislocations can overcome stationary obstacles (or short-distance obstacle), thus reducing the effective stress. At this time, the dislocation easily glides into the area where the internal stress is lower than the effective stress. Therefore, the force required for causing deformation per unit length decreases gradually with increasing temperature, as in this study, and the deformation mechanism as a whole follows the stiffness behavior in Fig. 7.4. However, in Fig. 7.5, the hardness values of the SKS3 and SK3 specimens are somewhat higher at 673 K than 473 K. The internal stress decreases with increasing temperature, that is, the deformation resistance to external force gradually decreases, but this cannot explain the fact that the effective stress also shows the same tendency as the internal stress, since the effective stress reflects the influence of heat and external force. In metallic materials with regular lattice arrangements, the lattice atoms keep moving at high frequency and relatively small amplitude; that is, they are

continuously vibrating and moving to the lowest energy position as they do so. When energy is injected in the form of a sound wave, the vibrations become larger, and the electrons in the atoms are quantized with higher energy values and become unstable. When an external force is applied in this unstable state, the atoms move very easily to another position. This can lead to moving, proliferating, and entangling of dislocations, so the material can harden even at high -temperatures. Therefore, the temperature range in Fig. 7.5 in which the hardness increases can be regarded as the range in which this hardening mechanism works better than the softening mechanism. Thus the characteristic phenomenon may occur that the material does not always soften at high-temperature but rather hardens.

7.4. Discussion

7.4.1. Indentation work, resilience and stiffness

Unlike at room-temperature, the high-temperature deformation behavior of materials in indentation testing is difficult to explain fully using conventional contact theories and material mechanics because the dislocation motion that causes deformation is affected by the thermal energy. Therefore the IIT load-depth curve reflecting this reaction must also be interpreted in terms of thermal energy.

Attempts to analyze the *L-h* curve from the viewpoint of energy have been made by Giannakopoulos and Suresh [7.34] and Cheng and Cheng [7.35]. According to these studies, the area under the *L-h* curve is defined as indentation work, as shown in Fig. 7.6. The area under the loading portion of *L-h* curve is a measure of the total work, W_t^{IIT}, done by the indenter in deforming the material and the area under the unloading portion of the *L-h* curve, W_e^{IIT}, means work energy required for elastic recovery when removing load. W_t^{IIT} and W_e^{IIT} can be expressed as

$$\begin{cases} W_{total}^{IIT} = \int_0^{h_{\max}} f_L(h)dh = \int_0^{h_{\max}} C_1 h^2 dh \\ W_e^{IIT} = \int_{h_f}^{h_{\max}} f_U(h)dh = \int_{h_f}^{h_{\max}} C_2 h^2 dh \end{cases} \tag{7-1}$$

$$\frac{W_e^{IIT}}{W_{total}^{IIT}} \propto \frac{h_{\max} - h_f}{h_{\max}} \propto \frac{H}{E} \tag{7-2}$$

As shown in Fig. 7.6, the total W_t^{IIT} can be decomposed into elastic and plastic parts: $W_t^{IIT} = W_e^{IIT} + W_P^{IIT}$. In addition, the energy ratio defined in Eq. (7-2) can be expressed as a combination of h_{max} and h_f, the indentation parameters, and it can be seen that their ratio is proportional to the ratio of the hardness and elastic modulus.

Here the item to note is the work of elastic recovery, W_e^{IIT}. The area W_e^{IIT} in Fig. 7.6 means that the material recovers elastically after the load is removed (Fig. 7.7) and the material is said to have elastic behavior during the unloading process. So, if we assume for now that the material is a linearly elastic body, the interpretation of the unloading curve can be very convenient. In materials science, resilience, U_R, is the ability of a material to absorb energy under elastic deformation and to recover this energy on removal of the load: it is thus a measure of the ability of the material to hold a certain stress without permanent deformation. Hence resilience is called strain-energy density in material

mechanics. Strain-energy density is defined as the strain energy per unit volume, and is a kind of internal energy. In the stress-strain curve in tensile testing, the area under the material's elastic region indicates the material's resilience. In the tensile test, resilience is defined as:

$$U_R^{ten} = \int_0^{\varepsilon_{ys}} \sigma d\varepsilon \tag{7-3}$$

where U_R^{ten} is the resilience defined in tensile testing, σ is stress, and ε is strain. If we assume a linear stress-strain curve, Eq. (7-3) simplifies to

$$U_R^{ten} \cong \frac{1}{2}\sigma_{ys}\varepsilon_{ys} \tag{7-4}$$

If the material behavior is linearly elastic, Hooke's law ($\varepsilon_{ys} = \sigma_{ys}/E$) can be applied:

$$U_R^{ten} \cong \frac{1}{2}\frac{\sigma_{ys}^2}{E} \tag{7-5}$$

Using Tabor's observation that hardness is approximately three times the yield strength ($\sigma_{ys} \approx H/3$) [7.36] yields

$$U_R^{IIT} \cong \frac{1}{2}\frac{1}{9}\frac{H^2}{E_s} \qquad (7\text{-}6)$$

The U_R^{ten} defined in the tensile test can be redefined using the above derivation as the ratio of the square of hardness and elastic modulus, which can be obtained using IIT, as shown in Eq. (7-6) [7.37], where U_R^{IIT} is the newly defined indentation resilience. Considering that W_e^{IIT}/W_t^{IIT} is related to H/E and resilience is related to H^2/E, we see that the elastic recovery at unloading is related to resilience and can thus be represented by the same parameters H and E.

Figure 7.8 shows the relationship between W_e^{IIT} calculated from Eq. (7-1) and U_R^{IIT} calculated from Eq. (7-6). Since the physical meaning of recovery of the energy absorbed by the external force is the same, it can be experimentally confirmed that the two factors are proportional to each other: W_e^{IIT} of IIT and U_R^{IIT} of IIT are:

$$W_e^{IIT} \propto U_R^{IIT} \qquad (7\text{-}7)$$

If we take advantage of Oliver-Pharr's study [7.26], Eq. (7-6), which is defined using H^2/E, leads to interesting results. The behavior of the unloading curve in Fig. 7.6 and the contact area in IIT are defined in Eq. (7-8).

$$\begin{cases} L_{h-h_f} = C_1 \cdot (h - h_f)^2 \\ A_c = C_2 \cdot h_c^2 \end{cases} \tag{7-8}$$

$$\frac{1}{E_r} = \frac{(1-\upsilon_s^2)}{E_s} + \frac{(1-\upsilon_i^2)}{E_i} \tag{7-9}$$

$$S^{IIT} = \frac{dL}{dh} = \frac{2}{\sqrt{\pi}} E_r \sqrt{A_c} \tag{7-10}$$

In Eq. (7-8), the exponent depends on the indenter's geometric shape and has a value of 2 for Vickers, 1.5 for spherical, and 1 for flat indenters, and C_1 can be determined by a least-squares fitting procedure. C_2 takes values of 24.5 and 26.4, respectively, taking into account the projected area or surrounding area of the indentation mark [7.13, 7.26, 7.38]. The hardness in Eq. (7-6) can be expressed by the applied load and contact area. If the applied load is approximated as the load in the elastic range, the hardness can be approximated as:

$$H \approx \frac{L_{h-h_f}}{A_c} = \frac{C_1 \cdot (h - h_f)^2}{C_2 \cdot h_c^2} \tag{7-11}$$

In order to divide the square of the hardness in Eq. (7-6), the definition of reduced elastic modulus, E_r in Eq. (7-9) was used. E_s and E_i are the elastic

moduli of the specimen and the indenter, respectively, while v_s and v_i are the Poisson's ratios of the specimen and the indenter, respectively. We now substitute Eq. (7-11), approximating the hardness using the IIT variables, and Eq. (7-9), containing the elastic modulus of the specimen, into Eq. (7-6) to derive Eq. (7-12) below; note here that constants such as (1/2) (1/9) in Eq. (7-6) are omitted.

$$\frac{H^2}{E_s} \approx \frac{C_1^2 \cdot (h - h_f)^4}{C_2^2 \cdot E_r \cdot h_c^4 \cdot \left\{ \frac{E_i(1-\upsilon_s^2) + E_s(1-\upsilon_i^2)}{E_i} \right\}} \tag{7-12}$$

Since the stiffness, S^{IIT} in Eq. (7-10) includes a reduced elastic modulus term, the following Eq. (7-13) can be derived by replacing E_r in Eq. (7-12) by S^{IIT}:

$$\frac{H^2}{E_s} \approx \frac{1}{S^{IIT}} \cdot \frac{(h - h_f)^4}{h_c^3} \cdot \frac{C_1^2}{C_3} \cdot \frac{1}{\left\{ \frac{E_i(1-\upsilon_s^2) + E_s(1-\upsilon_i^2)}{E_i} \right\}} \tag{7-13}$$

As shown in Eq. (7-13), H^2/E, the IIT resilience, is proportional to the reciprocal of the stiffness. H^2/E is also affected by the combination of the IIT variables (h, h_f, h_c) and the elastic properties (E_i, E_s, v_i, v_s).

Figure 7.9 shows that H^2/E in Eq. (7-13) and stiffness are inversely proportional to each other. In general, resilience and stiffness are proportional,

assuming that yielding occurs at the same strain on the stress-strain curve. That is, high stiffness implies high resilience and low stiffness implies low resilience. However, in this study, indentation testing was consistently performed to the same depth. Therefore, the distributions of stress and strain of material under indenter are not the same. Also, the tendency of the inverse of the resilience and stiffness in Fig. 7.9 is consistent with the results of Roy et al. [7.37]. Roy coated diamond-like carbon (DLC) on magnesium-stabilized zirconium (Mg-PSZ) and cobalt-chromium alloy (CoCr) substrates to measure mechanical properties such as elastic modulus, resilience and plastic resistance ratio, H^3/E^2, using microhardness and nanoindentation testing. Theirexperimental data show a lower resilience value with higher elastic modulus and higher resilience with lower elastic modulus. Elastic modulus is the mathematical description of the stiffness of material, i.e., resistance to being deformed when a force is applied. Therefore, in this study, elastic work, resilience, and stiffness of IIT were found to be as follows in the experiments in Figs. 7.8 and. 7.9:

$$W_e^{IIT} \propto U_R^{IIT} \left(\approx \frac{H^2}{E_s}\right) \propto \frac{1}{S^{IIT}} \qquad \text{where } S^{IIT}\text{: stiffness} \tag{7-14}$$

In the meantime, the IIT academic world has studied how the energy ratio, W_t-W_e/W_t, is related to material's properties such as σ_{ys}/E or H/E. Because it is important to determine the precise contact area beforehand to evaluate the

hardness and elastic modulus, it is no longer necessary to calculate the complex elastoplastic deformation affecting the contact area (pileup, sink-in) by introducing the work of IIT as a parameter. However, Eq. (7-14) broadens our horizons in looking at the indentation curve: it presents two possibilities for its application.

The first possibility is that the elastic energy absorbed or released by an external force into the material can be derived from the area beneath the unloading curve. Conversely, if we know the elastic energy in advance, we can interpret or manipulate the unloading curve. The second is that elastic energy can be quantified using stiffness as a variable. Stiffness can be easily obtained from the initial slope of unloading curve, and thus the change in elastic energy can be seen through the change of stiffness. This is useful in applications: if we know the amount of elastic energy in advance, we can determine the slope of the unloading curve.

7.4.2. Relationship of internal energy and stiffness

Since the concept of internal energy is very comprehensive, it is often replaced by other terms depending on the academic field; in addition, the written parameters can differ with the field, as can their physical meaning. However, since material mechanics and thermodynamics are fused in this study, we must summarize our view of internal energy. Internal energy is defined as the sum of the various forms of energy in a system. The components of internal energy are a kinetic energy of atomic or molecular, rotational energy, vibrational energy, etc., and the bonding force and the nuclear force between the atoms or molecules making up the material. Thermodynamics focuses on understanding kinetic energy, but material mechanics focuses on bonding energy. However, it is undesirable to think of them as separate concepts. Therefore, in this study, we look for connections between two disciplines by considering the process by which internal energy develops in time. Joule's experiments on the properties of heat and work provided a basis for understanding the thermodynamic first law and energy, and he proved from a quantified relationship of work and heat that heat is a form of energy. Maxwell considered instead the velocity distribution of gas molecules, and presented a probabilistic concept. His work was used by Boltzmann to explain the distribution of energies; it can be said that Boltzmann generalized the principle of Maxwell's energy equal distribution theory. According to equipartition theorem, internal energy is defined as

($U_{int}=N{\cdot}f{\cdot}1/2{\cdot}k_B{\cdot}T$). Maxwell-Boltzmann considered the number of particles N and degrees of freedom f that can store the kinetic energy per particle, and the energy, $1/2{\cdot}k_B{\cdot}T$, that can be distributed per degree of freedom. Using these, they proposed a theoretical and mathematical way of expressing internal energy in which k_B is the Boltzmann constant $1.378 \cdot 10^{-23}$ [J/K]. The equipartition theorem can be a powerful tool in explaining atomic motion in terms of energy. However, the definition of internal energy in the equipartition theorem applies to gaseous systems, but not to solid systems, such as metals. In the solid state, particles are constrained by their mutual attractive force, so their translational and rotational motion is limited and most of them vibrate in place. In order to explain the energy of vibrating particles, it is necessary to understand the quantization in which energy is received or released as an integer multiple of the distance between nuclei (protons, neutrons) and electrons in detail. In other words, quantization means that the motion of the particle is discontinuous rather than continuous, and this means that the Newtonian mechanics, which had previously explained motion, no longer applies. Therefore, we must explain the internal energy of solid using quantum mechanics. Planck introduced the assumption that the energy E of an oscillator changes not continuously but only as an integral multiple, n, of a certain basic quantity, $h{\cdot}v$, which is proportional to the frequency. From this ($E = n{\cdot}h{\cdot}v$), he derived the average energy of the oscillator; here h is the Frank constant, $6.626{\cdot}10^{-34}$ [$J{\cdot}s$], and v is the vibration. Using Planck's idea of average oscillator energy, Einstein multiplied the average

energy by the total frequency of the solid, thus suggesting a new model to express the heat capacity of a system by a fixed oscillator and volume. Since the heat capacity is a partial differential of the internal energy with respect to the temperature, the internal energy defined in the inductive process of Einstein's heat capacity is as follows:

$$\begin{cases} U_{\text{int}} \equiv 3N\left(\frac{1}{2}hv_E + k_B T\right) \\ v_E = \frac{1}{2\pi}\sqrt{\frac{\alpha \cdot E}{m}} \end{cases} \qquad (7\text{-}15)$$

where v_E is Einstein's frequency, i.e. the natural frequency of the harmonic oscillator. If the harmonic oscillator is regarded as a pendulum of mass m attached to the ceiling, then the natural frequency can be defined from Newton's law of motion as Eq. (7-15). Eq. (7-15) is very significant for this study of metals at high-temperature because it contains all the thermodynamic, material mechanics, and quantum mechanics parameters necessary to represent internal energy. The internal energy defined by Einstein is related to a frequency dependent on the elastic modulus, which is a material property, and is also related to temperature in a given system with a fixed number of oscillators and volume. This implies that the internal energy with temperature can depend on the elastic properties of the material. Therefore, we can infer that the elastic

factors obtained in IIT (Eq. 7-14) and the internal energy, including the elastic modulus (Eq. 7-15), may be related to each other.

Fig. 7.10 shows experimental data demonstrating the validity of these inferences. As the temperature increases, the internal energy increases while the stiffness decreases. Of course, the relationship between internal energy and stiffness need not always be inverse, since stiffness is physically just the interatomic bonding force in a material, while internal energy is influenced by a variety of factors such as bonding force, temperature, frequency, mass, and number of oscillators. In other words, the internal energy is more comprehensive than stiffness. Also, consider that the internal energy may be proportional to elastic work, W_e^{IIT}, and resilience, U_R^{IIT}, of IIT, since as we have said the terms for this concept can differ according to discipline, The definition of resilience as applied to Einstein's solid model could mean the amount of energy absorbed by the interatomic or interlattice 'springs'. Thus, resilience merely excludes the temperature term from its definition, and can also be thought of as representing a part of the internal energy. However, the experimental data (resilience with temperature) here are still not sufficient, and so we give only the following correlation, based on Fig. 7.10:

$$\frac{1}{S^{IIT}} \propto U_{\text{int}} \qquad \text{where } S^{IIT}: \text{stiffness} \tag{7-16}$$

7.4.3. Helmholtz free energy and the work of IIT

Internal energy can be mathematically converted into Helmholtz free energy through the Legendre transformation in a well-known process omitted here. Instead, we consider the physical meaning of Helmholtz energy and its relationship with stiffness in IIT. To understand Helmholtz energy accurately let us imagine a certain system in contact with the reservoir. Here the reservoir can be defined as a system that continuously exchanges heat with another adjoining system; however, the heat reservoir itself has no heat loss and sustains a constant temperature infinitely. The adjoining system then can always receive heat from the reservoir, so that it can maintain a constant temperature and the internal energy needed to retain and configure the system will always save a certain amount of thermal energy (because it is constantly supplied from the reservoir). Therefore, Helmholtz free energy F can be mathematically defined as follows:

$$\Delta F \equiv \Delta U_{\text{int}} - T\Delta \text{S} \qquad \text{where S : entropy} \tag{7-17}$$

where U_{int} is internal energy, T is temperature, and S is entropy (not stiffness). In Clausius' definition of entropy, $T\Delta S$ is the change of heat, ΔQ, entering and leaving the system. Equation 7-17 shows that a certain amount of heat is less to

compose the internal energy. That is, Helmholtz energy is another name for internal energy. The concept of Helmholtz energy becomes clearer when we consider the inverse Helmholtz energy, $-\Delta F$. Here, the inverse Helmholtz energy means that the system does not receive energy from the surroundings, but rather emits energy to the surroundings. Consider the inverse reaction of Eq. (7-17): ($-\Delta F=-\Delta U+T\Delta S$). This means that when the system works on its surroundings, even if its internal energy decreases, if the reaction is a process in which system's entropy increases, the ability to work on the surroundings can be further increased. Therefore, Helmholtz energy is called a free energy in that it can express specifically what can be done by a system to its surroundings based on entropy change by heat input and output. At this time, it should be noted that the amount of work done by system is not the same as its internal energy, because the internal energy in the definition of Helmholtz energy is partly supplied by an external reservoir. Hence, the system can do the work from its internal energy, except for the amount of energy supplied by the reservoir. Only after these physical situations are clear can the concepts in a discussion of Helmholtz free energy be fully understood, such as maximum work at constant temperature, maximum work function, or useful work obtained from the system at constant temperature.

Now let's apply the concept of Helmholtz free energy to high-temperature IIT. As seen from Fig. 7.1, the high-temperature chamber has a halogen lamp that is supplied with current and always maintains a constant temperature. Thus a

halogen lamp can serve as heat storage, like a reservoir. Also, the elastic recovery of a specimen in unloading (Fig. 7.7) corresponds to the circumstances in which a system performs work on the surroundings. It can therefore be said that high-temperature IIT fulfills the definition of Helmholtz energy. Thus, the amount of energy that the specimen undergoes in elastic recovery at a certain temperature can be regarded as the amount of work which the system can do to the surroundings, that is, the amount of inverse Helmholtz energy. Therefore, the inverse Helmholtz energy can be interpreted as having the same physical meaning as the specimen resilience . The relevance of inverse Helmholtz energy to resilience is also found in the study of Wu and Wu [7.39], who described mathematically the relationship between resilience and Helmholtz energy for commercial steel (Q345, Cu, AF, HB, and mild steel):

$$-U_R = F^i - F^y = (U^i_{\text{int}} - U^y_{\text{int}}) - (T^i S^i - T^y S^y) \tag{7-18}$$

where $-U_R$ is inverse resilience, superscript i refers to internal energy (U^i_{int}), temperature (T^i), and entropy (S^i) at the beginning of the tensile test and superscript y indicates internal energy (U^y_{int}), temperature (T^y), and entropy (S^y) at the yield strength. In addition, Wu and Wu [7.39] suggested an empirical equation to obtain the resilience using Helmholtz energy, free electron gas/acoustic phonon approximations, elastic strain-electron-phonon coupling, Debye/Curie temperature, elastic modulus and yield strength. It can be said that

their results show the experimental evidence and theoretical basis for connecting the inverse resilience and Helmholtz energy in that heat transfer in a solid proceeds in the form of an acoustic wave between vibrating atoms, that the thermal vibration energy is composed of elastic waves, and that the thermal oscillating quantum energy is described as the behavior of phonon and free electrons. Eq. (7-14) shows that resilience is related to stiffness, a parameter that can be readily obtained from IIT. Thus, we can see that inverse Helmholtz energy is clearly associated with stiffness. To find the relationship between the inverse Helmholtz energy and stiffness, the entropy flow must be traced at each step of the indentation test. This is because environmental definitions of work are different: Helmholtz energy includes the work of volume expansion of the specimen by heat, and stiffness includes the work in the elastic recovery process of the specimen after unloading. One kind of work is due to heat and the other is due to force. Therefore, we must match the work regulated by the stiffness and by the Helmholtz energy to each other, and the best way to do that is to trace the flow of entropy. Entropy occurs in all changing processes, whether changed by heat or by force. Thus, using entropy change to explain what specimens undergo by heat and by force is the most plausible and efficient way to understand high-temperature IIT results, since entropy dominates all system changes.

7.4.4. Entropy flow in IIT process

High-temperature IIT can be divided into the three systems shown in Fig. 7.11. System 1, a halogen lamp, acts like the reservoir mentioned above. System 2 is the IIT device and system 3 is the specimen. There is a temperature difference between system 1 and system 2, so that they exchange heat energy until thermal equilibrium is reached. At this moment, it is assumed that system 1 has no heat loss and always maintains a certain constant temperature and a constant volume. System 2 can apply or remove the load on system 3. After removal of the load by system 2, the system 3 exchanges volume with the surroundings (because of the pressure difference) until the mechanical equilibrium state is reached. The volume of system 2 remains unchanged and always maintains a constant volume: that is, the indentation shaft and indenter are assumed to be rigid. Surely, energy can also be exchanged between system 1 and system 2. Because system 1 supplies infinite thermal energy to system 2, the indentation device in System 2 is also heated until a thermal equilibrium condition is reached. The effect of heat on system 2 is seen as the compliance. In general, the compliance depends on the geometrical configuration and on the inverse of the elastic modulus of system 2. The geometric configuration does not change, but the elastic modulus can decrease with increasing temperature, so compliance increases with increasing temperature.

The temperature effect of compliance was calibrated through a method introduced in [7.6]. Therefore, this study focuses on system 3 (specimen), which is affected by heat and load. Here it is assumed that there is no change in the number of particles in each system, and there is no exchange of particles between each system. It is also assumed that systems 1, 2, and 3 are isolated and energy can be exchanged among each of the systems, but that the total internal energy is conserved. It is also assumed that the material behavior at the moment of elastic recovery after unloading follows the Einstein solid model [7.40]. In order to track the change of entropy of system 3 during high-temperature indentation, a common technique is to use the internal energy change and volume change relation of system 3, since system 3 is exchanging not only heat but also mechanical pressure. Therefore, it is necessary to express the part changed by heat as an internal energy change, and the part changed by pressure as a volume change.

Fig. 7.12 describes the indentation response of system 3 at given high-temperature conditions as a change in volume and internal energy. System 3 can be changed from the equilibrium state A (V_A, U_A) to the equilibrium state B (V_B, U_B) while system 3 exchanged energy with systems 1 and 2. It is very difficult directly to interpret the change of state from A to B, and we will look at it step by step. System 3 in state A (V_A, U_A) achieves thermal equilibrium while exchanging thermal energy with system 1. Therefore, step 1 in Fig. 7.12 means that system 3 is heated and reaches the temperature of system 1. And since step

1 is a constant-volume process, there is no change in work, W, so the value of is zero and only heat, Q, operates. Therefore, in a quasistatic situation, we can apply the first and second laws of thermodynamic to step 1: $dQ \approx dU \approx TdS$. That is, the heat flow is equal to the change in internal energy and can be expressed as the product of the change in temperature and entropy. Therefore, process step 1 of system 3 in Fig. 7.12 can be written as

Step 1: $TdS_{A\to B} \approx dU_{A\to B}$ (when Q flows from system 1 to system 3)(7-19)

In this step, of course, the reaction that transfers heat from system 3 to system 1 occurs. However, as mentioned earlier, system 1 is like a heat reservoir, so regardless of whether heat was received or discharged, system 1 is always constant. Therefore, it is meaningless to consider the heat received from system 3.

Step 2: $TdS_{A\to B} \approx dU_{A\to B} + (PdV)_{thermal\ expansion}$ (7-20)

In step 2 of Fig. 7.12, system 3 receives heat energy, which means that the elastic modulus decreases in Einstein's frequency (Eq. 7-15), so that the attraction between the atoms weakens and the volume of system 3 expands. At this time, the volume is still equal to the ambient pressure; volume is exchanged with the surroundings, so that a mechanical equilibrium state is reached.

Therefore, the step 2 can be written as Eq. (7-20) by adding a term for work of volume expansion into Eq. (7-19), since the internal energy is fixed but the volume increases.

Step 3:

$$TdS_{A\to B} \approx dU_{A\to B} + (PdV)_{thermal\ expansion} - (PdV)_{loading,indentation} \quad (7\text{-}21)$$

Step 3 means that a load is applied to system 3 by system 2, so the volume of system 3 is reduced. At this time, the volume reduced depends on the indentation depth and the indenter geometry. Since Vickers indenters were used here, the amount of the reduced volume was calculated through mensuration by parts, $\lim_{n\to\infty} V_n = 1/3 \cdot a^2 \cdot h_{max}$, where V_n is the volume (dependent on indenter shape), a is the cross-sectional area of the impressed mark, and h_{max} is the maximum indentation depth. During step 3, force energy is transferred from system 2 to system 3. This force energy acts on the area and is consumed so as to cause plastic deformation over most of system 3; the rest of this energy is consumed as elastic deformation in interatomic and interlattice space. Here the elastic energy is consumed but does not disappear, and can accumulate inside the material for elastic recovery. Therefore, the process up to step 3 can be written as Eq. (7-21), considering the volume reduction by loading:

Step 4:

$$TdS_{A\to B} = dU_{A\to B} + (PdV)_{thermal\ expansion} - (PdV)_{loading,indentation} + (PdV)_{unloading,elastic\ recovery} \quad (7\text{-}22)$$

Step 4 in Fig. 7.12 is the final step in which system 3 reaches from state *A* to state *B*. During step 4, system 3 undergoes unloading, and the internal energy is released to the outside, again reducing the distance between atoms and lattices. During this elastic recovery process, The material behavior follows Einstein's solid model and the volume increases somewhat, so that step 4 can be written as Eq. (7-22). Eq. (7-22) describes the overall change that the specimen undergoes when performing high-temperature IIT at a constant temperature. If we divide both sides of Eq. (7-22) by temperature *(T)* and abbreviate the subscripts, we have:

$$dS_{tot.} = \frac{1}{T} dU_{tot.} + \left(\frac{P}{T} dV\right)_{\text{t.e.}} - \left(\frac{P}{T} dV\right)_{\text{l.}} + \left(\frac{P}{T} dV\right)_{\text{unl.}} \quad (7\text{-}23)$$

where dS_{tot} is the total entropy change in system 3 during the transition from state *A* to state *B*. dU_{tot} also shows the total internal energy change while changing from state *A* to state *B*; the subscripts *t.e* indicates thermal expansion, *l* is the indentation loading, and *unl* is indentation unloading. In general, when two systems with temperature differences are mixed, the mixed system must

move toward the maximum probability of the multiplicity (Ω): that is, the mixed system moves in a direction where the entropy increases by Boltzmann's entropy definition [$S = k_B ln\Omega$], and at the point of maximum multiplicity, the derivative of entropy and internal energy becomes zero (this maximum is called thermal equilibrium). Since the internal energy is a function of temperature, the relationship between entropy and internal energy can also be expressed as temperature. In particular, in the relation between entropy and internal energy, if the temperature has a large value, the derivative is small; if the temperature is small, the derivative is large. Therefore, we have $1/T = (\partial S/\partial U)$, (where S is entropy) at a certain number of particles and a certain volume. A similar concept holds for systems that have volume differences. The volume difference is due to the pressure difference, so the phenomenon occurs when two systems equalize the pressure while exchanging volumes. In other words, the system moves in the direction of entropy increase. Therefore, for a constant number of particles and constant internal energy, pressure can be expressed as the derivative of entropy and volume, $P = T(\partial S/\partial V)$. Therefore, we can rewrite each term in Eq. (7-23) using entropy as follows:

$$dS_{tot} = \left(\frac{\partial S_1}{\partial U_{tot}}\right)_{V,N} dU_{tot} + \left(\frac{\partial S_2}{\partial V_{t.e.}}\right)_{U,N} dV_{t.e.} - \left(\frac{\partial S_3}{\partial V_l}\right)_{U,N} dV_l + \left(\frac{\partial S_4}{\partial V_{unl}}\right)_{U,N} dV_{unl} \qquad (7\text{-}24)$$

We can rearrange this equation by moving the last term to the left side:

$$\left(\frac{\partial S_4}{\partial V_{unl}}\right)_{U,N} dV_{unl} = dS_{tot} - \left(\frac{\partial S_1}{\partial U_{tot}}\right)_{V,N} dU_{tot} - \left(\frac{\partial S_2}{\partial V_{t.e.}}\right)_{U,N} dV_{t.e.} + \left(\frac{\partial S_3}{\partial V_l}\right)_{U,N} dV_l \qquad (7\text{-}25)$$

The left side of Eq. (7-25) represents the energy (Fig. 7.7) required to recover the elasticity of the impression after unloading in the form of "entropy", which is to the final entropy in the high-temperature IIT process, the entropy of state B in Figure 7.12, and the entropy of the specimen after unloading. Therefore, this energy cannot be physically matched to the work that the specimen undergoes in elastic recovery after unloading at high- temperature until the entropy change defined in Eq. 7-25 is applied to Helmholtz free energy. It can be inferred that the inverse Helmholtz energy with dS_4 can be inversely proportional to the resilience by Eq. (7-18), and can be proportional to the stiffness by Eq. (7-14):

$$dS_4 \propto -dF_4 \propto dU_R^{IIT} \propto dS^{IIT} \qquad (7\text{-}26)$$

where dS_4 is the entropy change defined from Eq. (7-25), $-dF_4$ is the inverse Helmholtz energy change taking S_4 into account, dU_R^{IIT} is the resilience change in IIT, and dS^{IIT} is the stiffness change in IIT.

Fig. 7.13, the experimental results describing the relationship in Eq. (7-26), shows that the indentation stiffness, dS^{IIT}, is proportional to the inverse Helmholtz free energy, $-dF_4$. The fitting equation approximating Fig. 7.13 by regression analysis is:

$$S^{IIT} = 0.0035 \cdot (-F_4) + 5.06268 \qquad \text{where } S^{IIT}: \text{stiffness} \tag{7-27}$$

Eq. (7-26) and (7-27) and Fig. 7.13 have many implications. Indentation stiffness is a mechanical factor and Helmholtz energy is a thermodynamic factor, but these two factors are interrelated. In material mechanics, the Helmholtz energy emerged in describing the movement of thermally activated dislocations. At high- temperatures, dislocation movement can be divided into cases in which there are no thermal waves and cases in which there are thermal waves. The mechanism of those dislocation motions was detailed in Section 3. Thus, to summarize briefly, dislocation motion can be expressed as a function of activation energy, shear stress (called effective stress), Boltzmann's constant and temperature, $\dot{\varepsilon} = \dot{\varepsilon}_0 exp\{-\Delta G(\sigma_{eff})/kT\}$. What is important here is the activation energy, which can be decomposed into two terms: the Helmholtz energy and the product of the activation volume (the obstacle's width involved in the plastic flow, dislocation segment length between obstacles) and the effective stress, $\Delta G(\sigma_{eff}) = \Delta F - V \cdot \sigma_{eff}$. That is, the activation energy is the

energy supplied in the form of heat, except for the stresses required for dislocation motion [41]. Since Helmholtz energy is involved in the movement of dislocations, of course, it can also be related to the material's mechanical properties [7.42, 7.43]. Therefore, the result in Fig. 7.13 that Helmholtz free energy is associated with stiffness in IIT not only can be explained by dislocation theory but also leads to a new discovery.

The more important idea is to use Eq. (7-27). Thinking Eq. (7-27) in the opposite, if only Helmholtz energy can be obtained, the material stiffness can be determined; since the stiffness is the slope of unloading curve, we may be able to infer the high-temperature unloading curve. That is, it implies that it is possible to deduce the high-temperature *L-h* curve indirectly without actual high-temperature indentation. A method for predicting the mechanical behavior of materials at high-temperatures has already been established in tensile testing. The constitutive equation of Johnson and Cook [44] is a representative example, $\sigma = (A + B\varepsilon^n)(1 + Cln\dot{\varepsilon}/\dot{\varepsilon}_0)\{1 - (T - T_r/T - T_m)^D\}$. In metallic materials, temperature as well as strain and strain rate are important factors affecting deformation behavior. Johnson and Cook proposed an experimental model considering effects of strain hardening, strain-rate hardening, and thermal softening by Hopkinson bar testing for oxygen-free high-conductivity copper (OFHC) and 4340 steel, among other materials, and many studies have used this model to predict high-temperature stress-strain curves [7.41-7.46]. The method for approximating the *L-h* curve proposed here does not reflect the effects of

strain hardening, strain- rate hardening, and thermal softening like the Johnson-Cook model. Future work may need to reflect such a deformation behavior of materials in its predicting model. However, the methodology for predicting the *L-h* curve at high-temperatures using Helmholtz energy is new. More details are introduced in the next section.

7.5. Application

7.5.1. The need of predicting indentation load-depth curve at high-temperature

Here we propose a method of predicting the high-temperature indentation load-depth curve using the stiffness-Helmholtz energy relation of Eq. (7-27). Until now, no studies have been reported on predicting the *L-h* curve in IIT research, and this may be the first attempt. The reasons why it is useful to predict the high-temperature *L-h* curve are clear.

The first reason is in designing high-temperature structures. Mechanical properties such as elastic modulus, yield strength, tensile strength and fracture characteristics generally deteriorate at high-temperatures. Therefore, designers must be aware of the actual operating temperature of the structures, and they must reflect the degraded mechanical properties in their design. Currently, designers of high-temperature facilities have either relied on information from actual high-temperature tensile tests or by using a constitutive model such as the Johnson-Cook model [7.44]. Both methods have weaknesses. Using the tensile curve means that material's properties are taken as an average, while they are likely in fact to differ locally. If the mechanical characteristics of a locally vulnerable area are known from IIT, a more complete design can be achieved.

The second is due to microstructural differences. Metal microstructures have different phases depending on temperature. The microstructure at the actual operating temperature may differ significantly from the microstructure observed at room-temperature, and this difference can lead to a difference in mechanical characteristics. Therefore, it can be dangerous to estimate the stability of high-temperature facilities from microstructural information at room-temperature. Indeed, Wheeler et al. [7.51] have pointed out that the observed room-temperature microstructure after high-temperature nanoindentation testing can be significantly different from the microstructure at the actual test temperature. Fischer-Cripps says [7.52]: "An understanding of the mechanical behavior for many structural components can best be obtained from tests that are performed at a temperature corresponding to the in-service temperature of the sample". However, it is not possible to obtain data directly by attaching an IIT device to a facility at the actual operating temperature. Even above 373 K, such facilities can be very dangerous to approach. Also, even if the equipment is attached at room-temperature and then raised to high-temperatures, it is almost impossible to obtain stable experimental data due to factors causing measurement error (e.g., measurement sensor malfunction due to vibration and heat transfer). Therefore, a good alternative plan is to consider the effect of temperature and use room-temperature IIT results.

The third is for nondestructive lifetime assessment. The conventional mechanical test for lifetime evaluation is the creep test, which applies a constant

load to the material to measure the displacement over time. Although this method is widely used, damage to facilities is inevitable in obtaining a creep-testing sample. An alternative to this method is to use the hardness [7.53], which has the advantage of causing minimal damage to the facility. However, this also can only be done at room-temperature, and the assumption that a material's reaction to an applied load at high-temperature would be the same as that at room-temperature is implausible. In addition, since a portable microscope is used to measure the impressed mark on the actual structure, measurement error may occur. Therefore, IIT testing that measures the indentation depth by mechanical instrumentation instead of measuring the area can more accurately reflect the reaction of the material, and predicting the indentation depth at high-temperatures would more closely match the operating conditions.

7.5.2. Specimen, assumptions and conditions for prediction

The specimen used to predict the high-temperature *L-h* curve is S45C material. The S45C steel has BCC type of crystal structure, like other specimens used here, but it was not used in Figs. 7.10 and 7.13 above. It was selected only to show the method and accuracy of curve prediction. In order to predict the high-temperature *L-h* curve, some assumptions are made. While the actual loading and unloading curves are curved, they are taken as straight lines for the sake of simplicity. And we set the condition that the maximum indentation depth is fixed at 80 μm. In addition, the stiffness and Helmholtz energy relations of Eq. (7-27) are used.

Fig. 7.14 shows the difference between the constant maximum indentation depth, h_{max}, and the final indentation depth, h_f, according to temperature, and Eq. (7-28) shows the results obtained by fitting Fig. 7.14. Also, the S45C sample is omitted from Fig. 7.14. The reason for the introduction of Fig. 7.14 and Eq. (7-28) is to predict the unloading curve. In IIT theory, the initial slope of the unloading curve means stiffness. At this time, the stiffness value can be obtained by using the Helmholtz energy relation, Eq. (7-27). Here, since stiffness merely means slope, the maximum indentation load L_{max} corresponding to the height and the difference between the maximum indentation depth and final indentation depth corresponding to the base must be determined quantitatively. L_{max} with temperature can be predicted by the definition of stiffness, but no good

way to determine h_f has been found. Therefore, the relation in Eq. (7-28) was required experimentally.

$$\left(h_{\max} - h_f\right) = 0.0068 \cdot (T) + 10.45391 \qquad (7\text{-}28)$$

The final assumption is that the *L-h* curves of the specimens used here have the same or very similar behavior at 273 K and 373 K. This assumption is established empirically by high-temperature indentation experiments on the specimens used here and can be viewed as somewhat unreasonable. However, it is necessary in order to determine the correct L_{max} and will be discussed in Section 5.4 below.

7.5.3. Overall process for predicting *L-h* curve.

Fig. 7.15 shows the overall process for predicting the *L-h* curve at high-temperature. For this prediction, it is certainly necessary to know the temperature, T, of the target material and the specific heat, C_p or C_v, at that temperature in advance. In a real structure, the operating temperature is set at design time or can be measured directly. For the specific heat one can take values from the literature or use DSC testing. When multiplying the temperature and the specific heat by the specimen mass, the heat, Q, flowing in the specimen is calculated, $\delta Q = c \cdot m \cdot d\mathrm{T}$. If there is information about the heat, the internal energy, U_{int}, and entropy-four, S_4, can be calculated using the first law of thermodynamics and Clausius' second law. Here U_{int} and S_4 are derived by analyzing the indentation process thermodynamically as shown in Fig. 7.11, Fig. 7.12, and Eq. (7-25). If the internal energy and entropy-four are known, they can be converted into the inverse Helmholtz energy by Eq. (7-17). If Eq. (7-27) is used, the inverse Helmholtz energy can be quantitatively converted to the stiffness value. Now, assuming that the loading and the unloading curves are simple straight lines, the stiffness can be divided into L_{max} and h_{max}-h_f by the definition of the slope, so that the approximate unloading curve can be drawn on the coordinate plane. Lastly, if Eq. (7-28) is used, the information about stiffness is already known and information on indentation depth according to temperature is also known, so that the position of L_{max} can be determined. Therefore, we can

obtain the linearly approximated loading curve by drawing a straight line from the origin to L_{max}.

7.5.4. Five stages for prediction and calibration

- Stage 1: Determination of h_f

Consider a Cartesian coordinate system with origin at (0, 0); the x-axis is depth and the y-axis is load. In this stage, the precondition that the maximum indentation depth is constant, (h_{max}=80 μm), is used, and the temperature must be known in advance. If a certain temperature has been determined, the final indentation depth, h_f, can be determined using equation (7-28). Then a point at (0,0) on the Cartesian coordinates can move to (h-h_f).

- Stage 2: Drawing the unloading curve

In this stage we find the slope of a straight line intersecting the point moved to (h-h_f). If a certain temperature is set and the heat capacity of the specimen is known at that temperature, then the inverse Helmholtz energy value, -F_4, can be determined from the flow chart in Fig. 7.15 and Eqs. (7-17), (7-25). Here the inverse Helmholtz energy contains entropy-four, S_4, which is derived by analyzing the indentation test process, of course, under the thermodynamic first and second laws. Using Eq. (7-27), the inverse Helmholtz energy can be converted to a stiffness value, S^{IIT}. Thus, a straight line with a slope can be drawn from the point at the position (h-h_f). This straight line approximates the unloading curve.

- Stage 3: Determination of L_{max}

Quantitative values of stiffness from Eq. (7-27) and (h_{max}-h_f) from Eq. (7-28) at a given temperature were obtained in stages 1 and 2. Since we already know (h_{max}-h_f), and the stiffness, we can determine L_{max} by using mathematical definition of slope, $S^{IIT} = L_{max}/(h_{max} - h_f)$.

- Stage 4: Drawing the loading curve

In this stage, the slope of the loading curve is determined. Under the preceding conditions, h_{max} is already set as 80 μm and L_{max} was determined in stage 3. Therefore, the distance from the origin (*0,0*) to (L_{max}, h_{max}) corresponds to the slope of the loading curve. Therefore, if the ratio of L_{max} over h_{max} is taken as the slope and a straight line corresponding to the slope determined at the origin is drawn, the loading curve can be approximated.

- Stage 5. Calibration of L_{max}

Fig. 7.16 shows the *L-h* curve at 375 K predicted in a straight line in stages 1, 2, 3 and 4 using the flow chart in Fig. 7.15. The target specimen is S45C. The heavy black curve is the *L-h* curve measured at 375 K and the thin red line is the predicted *L-h* curve. Fig. 7.16 shows a noticeable difference in L_{max}, but it can be seen that stiffness and h_f are fairly similar. The actual and predicted *L-h* curves are inconsistent for two reasons. First, the flow chart in Fig. 7.15 shows that only the elastic properties of the specimen are considered. The IIT causes

elastic-plastic deformation of the specimen, but it also creates inconsistency with the actual *L-h* curve because only the elasticity is considered in the proposed prediction method. The assumption that the loading and unloading curves are straight lines may also cause a problem. When the load is transferred to the specimen through the indenter, a hydrostatic core is formed at the bottom of the indenter. As the load increases, the size of the core gradually expands, forming a plastic zone that causes plastic deformation around the core and is constrained by the surrounding elastic zone. Therefore, the deformation at the bottom of the indentation causes a very small elastic deformation at the moment of contact, soon transitioning to elastoplasticity and complete plasticity [7.15, 7.54, 7.55]. The IIT loading and unloading curves result from those complex deformation mechanisms, which our simple linear prediction method does not fully reflect. However, in the process of developing the prediction method, we overlooked one issue: that the *L-h* curve can be obtained at room-temperature. It is believed that only the *L-h* curve at 273 K is reliable. Not only can the *L-h* curve at room-temperature be obtained by attaching the equipment to actual stationary facilities, but this curve can also give information reflecting the elastic-plastic deformation of the specimen. Therefore, to calibrate the predicted *L-h* curves in Fig. 7.16, we need only to use information that can be obtained experimentally and is reliable at room-temperature. Therefore, the maximum indentation load, ($L_{max}^{measured\_273K}$), at room-temperature is used in this study. Because maximum indentation depth was always set to be constant, it was

thought reasonable to consider load as a variable. In order to reduce the load error in Fig. 7.16, therefore, we propose calibration by the ratio of the maximum indentation load. Here, one important assumption is added: that the maximum indentation load at 273 K and the at 373 K are the same or differ very little (within ~1 kgf). This assumption is probably not generally acceptable, since a 100 K temperature difference can cause a very large load difference depending on the experimental material. However, for the specimens used in this study, it was confirmed empirically that the 100 K difference produced almost no difference in indentation maximum load. If the assumption is established that the maximum load at 273 K and the maximum load at 373 K are the same or similar, then the measured maximum load at 273 K is equal to or very similar to that predicted at 373 K. Using the ratio of the actually measured maximum load at 273 K to the virtually predicted maximum load at 373 K has the helpful effect of reducing the maximum load error.

$$\frac{L_{\max}^{measured\_273K}}{L_{\max}^{predicted\_373K}} \tag{7-29}$$

In this study, we created the IIT maximum load ratio in the form shown in Eq. (7-29) as the calibration coefficient. The constant value derived from Eq. (7-29), as the correction factor, was multiplied by the IIT maximum load predicted at 375 K, 475 K, 575 K, 675 K and 775 K. As a result, the maximum load error is

reduced. Figs. 7.17 and 7.18 show the actual *L-h* curves measured at 575 K and 675 K, respectively (bold black lines) and the calibrated *L-h* curve predicted at room-temperature (thin red lines). The maximum indentation load, final indentation depth, and stiffness show significant predictive accuracy. Table 3 compares the quantities obtained from the measured *L-h* curves with those from the predicted *L-h* curves.

Table 7.3 shows the difference between variables obtained from measured *L-h* and predicted *L-h* curves at each temperature. It can be seen that most variables match well (within 15% error); the error at 373.15 K is small, but the higher the temperature, the larger the error. In particular, the error in stiffness is –29.32% at 773.15 K, probably because of inaccuracy in Eq. (7-27). Stiffness can be obtained from the inverse Helmholtz energy. However, the data distribution in Fig. 7.13 is not considered to be expressed perfectly in the form of Eq. (7-27). Although there are several limitations, conditions and assumptions on the work here that can be difficult to justify, the suggested method of predicting the high-temperature indentation curves presents another possibility in their application. In the past, various kinds of mechanical properties were obtained from a single indentation test, and this has been recognized as a benefit of IIT. However, this study suggests that physical properties at high-temperatures can be also obtained. Therefore, continuing to develop this study should let us will produce *L-h* curves with greater accuracy and predictability.

7.6. Summary

We have investigated applying material mechanics and thermodynamics to analyze the elastic recovery of materials after unloading in the indentation test process using high-temperature IIT equipment. In addition, we predicted a high-temperature indentation load-depth curve by using the relation between stiffness and Helmholtz free energy. The steps for predicting load-depth curve have led to the following conclusions:

The elastic recovery of the specimen after unloading can be interpreted as due to the fact that when the Einstein solid model is applied, the atoms displaced by the influence of the external force travel to their original position. In this process, the work done by system on the surroundings can be defined and the amount of work from the area under the unloading curve can be quantified. The work of IIT can be expressed as an indentation parameter, and it was confirmed that this work was in proportion to the resilience as defined in the tensile test.

Since the resilience means the elastic energy of the material, it can be confirmed that it is related to the stiffness obtained from the slope of the indentation unloading curve. In a solid with constant volume and number of particles, we consider that the internal energy must be comprehensively understood as the frequency of atoms, the temperature, and the bonding force between atoms, and is influenced by the elasticity of the material. Therefore, it was confirmed experimentally that there is a correlation between stiffness and internal energy.

The energy inside the material (excluding the product of temperature and entropy change) is called Helmholtz free energy. Helmholtz free energy is a function of entropy at a certain temperature, so we proposed that it can be related to the recovery work after unloading. The entropy flow was traced by dividing the indentation process by heat, load, and load removal, and it was confirmed that the stiffness in IIT and the inverse Helmholtz free energy are proportional to each other.

The relationship between the stiffness and the inverse Helmholtz free energy and the dependence of the indentation depth on the temperature are used to predict the indentation load-depth curve at high-temperatures. In this process, the indentation curve is assumed to be a straight line, and a calibration coefficient is proposed to increase the accuracy of the predicted curve.

This study focuses on the mechanical phenomenon of elastic recovery of the specimen after unloading in IIT in a high-temperature environment. We propose a new method to predict the load-depth curve at high- temperatures if the room-temperature indentation curve and the specific heat of the specimen are known. A new way to interpret the indentation load-depth curves is presented by analyzing the high-temperature IIT procedure in terms of entropy flow. However, that the specimens used here are limited to general tool steels, and that somewhat immoderate assumptions were used to predict the high-temperature curve, remains regrets.

In exploring this problem, we received from Doosan Heavy Industries & Construction and Korea Electric Power Corporation in Korea eight alloys (JIS STBA 23, ASME SA-213/335 Grade 92, KA-SUS410J3 TPTB, JIS SUS316 HB, JIS SUS347H TB, KA-SUS310J1 TB, JIS NCF 600, JIS NCF 750-B) that are used in high-temperature facilities such as boilers, turbine rotors, tubes and pipes. We continue research on these alloys in order to improve the prediction accuracy of the theory presented here. In addition, as in the Cook model, the effect of strain, strain rate and temperature should be also taken into account.

Table.7.1. Mechanical properties

Specimen	E (GPa)	YS (MPa)	UTS (MPa)	*n*	Hv (kgf/μm^2)
SKS3	210	435	756	0.22	195
SKH51	223	295	784	0.26	222
SKD11	217	343	808	0.26	230
SUJ2	217	404	822	0.24	199
SKD61	214	371	781	0.24	201
SK3	207	315	707	0.26	165
S45C	212	363	774	0.26	171

Table 7.2. Heat capacities. C_p: [J/K]

	SKS3	SKH51	SKD11	SUJ2	SKD61	SK3
323 K	11.06	9.82	9.30	9.92	8.76	8.74
373 K	11.94	21.48	10.89	10.97	9.65	9.90
423 K	12.75	22.85	11.67	11.66	10.34	10.79
473 K	13.46	23.98	12.38	11.87	10.87	11.41
523 K	13.95	24.86	12.91	11.42	11.30	11.91
573 K	14.18	25.43	13.37	9.53	11.64	12.19
623 K	14.69	25.87	13.72	10.19	11.92	12.55
673 K	14.90	26.26	14.13	12.77	12.15	13.04
723 K	15.29	26.41	14.40	13.71	12.35	13.45
773 K	15.71	26.29	14.64	14.08	12.55	13.73

Table 7.3. Comparison of measured and predicted IIT variables.

		Measured Curve	Predicted Curve	Error (%)
373.15 K	L_{max}	27.23	27.23	0
	h_f	68.3	67.01	1.89
	Stiffness	2.97	3.05	-2.67
		Measured Curve	Predicted Curve	Error (%)
473.15 K	L_{max}	26.79	26.27	1.98
	h_f	67.8	66.33	2.17
	Stiffness	3.04	2.79	7.96
		Measured Curve	Predicted Curve	Error (%)
573.15 K	L_{max}	25.86	26.60	-2.88
	h_f	66.8	65.64	1.74
	Stiffness	2.74	2.69	1.38
		Measured Curve	Predicted Curve	Error (%)
673.15 K	L_{max}	27.58	27.20	1.38
	h_f	63.9	64.97	-1.67
	Stiffness	2.30	2.64	-14.39
		Measured Curve	Predicted Curve	Error (%)
773.15 K	L_{max}	26.17	28.22	-7.82
	h_f	63.6	64.29	-1.08
	Stiffness	2.02	2.62	-29.32

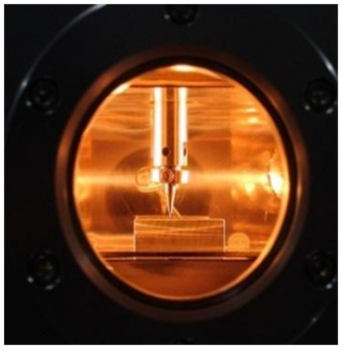

Fig. 7.1. Indenter, sample, and halogen lamp inside chamber.

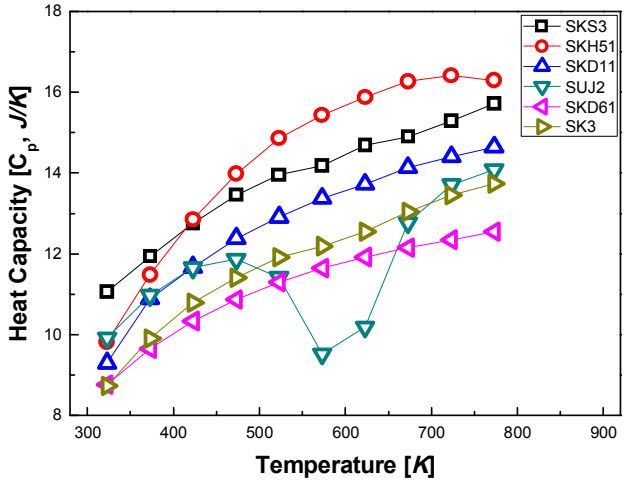

Fig. 7.2. Thermal capacity with increasing temperature

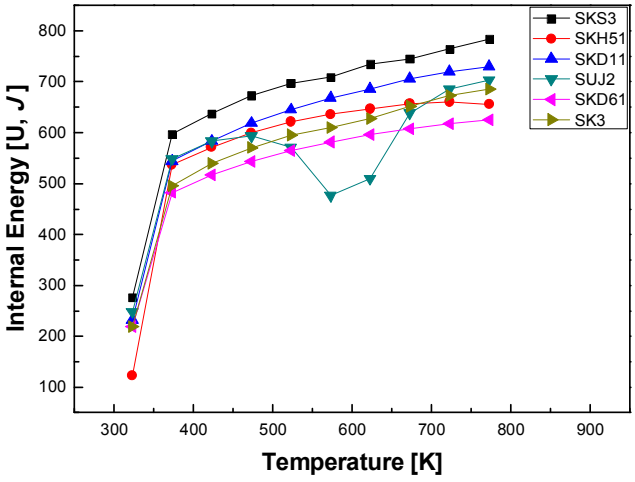

Fig. 7.3. Internal energy with increasing temperature

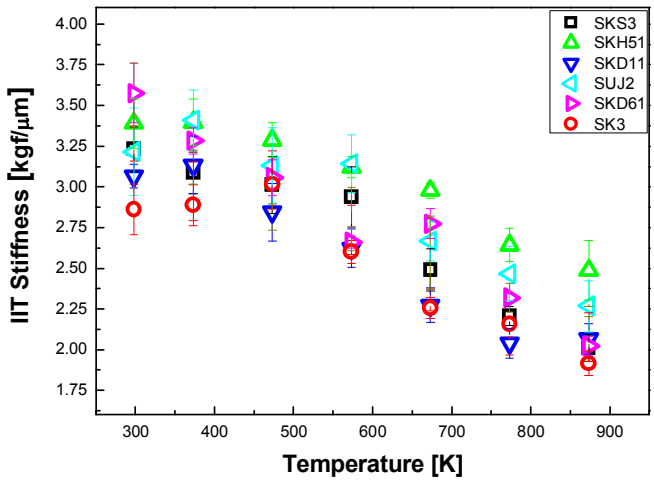

Fig. 7.4. Stiffness with increasing temperature (IIT).

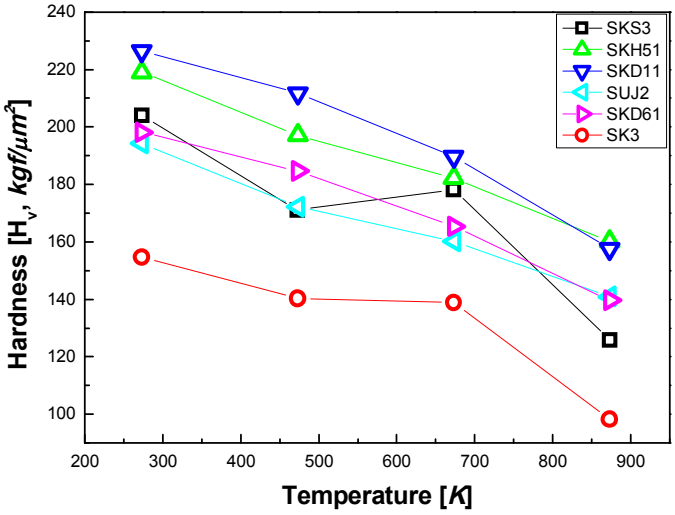

Fig. 7.5. Vickers hardness with increasing temperature.

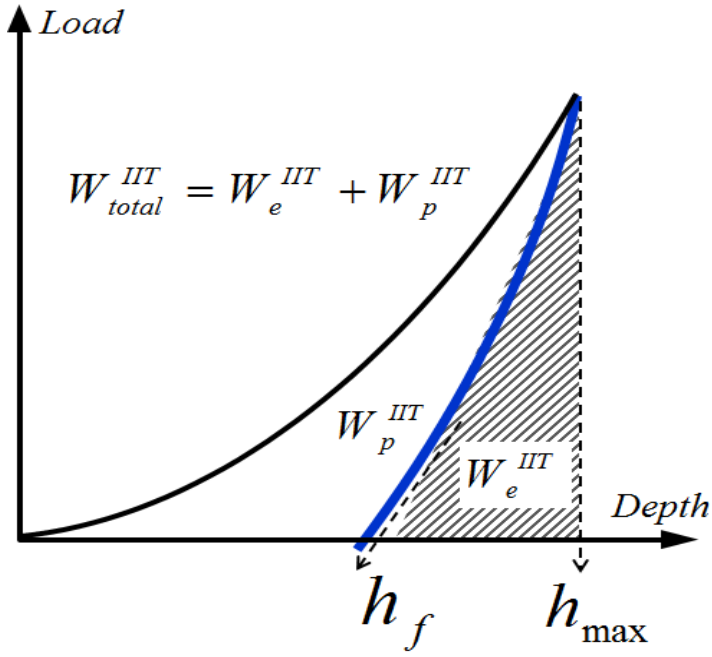

Fig. 7.6. Definition of indentation energy

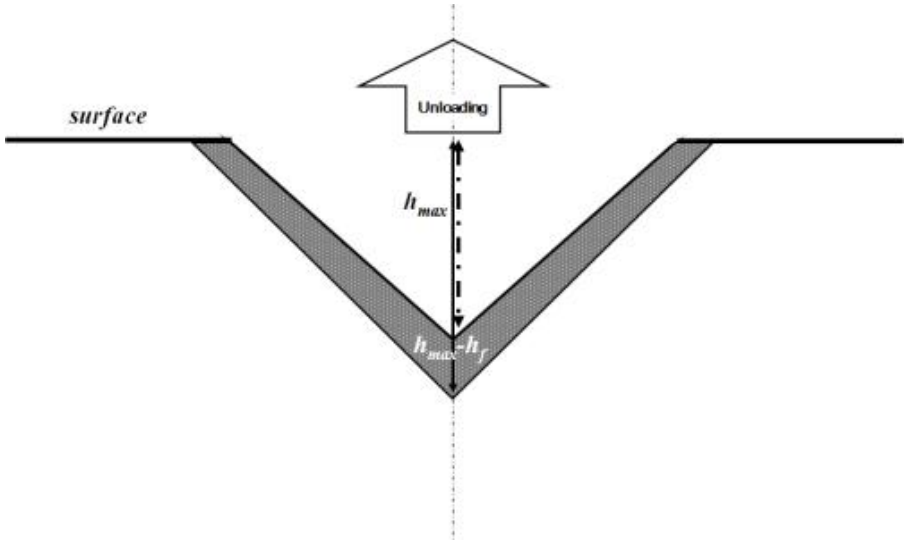

Fig. 7.7. Elastic recovery of indent mark in IIT

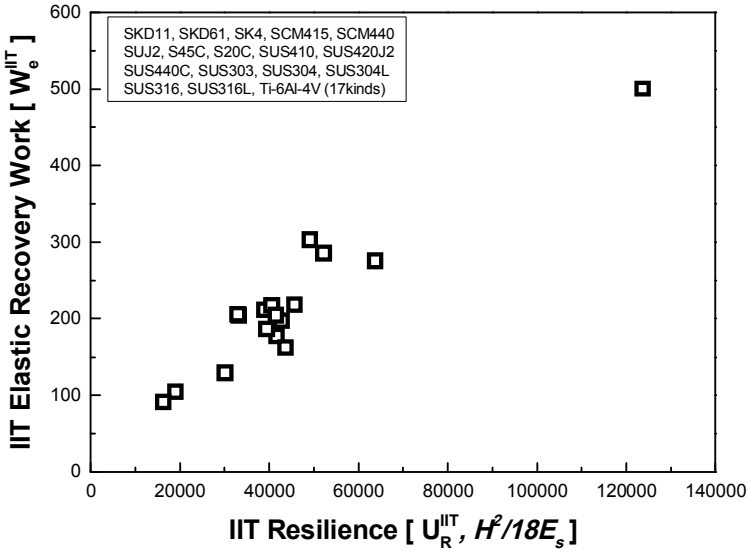

Fig. 7.8. Relation between elastic recovery work and resilience in IIT

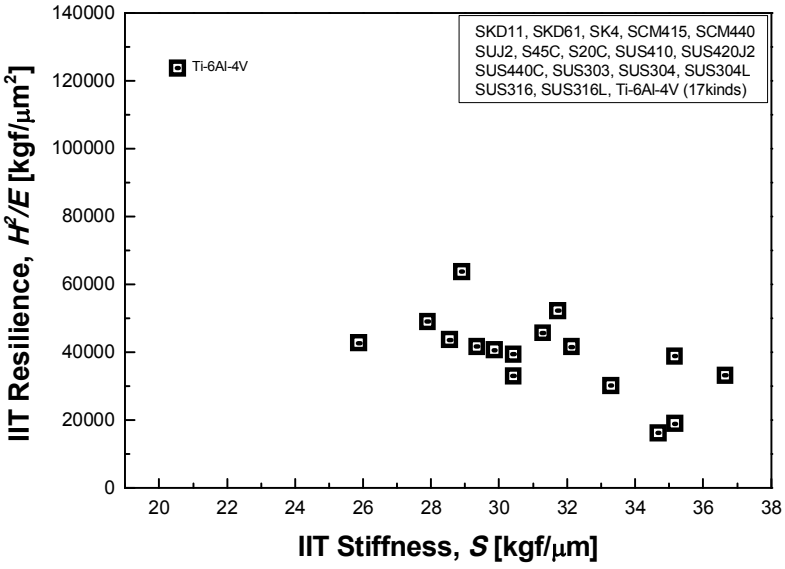

Fig. 7.9. Relationship between stiffness and resilience in IIT

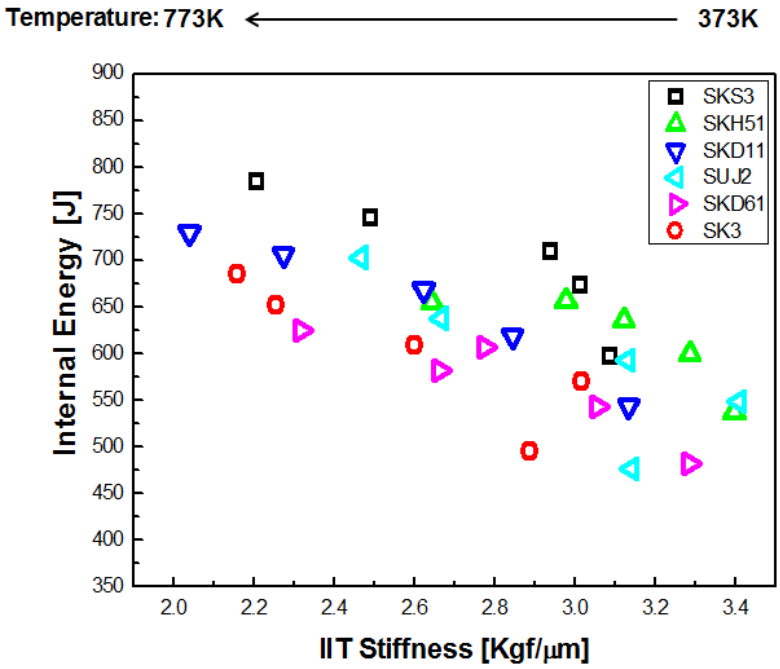

Fig. 7.10. The relationship of internal energy and stiffness

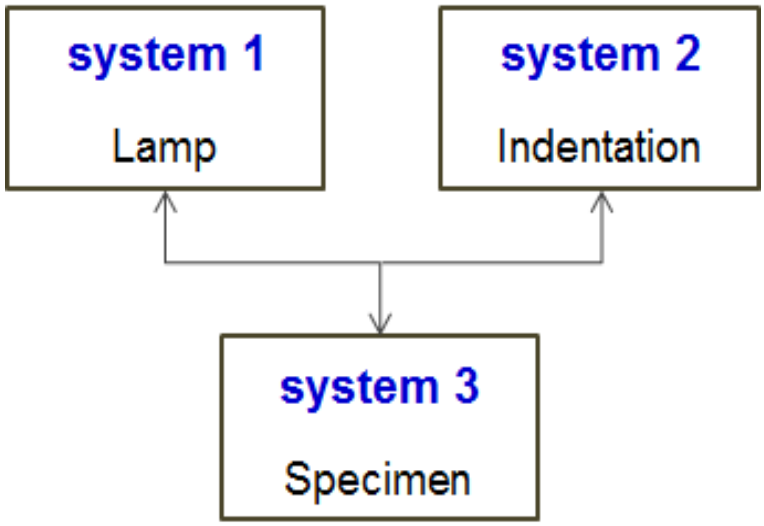

Fig. 7.11. High-temperature IIT systems.

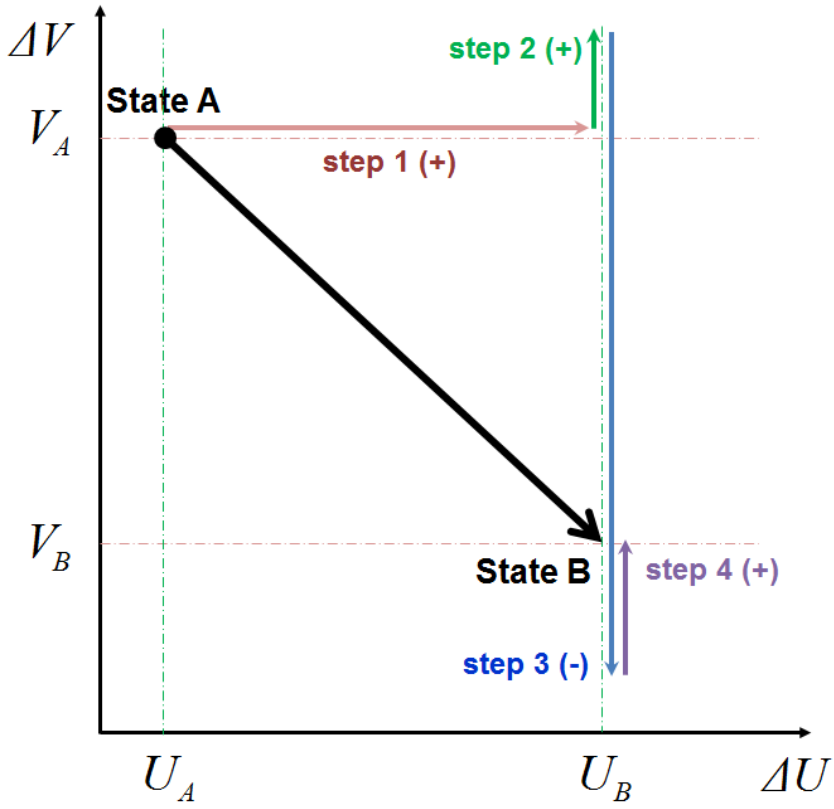

Fig. 7.12. The step process in high-temperature IIT

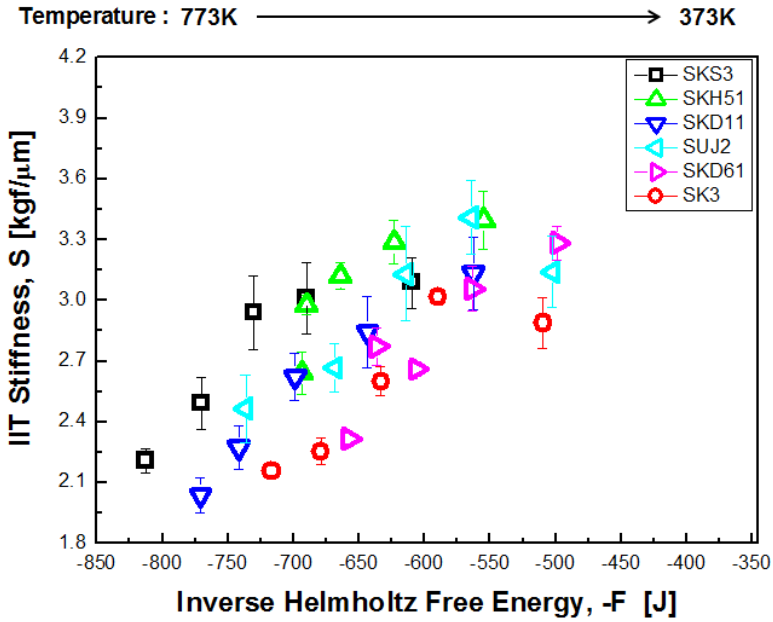

Fig. 7.13. The relationship of stiffness and inverse Helmholtz energy in IIT

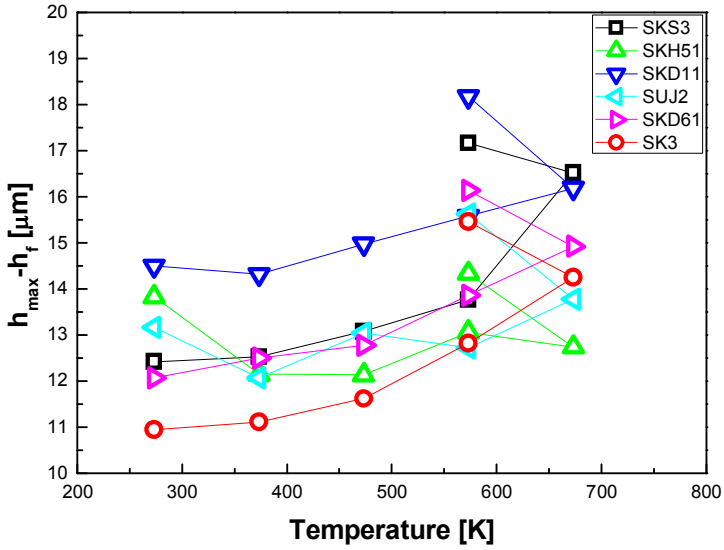

Fig. 7.14. The relationship between indentation depth and temperature.

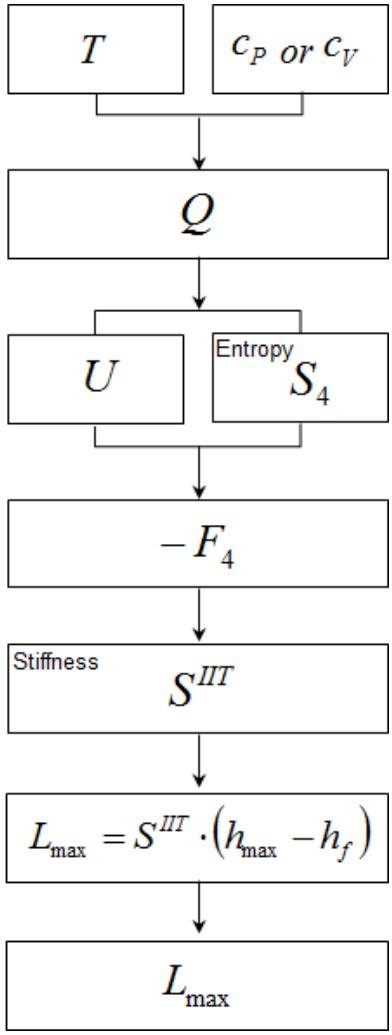

Fig. 7.15. Flow chart for prediction

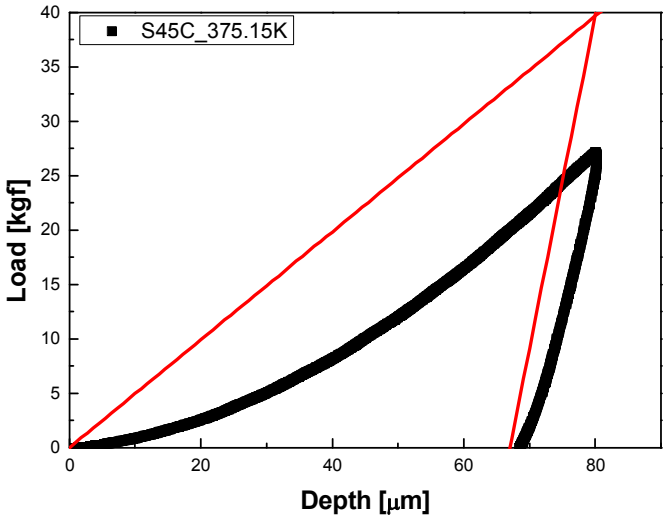

Fig. 7.16. Predicted indentation load-depth curve for S45C at 375 K

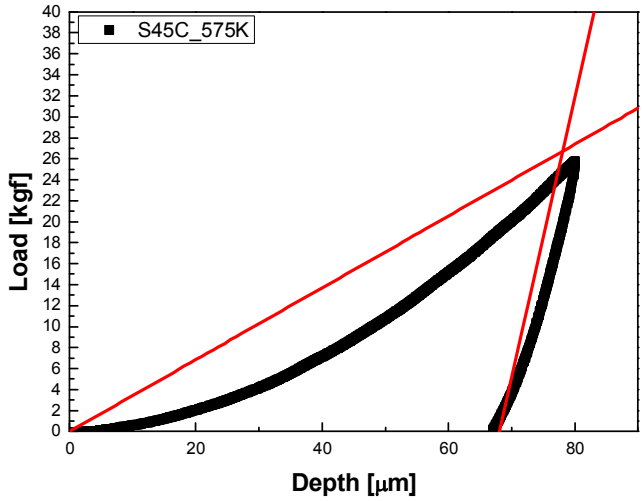

Fig. 7.17. Calibrated *L-h* curve for S45C at 575 K

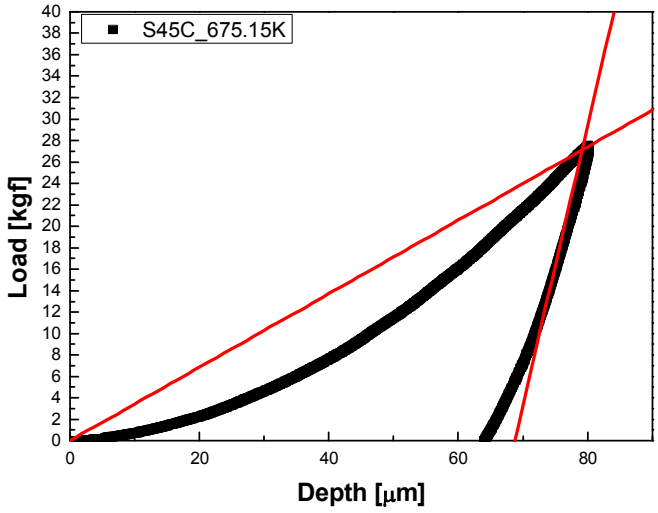

Fig. 7.18. Calibrated *L-h* curve for S45C at 675 K

References

[7.1] M. F. Doerner and W. D. Nix; A method for interpreting the data from depth-sensing indentation instruments, *J. Mater. Res.*, 1, (1986), 601-609

[7.2] J.-Y. Kim, K.-W. Lee, J.-S. Lee, D. Kwon; Determination of tensile properties by instrumented indentation technique: representative stress and strain approach, *Surface and Coatings Technology*, 201, (2006), 4278-4283

[7.3] J.-S. Lee, J.-I. Jang, B.-W. Lee, Y. Choi, S.-G. Lee, D. Kwon; An instrumented indentation technique for estimating fracture toughness of ductile materials: A critical indentation energy model based on continuum damage mechanics, *Acta Materialia*, 54, (2006), 1101-1109

[7.4] D. Ye, F. Mi, J. Liu, Y, Xu, Y. Chen, L, Xiao; Use of instrumented indentation testing to study local mechanical properties of 304L SS welded joints subjected to low-cycle fatigue loadings, *Materials Science and Engineering A*, 564, (2013), 76-84

[7.5] C. Su et al.; Measurement of power-law creep parameters by instrumented indentation methods, *J. Mech. Phys. Solids*, 61, (2013), 517–536

[7.6] C.-P. Park, et, al: Evaluation of high-temperature Vickers hardness using instrumented indentation system, *Materials Science and Engineering A*, 650, (2016), 15-19

[7.7] Andrew J. Gayle and Robert F. Cook; Mapping Viscoelastic and Plastic Properties of Polymers and Polymer-Nanotube Composites using Instrumented Indentation, J Mater Res, 31, (2016), 2347-2360

[7.8] C.A. Schuh et al.; A survey of instrumented indentation studies on metallic glasses, *J. Mater. Res*., 19, (2004), 46-57

[7.9] Jaroslav Mencík, Li Hong He, Michael V. Swain; Determination of viscoelastic–plastic material parameters of biomaterials by instrumented indentation, *J. Mech. Beha. Bio. Mate*., 2, (2009), 318-325

[7.10] J. Hay; Introduction to instrumented indentation testing, *Experimental Techniques*, (2009), 66-72

[7.11] Bharat Bhushan, et. al; Nanoindentation and picoindentation measurements using a capacitive transducer system in atomic force microscopy, *J. Philosophical Magazine A*, 74, (1996), 1117-1128

[7.12] J. M. Wheeler, D. E. J. Armstrong, W. Heinz, R. Schwaiger; High temperature nanoindentation: The state of the art and future challenges, *Current Opinion in Solid State and Materials Science*, 19, (2015), 354–366 355

[7.13] lan N. Sneddon; Boussinesq's problem for a rigid cone, *Mathematical Proceedings of the Cambridge Philosophical Society*, 44, (1948), 492-507

[7.14] K. L. Johnson; The correlation of indentation experiments, J. Mech. Phys. Solids, 18, (1970), 115-126

[7.15] X. L. Gao; An expanding cavity mode incorporating strain-hardening and indentation size effects, *International Journal of Solid and Structures*, 43, (2006), 6615-6629

[7.16] G. R Johnson and W. H. A. Cook; A constitutive model and data for metals subjected to large strains, high strain rates and high temperature, *Proc. of 7th Int. Symp. on Ballistics,* (1983), 541-547

[7.17] W. J. Kang, et. al; Modified Johnson-Cook model for vehicle body crashworthiness simulation, *Int. J. Vehicle Design*, 21, (1999), 424-435

[7.18] Y. T. Cheng and C. M. Cheng; Relationships between hardness, elastic modulus, and work of indentation, Applied Physics Letters, 73, (1998), 614-616

[7.19] online materials information resource – MatWeb, http://www.matweb.com

[7.20] C.A. Schuh, C.E. Packard, A.C. Lund; Nanoindentation and contact mode ima□ging at high-temperatures, *J. Mater. Res*. 21 (3) (2006) 725.

[7.21] B.D. Beake, J.F. Smith; High-temperature nanoindentation testing of fused silica and other materials, *Philos. Mag. A* 82 (2002) 2179.

[7.22] J.F. Smith, S. Zheng; High-temperature nanoscale mechanical property measurement, *Surf. Eng,* 16 (2000) 143

[7.23] J.S. Lee, J.I. Jang, B.W. Lee, Y. Choi, S.G. Lee, D. Kwon, An instrumented indentation technique for estimating fracture toughness of ductile materials: A critical indentation energy model based on continuum damage mechanics, *Acta Mater*. 54 (2006) 1101.

[7.24] Y. Choi, H.S. Lee, D. Kwon, Analysis of sharp-tip-indentation load-depth curve for contact area determination taking into account pile-up and sink-in effects, *J. Mater. Res*. 19 (2004) 3307.

[7.25] S.K. Kang, J.Y. Kim, C.P. Park, H.U. Kim, D. Kwon, Conventional Vickers and true instrumented indentation hardness determined by instrumented indentation test, *J. Mater. Res*. 25 (2010) 2.

[7.26] W. C. Oliver and G. M. Pharr, An improved technique for determining hardness and elastic modulus using load and displacement sensing indentation experiments, *J. Mater, Res.*, 7 (1992) 1564-1583

[7.27] O. Mustak, G. E. Evcil, C. Simsir; Simulation of through-hardening of SAE 52100 steel bearing – part 1: determination of material properties, *Mat, -wiss, u, Werkstofftech*, 47, (2016), 735 – 745

[7.28] Hideo Yoshinaga, Zenji Horita and Hiroaki Kurishita; Determination of high-temperature deformation mechanism in crystalline materials by the strain-rate change test, *Acta matallurgica*, 29, (1981), 1815-1824

[7.29] K. Toma, H. Yoshinaga, S. Morozumi, *J. Japan Inst*. Metals, 39 (1975), p. 621

[7.30] K. Toma, H. Yoshinaga, S. Morozumi, *Trans. Japan Inst. Metals*, 17 (1976), 102

[7.31] K. Abe, H. Yoshinaga, S. Morozumi, *Trans. Japan Inst. Metals*, 18 (1977), p. 479

[7.32] H. Oikawa, K. Sugawara, *Scripta metall.*, 12 (1978), 85

[7.33] H. Oikawa, *Phil. Mag.*, A37 (1978), 707

[7.34] A. E. Giannakopoulos and S. Suresh; Determination of elastoplastic properties by instrumented sharp indentation, *Scripta Materialia*, 40, (1999), 1191–1198

[7.35] Y. T. Cheng and C. M. Cheng; Relationship between hardness, elastic modulus, and the work of indentation, *Applied physics letters*, 73, (1998), 614-616

[7.36] Tabor D. The hardness of metals. Oxford: Oxford University Press; 1951.

[7.37] M. E. Roy, L. A. Whiteside, J. Xu, and B. J. Katerberg; Diamond-like carbon coatings enhance the hardness and resilience of bearing surfaces for use in joint arthroplasty, *Acta Biomaterialia*, 6, (2010), 1619–1624

[7.38] J. W. Harding and I. N. Sneddon; The elastic stresses produced by the indentation of the plane surface of a semi-infinite elastic solid by a rigid punch, *Mathematical proceedings of the cambridge philosophical society*, 41, (1945), 16-26

[7.39] Ping Wu, Tanya Wu; Temperature-dependent modulus of resilience in metallic solid calculated from strain-electro-phonon interactions, *J. Alloys and Compounds*, 705, (2017), 269-272

[7.40] Einstein, Albert; Die Plancksche Theorie der Strahlung und die Theorie der spezifischen Wärme, *Annalen der Physik*, 327(1), (1906), 180–190.

[7.41] D. Caillard and J. L. Martin; Thermally Activated Mechanisms in Crystal Plasticity, *Amsterdam: Pergamon*, 2003.

[7.42] A.S. Argon; Plastic deformation in metallic glasses, *Acta Metallurgica*, 27, (1979), 47-58.

[7.43] Baoxing Xu, Zhufeng Yue and Xi Chen; Characterization of strain rate sensitivity and activation volume using the indentation relaxation test, *J. Phys. D: Appl. Phys.* 43, (2010) 1-5

[7.44] Riqiang Liang, Akhtar S. Khan; A critical review of experimental results and constitutive models for BCC and FCC metals over a wide range of strain rates and temperatures, *International Journal of Plasticity*, 15, (1999), 963-980

[7.45] Dipti Samantaray, Sumantra Mandal, A.K. Bhaduri; A comparative study on Johnson Cook, modified Zerilli–Armstrong and Arrhenius-type constitutive models to predict elevated temperature flow behaviour in modified 9Cr–1Mo steel, *Computational Materials Science*, 47, (2009), 568–576

[7.46] Y.C. Lin, Xiao-Min Chen, Ge Liu; A modified Johnson–Cook model for tensile behaviors of typical high-strength alloy steel, *Materials Science and Engineering A* , 527, (2010), 6980–6986

[7.47] William K. Rule and S. E. Jones; A revised form for the Johnson-Cook strength model, *Int. J. Impact Eng*, 21, (1998), 609—624

[7.48] Y.C. Lin, Ming-Song Chen, Jue Zhong; Prediction of 42CrMo steel flow stress at high temperature and strain rate, *Mechanics Research Communications*, 35 (2008), 142–150.

[7.49] D. Umbrelloa, R. M'Saoubib, J.C. Outeiroc; The influence of Johnson–Cook material constants on finite element simulation of machining of AISI 316L

steel, *International Journal of Machine Tools & Manufacture*, 47, (2007), 462–470

[7.50] Anthony C. Fischer-Cripps; Nanoindentation, *Springer*, (2002).

[7.51] S. N. G. Chu, J. C. M. Li; Impression creep; a new creep test, *Journal of Materials Science*, 12, (1977), 2200–2208.

[7.52] K. L. Johnson; *Contact Mechanics, first ed. Cambridge University Press*, New York, (1985)

[7.53] C. J. Studman, M. A. Moore and S. E. Jones; On the correlation of indentation experiments, *Journal of Physics. D: Applied Physics*., 949, (1977), 949-956.

Chapter 8

Conclusions

In this thesis, elastic, elastoplastic contact mechanism, contact area, hardness, and prediction of indentation load-depth curve are explored at high-temperature. The primary results of this thesis are as follows.

In the study of determination of contact area, an instrumented indentation system for high-temperatures was developed and measurement-errors caused by equipment temperature were calibrated.

In addition, the pileup effect during indentation was studied at different temperatures. A new equation for the high-temperature contact area is proposed. For verification, conventional hardness testing was performed to compare the results with high-temperature instrumented indentation testing.

In the study of evaluation of hot-hardness, the high-temperature deformation behaviors of eight Cr-Mn alloy steels are investigated over a wide temperature range. The hardness-temperature relation of the conventional Westbrook model is newly modified to contain more physical meaning by considering the effect of temperature.

Additionally, a comprehensive relation equation is developed using indentation-depth parameters to describe the contact area at high temperatures. The results show that the calculated contact area agrees well with measured contact area, and the hardness values calculated by the new contact-area equation also agree well with experimental results. These results confirm that the new comprehensive contact-area equation can give an accurate and precise estimate of the Vickers hardness of Cr-Mn alloy steels.

In the study of prediction of load-depth curve, the study suggests a new method to predict high-temperature indentation curves using room-temperature macro-scale instrumented indentation testing. To predict the indentation curve, the thermal and mechanical characteristics of six BCC metal alloys were investigated through differential scanning calorimeter testing and instrumented indentation testing.

Physical investigations on the elastic recovery phenomenon of an indentation mark after unloading confirm that it can be expressed in terms of work, resilience, and indentation stiffness. It is also confirmed that elastic recovery of impression mark can be explained by internal energy or Helmholtz free energy through thermodynamic analysis. Thus, by tracing the entropy flow which dominates the high-temperature indentation process, we can prove experimentally a proportional relationship between stiffness and inverse Helmholtz free energy and can obtain an equation describing this relation.

In addition, a temperature-dependent indentation depth function, some geometric assumptions about the indentation curve, and experimental conditions are also introduced for predicting the high-temperature indentation curve. The indentation curves predicted are consistent with the actual indentation curves measured at the corresponding temperature within a fifteen percent error range. This study provides a new perspective on the analysis of the indentation load-depth curve and lets us interpret the mathematical relevance and physical meaning of the parameters to be considered in high-temperature studies.

References

[2.1] Boussinesq, J. Applications des potentiels, Paris, 1885

[2.2] Allan F. Bower, Analytical techniques and solutions for linear elastic solid, Chapter 5, *Applied Mechanics of Solids*, CRC Press, 2009

[2.3] lan N. Sneddon; Boussinesq's problem for a rigid cone, *Mathematical Proceedings of the Cambridge Philosophical Society*, 44, (1948), 492-507

[2.4] J. W. Harding and I. N. Sneddon; The elastic stresses produced by the indentation of the plane surface of a semi-infinite elastic solid by a rigid punch, *Mathematical proceedings of the cambridge philosophical society*, 41, (1945), 16-26

[3.1] Titchmarsh, E. C. An introduction to the theory of Fourier integrals (*Oxford*, 1937), p334.

[3.2] Busbridge, I. W. *Proc. London Math. Soc*. (2), 44 (1938), 115-30

[3.3] Love, A. E. H. *Quart. J. Math*. 10, (1939), 161

[4.1] R. Hill, E. H. Lee, S. J. Tupper, The theory of wedge indentation of ductile materials, *Proc, R. Soc. Lond*. A 188, 273 (1947)

[4.2] K.L. Johnson, Contact Mechanics, *Cambridge University Press*, Cambridge (1985).

[4.3] K.L. Johnson, *J. Mech. Phys*. Sol.18, 115 (1970).

[4.4] R. Hill,The Mathematical Theory of Plasticity, *Clarendon Press*, *Oxford* (1950).

[4.5] R.F. Bishop, R. Hill, N.F. Mott, The theory of indentation and hardness tests, *Proceeding, Physics Society* 57, 147 (1945).

[5.1] W.C. Oliver and G.M. Pharr: An improved technique for determining hardness and elastic-modulus using load and displacement sensing indentation experiments. *J. Mater. Res*. 7, 1564 (1992).

[5.2] W.C. Oliver and G.M. Pharr: Measurement of hardness and elastic modulus by instrumented indentation: Advances in understanding and refinements to methodology. *J. Mater. Res*. 19, 3 (2004).

[5.3] A. Bolshakov and G.M. Pharr: Influences of pileup on the measurement of mechanical properties by load and depth-sensing indentation techniques. *J. Mater. Res*. 13, 1049 (1998).

[5.4] Y.-H. Lee, D. Kwon: Estimation of biaxial surface stress by instrumented indentation with sharp indenters, *Acta Mater*. 52, 1555 (2004)

[5.5] S.I. Bulychev, V.P. Alekhin, M.Kh. Shorshorov and A.P. Ternovskii: Mechanical properties of materials studied from kinetic diagrams of load versus depth of impression during microimpression. *Prob. Prochn.* 9, 79 (1976)

[5.6]. J.C. Hay, A. Bolshakov and G.M. Pharr: A critical examination of the fundamental relations used in the analysis of nanoindentation data. *J. Mater. Res*. 14, 2296 (1999)

[5.7] E.G. Herbert, G.M. Pharr, W.C. Oliver, B.N. Lucas, J.L. Hay: On the measurement of stress-strain curves by spherical indentation. *Thin Solid Films*. 398–399, 331 (2001).

[5.8] J.S. Lee, J.I. Jang, B.W. Lee, Y. Choi, S.G. Lee, D. Kwon: An instrumented indentation technique for estimating fracture toughness of ductile materials: A critical indentation energy model based on continuum damage mechanics. *Acta Mater*. 54, 1101 (2006)

[5.9] S. Suresh, A.E. Giannakopoulos: A new method for estimating residual stresses by instrumented sharp indentation. *Acta Mater*. 465, 755 (1998)

[5.10] K.L. Johnson: Contact Mechanics, *Cambridge University Press*, Cambridge, UK (1985)

[5.11] J.-H. Ahn, Y. Choi and D. Kwon: Evaluation of plastic flow properties of materials through the analysis of indentation load-depth curve. *Kor. Inst. Met. & Mat*. 38, 16067 (2000)

[5.12] Y.T. Cheng and C.M. Cheng: Relationships between hardness, elastic modulus, and the work of indentation. *Appl. Phys*. Lett. 73, 614 (1998).

[5.13] Y.T. Cheng and C.M. Cheng: What is indentation hardness? *Surf. Coat. Technol*. 133–134, 417 (2000).

[5.14] J. Alcala, A.C. Barone, and M. Anglada: The influence of plastic hardening on surface deformation modes around Vickers and spherical indents. *Acta Mater*.

48, 3451 (2000).

[5.15] Y. Choi, H.S. Lee, and D. Kwon: Analysis of sharp-tip-indentation load-depth curve for contact area determination taking into account pile-up and sink-in effects. *J. Mater. Res*. 19, 3307 (2004).

[5.16] S.K. Kang, J.Y. Kim, C.P. Park, H.U. Kim and D. Kwon: Conventional Vickers and true instrumented indentation hardness determined by instrumented indentation test. *J. Mater. Res* 25, 2 (2010).

[5.17] C.A. Schuh, C.E. Packard, and A.C. Lund: Nanoindentation and Contact Mode Imaging at High-Temperatures. *J. Mater. Res.* 21(3), 725 (2006)

[5.18] B.D. Beake and J.F. Smith: High-temperature nanoindentation testing of fused silica and other materials. *Philos. Mag*. A82, 2179 (2002)

[5.19] J.F. Smith and S. Zheng: High-temperature nanoscale mechanical property measurement. *Surf. Eng*. 16, 143 (2000)

[5.20] B.N. Lucas and W.C. Oliver: Indentation Power-Law Creep of High Purity Indium. *Metall. Mater. Trans.* 30A, 601 (1999)

[5.21] C.A. Schuh, J.K. Mason, and A.C. Lund: Quantitative insight into dislocation nucleation from high-temperature nanoindentation experiments. *Nat. Mater*. 4. 617 (2005)

[5.22] Y.Y. Lim, A.J. Bushby and M.M. Chaudhri: Nano and macro indentation studies of polycrystalline copper using spherical indenters. *Mater. Res. Soc. Symp. Proc.* 522, 145 (1998)

[5.23] Y.Y. Lim, M.M. Chaudhri and Y. Enomoto: Accurate determination of the mechanical properties of thin aluminium films deposited on sapphire flats using nanoindentation. *J. Mater. Res.* 14, 2314 (1999)

[5.24] M. Riaz and N. Atiqah: A study on the mechanical properties of S45C medium type carbon steel specimens under lathe machining and quenching condition. *IJRET*. 3, 12 (2014)

[5.25] George E. Dieter: Mechanical Metallurgy (third edition), *University of Maryland*, McGraw-Hill Inc, USA (1986)

[5.26] ISO/FDIS 14577-1: Metallic Materials-Instrumented Indentation Test for Hardness and Materials Parameters; Part 1, Test Method, *International Organization for Standardization*, Geneva, Switzerland, (2002)

[6.1] Danijela Anica Skobir,Matjaz Godec,a Monika Jenkoa and Bostjan Markoli; Characterization of the carbides in the steel X20CrMoV12.1 used in Thermal power plants; *Surf. Interface Anal*. 40, (2008), 513–517

[6.2] W. L. MankinsJ. C. HosierT. H. Bassford; Microstructure and phase stability of INCONEL alloy 617; *Metallurgical Transactions*, 5, (1974), 2579 -2590

[6.3] V. A. Popovich, M. P. F. H. L. van Maris, M. Janssen, I. J. Bennett, I. M. Richardson; Understanding the properties of silicon solar cells aluminium contact layers and its effect on mechanical stability; *Materials Sciences and Applications*, 4, (2013), 118-127

[6.4] D. R. Kim, S. M. Yang and H. S. Y; Material property evaluation of high temperature creep for Pb-free solder joints of Sn-Ag-(Cu) types; *KSME*, (2012), 313-318

[6.5] E. R. Petty; Hardness and Other Physical Properties of Metals in Relation to Temperature; *Metallurgia*, 56, (1957), 337, 231-236.

[6.6] D. Tabor; A simple theory of static and dynamic hardness; *Proc R Soc. London A* 192, (1948), 247–274.

[6.7] Kirity Bhusan Khan, T. R. G. Kutty, M. K. Surappa; Hot hardness and indentation creep study on Al-5% Mg alloy matrix-B_4C particle reinforced composites; *Materials Science and Engineering A* 427, (2006), 76-82.

[6.8] Yichun Zhang, Tielin Shi, Zirong Tang, Guanglan Liao; An improved method to estimate Young's modulus of Zr-based BMGs accounting for pile-up during nanoindentation; *Journal of Non-Crystalline Solids*, 427, (2015), 20-25.

[6.9] Chan-Pyoung Park, Jung-Jun Lee, Seung-Kyun Kang, Young-Cheon Kim, Kwan-Sik Woo, Seung-Won Jeon, Dongil Kwon; Evaluation of high-temperature Vickers hardness using instrumented indentation system; *Materials Science and Engineering A*, 650, (2016), 15-19.

[6.10] W. C. Oliver, G. M. Pharr; An improved technique for determining hardness and elastic-modulus using load and displacement sensing indentation experiments; *J. Mater. Res*, 7, (1992), 1564.

[6.11] J. H. Westbrook; Temperature dependence of hardness of the equi-atomic iron group aluminides; *Journal of the Electrochemical Society*, 103, (1956), 54-63.

[6.12] George E. Dieter; Mechanical Metallurgy; *McGraw-Hill Book Company (UK) Si Metric Edition*, (1988).

[6.13] Chin-You Hsu, Woei-Ren Wang, Wei-Yeh Tang, Swe-Kai Chen and Jien -Wei Yeh; Microstructure and mechanical properties of new AlCoxCrFeMo0.5Ni high-entropy alloys; *Advanced Engineering Materials*, (2010), 44-49

[6.14] J.S. Lee, J.I. Jang, B.W. Lee, Y. Choi, S.G. Lee, D. Kwon; An instrumented indentation technique for estimating fracture toughness of ductile materials: A critical indentation energy model based on continuum damage mechanics; *Acta Mater.* 54, (2006), 1101.

[6.15] Y. Choi, H.S. Lee, D. Kwon; Analysis of sharp-tip-indentation load-depth curve for contact area determination taking into account pile-up and sink-in effects; *J. Mater. Res*. 19, (2004), 3307.

[6.16] S.K. Kang, J.Y. Kim, C.P. Park, H.U. Kim, D. Kwon; Conventional Vickers and true instrumented indentation hardness determined by instrumented indentation test; *J. Mater. Res*. 25, (2010), 2.

[6.17] T. Maki, I. Tamura; Deformation behaviors of metals and alloys at Elevated temperatures: 2. dynamic recrystallization and its related phenomena; *Journal of the Society of Materials Science*, 30, (1981), 329, 211-217

[6.18] S. E. Ion, F. J. Humphreys, S. H. White; Dynamic recrystallisation and the development of microstructure during the high temperature deformation of magnesium; *Acta Metallurgica*, 30, (1982), 10, 1909-1919.

[6.19] H. D. Merchant, G. S. Murty, S. N. Bahadur, L.T. Dwivedi, Y. Mehrotra; Hardness-temperature relationships in metals; *Journal of Materials Science*, 8, (1973), 437-442

[6.20] Akio Kagawa, Taira Okamoto, Kazuo Saito, Minoru Ohta; Hot hardness of $(Fe, Cr)_3C$ and $(Fe, Cr)_7C_3$ carbides; *Journal of Materials Science*, 19, (1954), 2546-2554

[6.21] V. A. Borisenko; Investigation of the temperature dependence of the hardness of molybdenum in the range of 20-2500°C; *Translated from Poroshkovaya Metallurgiya*, 2, (1962), 55-61.

[6.22] Chin-You Hsu, Woei-Ren Wang, Wei-Yeh Tang, Swe-Kai Chen and Jien-Wei Yeh; Microstructure and mechanical properties of new AlCoxCrFeMo0.5Ni high-Entropy alloys; *Advanced Engineering Materials*, 12, (2010), 44-49.

[6.23] Schweitzer, E; Goken, M; The grain boundary hardness in austenitic stainless steels studied by nanoindentations; *Zeitschrift Fur Metallkunde*, 95, (2004), 492-498.

[6.24] Kittel, Charles, Herbert Kroemer; Thermal Physics 2nd edition; *New York Freeman and Company*, (1980).

[6.25] Arrhenius, S.A.; Über die Dissociationswärme und den Einfluß der Temperatur auf den Dissociationsgrad der Elektrolyte; *Z. Phys. Chem.* **4,** (1889), 96–116.

[6.26] Zener, C., Hollomon. J. H; Effect of strain rate upon plastic flow of steel; *Journal of Applied Physics*, 15, (1944), 22-32.

[6.27] C. M. Sellars, W. J. Mc Tegart; On the mechanism of hot deformation; *Acta Metallurgica*, 14, (1966), 1136-1138.

[6.28] Z. S. Basinski; Activation energy for creep of aluminium at sub-atomspheric temperature; Acta Metallurgica, 5, (1957), 684

[6.29] V. Vitek and F. Kroupa; Dislocation theory of slip geometry and temperature dependence of flow stress in B. C. C. Metals; *Phys. Stat. Sol.* 18, (1966), 703

[6.30] George-Maria Schwab; Some new aspects of the strength of alloys; Transactions of the Faraday Society, 45, (1949), 385.

[6.31] O. D. Sherby and P. E. Armstrong; Prediction of activation energies for creep and self-diffusion from hot hardness data; *Metallurgical Transactions*, 2, (1971), 3479.

[6.32] S.I. Bulychev, V.P. Alekhin, M.K. Shorshorov, A.P. Ternovskii, and G.D. Shnyrev; Determining Young's modulus from the indentor penetration diagram; *Zavod. Lab.* 41, (1975), 1137.

[6.33] M.F. Doerner and W.D. Nix; A method for interpreting the data from depth-sensing indentation instruments; *J. Mater. Res.* 1, (1986), 601.

[6.34] J.L. Bucaille, S. Stauss, E. Felder, and J. Michler; Determination of plastic properties of metals by instrumented indentation using different sharp indenters. *Acta Mater.* 51, (2003), 1663.

[6.36] Yun-Hee Lee and Dongil Kwon; Residual stresses in DLC/Si and Au/Si systems: Application of a stress-relaxation model to the nanoindentation technique*; J. Mater. Res*, 17, (2002), 901-906.

[6.37] J. S. Tse; Intrinsic hardness of crystalline solids; *Journal of Superhard Materials*, 32, (2010), 177-191.

[6.38] N. A. Stilwell and D. Tabor; Elastic recovery of conical indentations; *Proc.Phys. Soc*. 78, (1961), 169.

[6.39] Y.T. Cheng and C.M. Cheng; Relationships between hardness, elastic modulus, and the work of indentation. *Appl. Phys. Lett*. 73, (1998), 614.

[7.1] M. F. Doerner and W. D. Nix; A method for interpreting the data from depth-sensing indentation instruments, *J. Mater. Res.*, 1, (1986), 601-609

[7.2] J.-Y. Kim, K.-W. Lee, J.-S. Lee, D. Kwon; Determination of tensile properties by instrumented indentation technique: representative stress and strain approach, *Surface and Coatings Technology*, 201, (2006), 4278-4283

[7.3] J.-S. Lee, J.-I. Jang, B.-W. Lee, Y. Choi, S.-G. Lee, D. Kwon; An instrumented indentation technique for estimating fracture toughness of ductile materials: A critical indentation energy model based on continuum damage mechanics, *Acta Materialia*, 54, (2006), 1101-1109

[7.4] D. Ye, F. Mi, J. Liu, Y, Xu, Y. Chen, L, Xiao; Use of instrumented indentation testing to study local mechanical properties of 304L SS welded joints subjected to low-cycle fatigue loadings, *Materials Science and Engineering A*, 564, (2013), 76-84

[7.5] C. Su et al.; Measurement of power-law creep parameters by instrumented indentation methods, *J. Mech. Phys. Solids*, 61, (2013), 517–536

[7.6] C.-P. Park, et, al: Evaluation of high-temperature Vickers hardness using instrumented indentation system, *Materials Science and Engineering A*, 650, (2016), 15-19

[7.7] Andrew J. Gayle and Robert F. Cook; Mapping Viscoelastic and Plastic Properties of Polymers and Polymer-Nanotube Composites using Instrumented Indentation, J Mater Res, 31, (2016), 2347-2360

[7.8] C.A. Schuh et al.; A survey of instrumented indentation studies on metallic glasses, *J. Mater. Res.*, 19, (2004), 46-57

[7.9] Jaroslav Mencík, Li Hong He, Michael V. Swain; Determination of viscoelastic–plastic material parameters of biomaterials by instrumented indentation, *J. Mech. Beha. Bio. Mate.*, 2, (2009), 318-325

[7.10] J. Hay; Introduction to instrumented indentation testing, *Experimental Techniques*, (2009), 66-72

[7.11] Bharat Bhushan, et. al; Nanoindentation and picoindentation measurements using a capacitive transducer system in atomic force microscopy, *J. Philosophical Magazine A*, 74, (1996), 1117-1128

[7.12] J. M. Wheeler, D. E. J. Armstrong, W. Heinz, R. Schwaiger; High temperature nanoindentation: The state of the art and future challenges, *Current Opinion in Solid State and Materials Science*, 19, (2015), 354–366 355

[7.13] lan N. Sneddon; Boussinesq's problem for a rigid cone, *Mathematical Proceedings of the Cambridge Philosophical Society*, 44, (1948), 492-507

[7.14] K. L. Johnson; The correlation of indentation experiments, J. Mech. Phys. Solids, 18, (1970), 115-126

[7.15] X. L. Gao; An expanding cavity mode incorporating strain-hardening and indentation size effects, *International Journal of Solid and Structures*, 43, (2006), 6615-6629

[7.16] G. R Johnson and W. H. A. Cook; A constitutive model and data for metals subjected to large strains, high strain rates and high temperature, *Proc. of 7th Int. Symp. on Ballistics,* (1983), 541-547

[7.17] W. J. Kang, et. al; Modified Johnson-Cook model for vehicle body crashworthiness simulation, *Int. J. Vehicle Design*, 21, (1999), 424-435

[7.18] Y. T. Cheng and C. M. Cheng; Relationships between hardness, elastic modulus, and work of indentation, Applied Physics Letters, 73, (1998), 614-616

[7.19] online materials information resource – MatWeb, http://www.matweb.com

[7.20] C.A. Schuh, C.E. Packard, A.C. Lund; Nanoindentation and contact mode ima□ging at high-temperatures, *J. Mater. Res*. 21 (3) (2006) 725.

[7.21] B.D. Beake, J.F. Smith; High-temperature nanoindentation testing of fused silica and other materials, *Philos. Mag. A* 82 (2002) 2179.

[7.22] J.F. Smith, S. Zheng; High-temperature nanoscale mechanical property measurement, *Surf. Eng,* 16 (2000) 143

[7.23] J.S. Lee, J.I. Jang, B.W. Lee, Y. Choi, S.G. Lee, D. Kwon, An instrumented indentation technique for estimating fracture toughness of ductile materials: A critical indentation energy model based on continuum damage mechanics, *Acta Mater*. 54 (2006) 1101.

[7.24] Y. Choi, H.S. Lee, D. Kwon, Analysis of sharp-tip-indentation load-depth curve for contact area determination taking into account pile-up and sink-in effects, *J. Mater. Res*. 19 (2004) 3307.

[7.25] S.K. Kang, J.Y. Kim, C.P. Park, H.U. Kim, D. Kwon, Conventional Vickers and true instrumented indentation hardness determined by instrumented indentation test, *J. Mater. Res*. 25 (2010) 2.

[7.26] W. C. Oliver and G. M. Pharr, An improved technique for determining hardness and elastic modulus using load and displacement sensing indentation experiments, *J. Mater, Res.*, 7 (1992) 1564-1583

[7.27] O. Mustak, G. E. Evcil, C. Simsir; Simulation of through-hardening of SAE 52100 steel bearing – part 1: determination of material properties, *Mat, -wiss, u, Werkstofftech*, 47, (2016), 735 – 745

[7.28] Hideo Yoshinaga, Zenji Horita and Hiroaki Kurishita; Determination of high-temperature deformation mechanism in crystalline materials by the strain-rate change test, *Acta matallurgica*, 29, (1981), 1815-1824

[7.29] K. Toma, H. Yoshinaga, S. Morozumi, *J. Japan Inst*. Metals, 39 (1975), p. 621

[7.30] K. Toma, H. Yoshinaga, S. Morozumi, *Trans. Japan Inst. Metals*, 17 (1976), 102

[7.31] K. Abe, H. Yoshinaga, S. Morozumi, *Trans. Japan Inst. Metals*, 18 (1977), p. 479

[7.32] H. Oikawa, K. Sugawara, *Scripta metall.*, 12 (1978), 85

[7.33] H. Oikawa, *Phil. Mag.*, A37 (1978), 707

[7.34] A. E. Giannakopoulos and S. Suresh; Determination of elastoplastic properties by instrumented sharp indentation, *Scripta Materialia*, 40, (1999), 1191–1198

[7.35] Y. T. Cheng and C. M. Cheng; Relationship between hardness, elastic modulus, and the work of indentation, *Applied physics letters*, 73, (1998), 614-616

[7.36] Tabor D. The hardness of metals. Oxford: Oxford University Press; 1951.

[7.37] M. E. Roy, L. A. Whiteside, J. Xu, and B. J. Katerberg; Diamond-like carbon coatings enhance the hardness and resilience of bearing surfaces for use in joint arthroplasty, *Acta Biomaterialia*, 6, (2010), 1619–1624

[7.38] J. W. Harding and I. N. Sneddon; The elastic stresses produced by the indentation of the plane surface of a semi-infinite elastic solid by a rigid punch, *Mathematical proceedings of the cambridge philosophical society*, 41, (1945), 16-26

[7.39] Ping Wu, Tanya Wu; Temperature-dependent modulus of resilience in metallic solid calculated from strain-electro-phonon interactions, *J. Alloys and Compounds*, 705, (2017), 269-272

[7.40] Einstein, Albert; Die Plancksche Theorie der Strahlung und die Theorie der spezifischen Wärme, *Annalen der Physik*, 327(1), (1906), 180–190.

[7.41] D. Caillard and J. L. Martin; Thermally Activated Mechanisms in Crystal Plasticity, *Amsterdam: Pergamon*, 2003.

[7.42] A.S. Argon; Plastic deformation in metallic glasses, *Acta Metallurgica*, 27, (1979), 47-58.

[7.43] Baoxing Xu, Zhufeng Yue and Xi Chen; Characterization of strain rate sensitivity and activation volume using the indentation relaxation test, *J. Phys. D: Appl. Phys.* 43, (2010) 1-5

[7.44] Riqiang Liang, Akhtar S. Khan; A critical review of experimental results and constitutive models for BCC and FCC metals over a wide range of strain rates and temperatures, *International Journal of Plasticity*, 15, (1999), 963-980

[7.45] Dipti Samantaray, Sumantra Mandal, A.K. Bhaduri; A comparative study on Johnson Cook, modified Zerilli–Armstrong and Arrhenius-type constitutive

models to predict elevated temperature flow behaviour in modified 9Cr–1Mo steel, *Computational Materials Science*, 47, (2009), 568–576

[7.46] Y.C. Lin, Xiao-Min Chen, Ge Liu; A modified Johnson–Cook model for tensile behaviors of typical high-strength alloy steel, *Materials Science and Engineering A* , 527, (2010), 6980–6986

[7.47] William K. Rule and S. E. Jones; A revised form for the Johnson-Cook strength model, *Int. J. Impact Eng*, 21, (1998), 609—624

[7.48] Y.C. Lin, Ming-Song Chen, Jue Zhong; Prediction of 42CrMo steel flow stress at high temperature and strain rate, *Mechanics Research Communications*, 35 (2008), 142–150.

[7.49] D. Umbrelloa, R. M'Saoubib, J.C. Outeiroc; The influence of Johnson–Cook material constants on finite element simulation of machining of AISI 316L steel, *International Journal of Machine Tools & Manufacture*, 47, (2007), 462–470

[7.50] Anthony C. Fischer-Cripps; Nanoindentation, *Springer*, (2002).

[7.51] S. N. G. Chu, J. C. M. Li; Impression creep; a new creep test, *Journal of Materials Science*, 12, (1977), 2200–2208.

[7.52] K. L. Johnson; *Contact Mechanics, first ed. Cambridge University Press*, New York, (1985)

[7.53] C. J. Studman, M. A. Moore and S. E. Jones; On the correlation of indentation experiments, *Journal of Physics. D: Applied Physics*., 949, (1977), 949-956.

초 록

계장화 압입 시험은 압입 하중을 인가하여 발생하는 변위를 연속적으로 측정하여 탄성계수 및 경도와 같은 기초적인 기계적 물성 평가에서부터 인장강도, 파괴인성, 피로 그리고 크립과 같은 기계적 물성을 평가할 수 있는 시험법이다. 압입시험이 기존의 기계적 시험에 비교해서 갖고 있는 최고의 장점은 시험에 필요한 재료의 부피가 매우 작다는 것이다. 이러한 특성으로 인해 간편성, 경제적, 비파괴적, 그리고 현장 적용성 등의 장점들이 파생된다. 따라서 일반 금속에서부터 폴리머소재, 비정질 소재 그리고 바이오소재 등의 다양한 소재에 적용 가능하다. 또한 매크로 스케일에서부터 나노/피코 스케일까지 광범위한 영역에서 활용되고 있다. 하지만 계장화 압입시험법에 대한 연구는 그 동안 다른 기계적 시험법으로 평가할 수 있는 기계적 물성을 압입 시험법으로도 평가할 수 있다는 시험법 자체의 타당성에 대한 연구가 주류를 이루었다. 이는 고온 계장화 압입시험이 2000년대 이후에 등장한 시험법이라서 타 시험법에 비해 적은 데이터 축척량과 짧은 사용년도를 갖고 있기 때문이다. 따라서 기계적 물성을 평가하기 위한 다양한 압입-하중변위곡선의 분석법이 등장하였고, 1차 적으로 측정 되어지는 변위를 정확히 산출하고자 pileup과 sink-in을 보

정하고자 하는 많은 노력들이 있어왔다. 하지만 인덴테이션 관련 연구는 거의 대부분 상온에서 수행되어 왔으며, 고온이나 저온 혹은 부식환경과 같은 특수 환경에서의 연구는 상대적으로 적게 수행되고 있다. 그 이유는 환경적 요인 예를 들면 thermal drift 와 같은 것들이 기계적 측정에 오류를 일으킬 수 있으므로 안정적인 실험데이터 확보가 어렵기 때문이다. 본 연구에서는 이러한 선행연구들을 참고하여 오류를 최소화 하여, 매크로 스케일, 650° C까지 활용할 수 있는 고온 계장화 압입시스템 (HTIIS)을 개발하였다. 개발된 장비를 이용하여 고온에서의 정확한 접촉면적결정을 위해 압입시 금속소재 표면에서 발생하는 파일업 현상을 정량화 하고자 하였으며, 물리적 해석을 수행하였다. 또한, 파일업을 보정한 접촉면적결정을 위해 고온 파일업 보정인자 f_T를 를 새롭게 제안하였으며, 연구의 검증을 위해 기존의 고온 경도와 결과를 비교하였다. 하지만 압입 면적 보정을 위한 함수를 결정하기 위해서는 매번 해당 온도에서 실험을 수행해야 하는 한계점이 있었다. 이는 압입 면적 보정함수가 시편이나 실험환경에 의존한다는 것을 의미한다. 따라서 이러한 한계를 극복하고자 새로운 보완 연구를 추가로 실시하였다. 열역학 기반으로 정의된 기존의 구성방정식들의 형태를 기반으로 경도와 온도의 관계를 새롭게 정의하였다. 또한, 수학적 전개방식을 통해 각 파라미터 들이 가지는 물리적

의미를 고찰해 보았으며, 압입시험의 접촉깊이를 압입변수와 온도의 함수로 표현하였다. 또한, 계산된 압입깊이를 바탕으로 환산된 접촉넓이를 기존 광학관찰로부터 얻어진 접촉넓이와 비교 해 보았으며, 연구결과의 타당성을 확보하기 위해 타 기관에서 동일 소재로 얻어진 경도 값을 본 연구결과로 부터의 경도값과 상호 비교해 보았다. 하지만 이러한 기계적 접근법으로는 고온에서의 압입시험을 충분히 이해할 수 없었다. 왜냐하면 고온이라는 것은 소재에 열 에너지가 가해진다는 것을 의미하기 때문이다. 그러므로 열에 대한 학문적 고찰이 필요하였다. 기존 기계적 영역에 머무르던 압입시험을 열역학적으로 새롭게 해석 해야할 필요성이 있었다. 그러므로 우선, 기계적 파라미터인 레질리언스와 압입시험의 언로딩커브로부터 얻어낼 수 있는 스티프니스와의 관계를 고찰하였다. 또한, 스티프니스와 열역학적 파라미터인 내부에너지와의 관계를 고찰하였으며, 고온에서 하중인가와 하중제거의 과정 동안의 엔트로피의 흐름을 파악하여 스티프니스와 헬름홀츠 자유에너지와의 관계를 고찰하였다. 즉 압입시험 후 압흔이 탄성회복하는데 기여하는 엔트로피를 알아내었고 이것을 매개로 하여 기계적 인자와 열역학적 인자가 서로 결합될 수 있다는 것을 확인하였다. 마지막으로 온도에 따른 압입 깊이의 변화를 이용하여 고온에서의 로드-뎁스 커브를 예측하였으며, 상온에서 측정가능한 압입하중

을 통해 예측된 고온 커브를 교정하는 방법을 제시 할 수 있었다. 예측된 고온 로드-뎁스 커브는 실제 온도에서의 로드-뎁스 커브와 비교하여 연구결과의 타당성을 검증하였다. 본 논문을 통해 압입하중-변위곡선을 분석하는 새로운 시각을 제시할 수 있었으며, 고온 연구에서 고려되어야 할 파라미터들간의 수학적 관련성과 물리적 의미를 해석할 수 있었다.

주요어: 계장화 압입 시험, 경도, 스티프니스 (강성도), 엔트로피, 헬름홀츠 자유 에너지, 고온

학번: 2008-20649

List of Publications

I. International Journal

1. **Chan-Pyoung Park**, Jung-Jun Lee, Seung-Kyun Kang, Young-Cheon Kim, Kwan-Sik Woo, Seung-Won Jeon, Dongil Kwon: Evaluation of high-temperature Vickers hardness using instrumented indentation system, *Materials Science and Engineering A* 650 (2016) 15-19

2. Seung-Kyun Kang, Ju-Young Kim, **Chan-Pyoung Park**, Hyun-Uk Kim, Dongil Kwon: Conventional Vickers and true instrumented indentation hardness determined by instrumented indentation tests, *Journal of Materials Research* 25 (2010) 337-343

3. S. W. Jeon, K. W. Lee, J. Y. Kim, W. J. Kim, **Chan-Pyoung Park**, D. Kwon: Estimation of Fracture Toughness of Metallic Materials Using Instrumented Indentation: Critical Indentation Stress and Strain Model, *Experimental Mechanics,* 57, (2016), 1-13

II. Korean Journal

1. 이윤희, 안승민, 김주영, 박찬평, 장희광: 용해실리카의 기준경도를 이용한 나노 압입시스템의 실험적 교정 (Calibration of Nanoindentation Systems Based on the Reference Hardness of a Fused Silica), 대한금속.재료학회지 53, (2015) 162-168

III. International Conference

1. **Chan-Pyoung Park**, Seung-Kyun Kang, Won-Je Jo, Dongil Kwon: Using instrumented indentation to evaluate high-temperature mechanical properties, *ISOPE-2010*, June20-26, Beijing, China (2010)

2. S. K. Kang, Y. C. Kim, **Chan-Pyoung Park**, D. Kwon: Evaluation of tensile properties profile of weld zone using instrumented indentation, *2010 Pressure Vessels & Piping Conference,* July18-22, Washington, USA (2010)

3. D. Kwon, S. K. Kang, J. Y. Kim, Y. C. Kim, **Chan-Pyoung Park**, W. S. Song: Instrumented Indentation Test: A Method for Nondestructive Evaluation of Mechanical Properties, *8th International Conference on NDE in Relation to Structural Integrity for Nuclear and Pressured Components*, September29-October 01, Berlin, Germany (2010)

4. Seung-Kyun Kang, **Chan-Pyoung Park**, Jinwoo Lee, Dongil Kwon: Investigation pileup of metallic materials using the equivalent elastic strained volume with expanding cavity, *Fourth International Indentation Workshop (IIW4)*, July03-08, Seoul, Korea (2011)

5. **Chan-Pyoung Park**, Kug-Hwan Kim, Seung-Kyun Kang, Won-Je Jo, Dongil Kwon: Instrumented indentation testing to evaluate high-temperature material properties, *2011 Pressure Vessels & Piping Conference*, July17-21, Baltimore, USA

IV. Korean Conference

1. **박찬평**, 강승균, 권동일: 계장화 압입시험법을 이용한 벌크소재의 고온 경도 평가, 2009년도 대한금속 · 재료학회 학술대회, 04월 23-24일, 창원컨벤션센터(CECO) (2009)

2. **박찬평**, 강승균, 권동일: 고온환경에서 계장화 압입 시험 시 발생하는 pile-up 정량화를 통한 접촉면적 결정, 2009년도 대한금속 · 재료학회, 10월 22-23일, 대구컨벤션센터(EXCO) (2009)

3. 김국환, **박찬평**, 권동일: 고온 계장화압입시험의 실험조건 결정 및 압입인장물성의 평가, 2008년 대한금속 · 재료학회 학술대회, 10월 23일-24일, 송도컨벤시아 (2008)

4. 강승균, **박찬평**, 김국환, 김현욱, 권동일: 비커스 압입자를 이용한 계장화 압입시험의 접촉깊이 및 경도평가 기술, 2009년 대한금속 · 재료학회 학술대회, 4월 23일-24일, 창원컨벤션센터(CECO)(2009)

5. 이경우, 김국환, 최민재, **박찬평**, 김광호, 권동일: 계장화 압입시험을 이용한 저/고온 강도 및 파괴인성 평가, 제22회 첨단구조재료 심포지엄, POSTECH 국제관, 09월 25-26, 포항 2008

6. 강승균, **박찬평**, 김종헌, 권동일: 계장화 압입시험을 이용한 비광학식 비커스경도 측정기술, 2009년도 대한금속 · 재료학회 추계 학술대회, 10월 22-23일, 대구컨벤션센터(EXCO) (2009)

7. 김국환, **박찬평**, 권동일: 고온 계장화 압입시험법을 통한 Ti-6Al-4V 합금의 인장특성 평가, 제15차 유도무기 학술대회, 10월 29일, 국방과학연구소 (2009)

8. **박찬평**, 강승균, 권동일: 계장화 압입시험을 이용한 구조용강의 고온 경도 평가, 제15차 유도무기 학술대회, 10월 29일, 국방과학연구소 (2009)

9. 김국환, **박찬평**, 조원제, 권동일: 계장화 압입시험법을 이용한 Ti-6Al-4V 합금의 고온 변형 거동 해석, 2010년도 대한금속 · 재료학회 춘계 학술대회, 4월 22-23일, 현대성우리조트(강원도 횡성) (2010)

10. **박찬평**, 강승균, 조원제, 권동일: 계장화 압입 시험을 이용한 고온 구조물 신뢰성 평가, 2010년 한국신뢰성학회 춘계학술대회, 6월 18일, 아주대학교 율곡관, 법학관, 팔달관 (2010)

11. 강승균, **박찬평**, 이진우, 권동일: 소성쌓임 보정을 통한 압입시험의 scaling relation 해석 및 압입각과 온도 의존성 규명, 2011년도 대한금속 · 재료학회 춘계 학술대회, 04월 21-22일, 대구컨벤션센터(EXCO) (2011)

12. 김준영, 최민재, 강승균, **박찬평**, 권동일: 계장화 압입시험법의 표준화 동향 : ASME, ISO, 제25회 첨단구조재료 심포지엄, 11월 17-18일, 한국원자력안전기술원, 대전 (2011)

13. **박찬평**, 김국환, 조원제, 전승원, 권동일: 연속압입시험의 탄소성 응력해석을 통한 대표응력-대표변형률 결정, 제25회 첨단구조재료 심포지엄, 11월 17-18일, 한국원자력안전기술원, 대전 (2011)

14. 안희준, **박찬평**, 김종형, 김의수, 권동일: 해외 최신 법공학 동향 조사 및 국내 법공학 체계 구축을 위한 방안 제시, 대한기계학회 2012년도 추계학술대회, 11월 07-09일, 창원컨벤션센터 (2012)

15. 안희준, **박찬평**, 전승원, 김지연, 권동일: 법공학 도입을 통한 안전사고 예방 및 대응체계 구축 방안에 대한 연구, 2013 한국안전학회 춘계학술대회, 05월 09-10일, 서귀포 KAL호텔 (2013)

감사의 글

부족한 글재주 이지만, 이 한 권의 졸업 논문 말미에, 그간 도움을 주셨던 은사님들께 감사의 마음을 전합니다.

먼저 처음 시작이라는 기회를 주셨으며, 학위기간 동안 연구적 환경을 제공해 주셨고, 살아감에 있어 올바른 방향을 가르쳐 주신 권동일 교수님께 감사 드립니다. 지도교수님이 계셨기에 근원적인 면에서 학위를 마칠 수 있었던 것 같습니다. 한번도 과제가 끊인적이 없었고, 꾸준히 연구할 수 있었으며, 또 개인적으로 힘든 날들을 보냄에도 교수님께서 지지해 주시고, 지원해 주신부분 아마 평생 감사함으로 남을 것 같습니다.

학위논문을 지도해 주시고 바쁜 시간을 쪼개시며 심사를 해주신 분들께도 감사 드립니다. 심사위원장을 맡아 주셨고, 제 연구에 대해 조언을 해주셨던 한흥남 교수님께 감사 드립니다. 예심과정에서 제 연구의 큰 틀을 봐주시고, 코멘트가 도움이 되길 바란다는 말씀을 통해 순수한 마음으로 지적대화를 즐기는 한명의 연구자의 모습을 배울 수 있었습니다. 박은수 교수님께도 감사 드립니다. 저의 연구를 세심하게 봐주시고 부족한 포인트는 무엇인지, 보완해야 할 부분은 어디인지, 교수님의 코멘트가 없었다면 연구의 완성도는 덜 했을 것입니다. 최병학 교수님께도 감사 드립니다. 쉬운 일이 아니었을 텐데, 제 연구에 대해 진심으로 검토해 주셨고, 제 이야기를 들어주셨으며, 또 미세조직학적으로 코멘트를 주신 부분 정말 감사 드립니다. 따뜻한 말씀과 인상으로 주변분들을 대하시는 부분 또한 배움으로 남을 것 같습니다. 전은채 박사님께도 감사 드립니다. 아마 전은채 박사님의 코멘트가 없었다면 제 연구의 전체흐름을 지배하지 못하였을 것 입니다. 바쁘신 스케쥴에도 심사위원직을 수락해 주시고 함께 디스커션 해 주셔서 감사 드립니다. 학위논문을 준비하며, 지도교수님과 심사위원님들의 도움이 없었다면 완성도 높은 연구를 하지 못하였을 것입니다. 한분,한분 학자적인 면모에 감탄 스러웠으며, 학문적 깊이, 논리, 데이터 분석, 연구적 한계, 발표하는 스킬, 그리고 따뜻한 마음 배울 수 있었고, 또 저 스스로도 향상된 것 같아 감사 드립니다.

한양대 장재일 교수님께 감사 드립니다. 제자가 좋은 연구하길 바라시고, 또 좋은 진로로 나아가길 바라시고, 제자의 실패에 함께

슬퍼하시고, 제자의 잘됨에 진심으로 기뻐하셨던 교수님의 모습, 많은 귀감이 되었습니다. 또한 연구에 대한 열정과 자세, 많이 배웠고 감사했습니다.

표준연의 이윤희 박사님께 감사 드립니다. 항상 후배들에게 격없이 대해 주시고, 그래서 연구 디스커션을 편한 마음으로 많이 할 수 있었고, 또 항상 공부하시는 자세, 연구하시는 자세, 정말 많은걸 배울 수 있는 시간들이었습니다. 감사했습니다.

유니스트의 김주영 교수님과 지금은 진주에 있는 김영천 박사님께 감사 드립니다. 심적으로 많은 부분 의지하였던 것 같습니다. 진로를 결정함에 있어 김주영 교수님과 김영천 박사님의 도움을 많이 받은 것 같습니다.

연구실 선후배님들께도 감사 드립니다. 경우형, 리더가 있다면 아마 형과 같은 모습이어야 할 것 입니다. 좋은 리더의 본보기, 윗사람과 잘 소통하고, 중간에서 추진하고, 후배들을 이끌어가고 챙기는 모습 닮고 싶습니다. 국환이, 정말 똑똑하고 인자한 선배였던 것 같습니다. 연구할 때 그 탁월했던 식견, 끈기 있는 모습, 고통에도 묵묵히 견디는 모습, 정말 닮고 싶습니다. 동갑이지만 선배여서 어려웠던 민재, 주위 사람들 챙기고 또 모든 상황을 바둑판의 형세를 보듯 파악하였던 능력, 대단한 것 같습니다. 천재였던 승균이, 지금은 카이스트 교수님이 되셨지만, 머리가 좋음에도 더 무서웠던 건 부지런하고 항상 노력했다는 점. 정말 배울 게 많은 것 같습니다. 더 많이 함께 시간을 보내고 싶었지만 빨리 졸업해서 나간 상욱이형, 관식이형, 현욱이, 인근이, 아마 랩생활 더 했으면 진짜 재밌는 일들이 많았을 것 같습니다. 다들 저한테 잘해 주셔서 감사합니다.

동기였던 원석이하고 준영이, 원석이는 겉보기에 고민이 정말 하나도 없어 보였던 긍정적 에너지를 뿜어내는 사람인 것 같습니다. 함께 랩생활 할 수 있어서 고마웠습니다. 준영이는 정말 친하게 지내고 싶었는데 그러질 못해서 아쉬움이 큽니다. 앞으로 살아가면서 준영이하고 친하고 애틋하게 지내야 할 것 같습니다. 후배였던 종헌이 원재, 승원이, 희준이 다들 나 때문에 고생을 많이 한 것 같아서 미안한 마음이 큽니다. 그때 좀더 마음에 여유가 있었더라면, 좀더 크게 상황을 볼 줄 알고, 제어할 줄 알았더라면 그렇게 까진 고생시키진 않았을 텐데 다들 내가 잘해주질 못해서 미안합니다. 앞으로 살면서 잘해 드리도록 하겠습니다.

이제는 최고참이 되는 진우, 연구적으로 함께 했던 시간이 없어서 아쉽습니다. 진우의 연구를 좀 더 들여다 보고 내가 도울 수 있는 부분이 있다면 돕고 싶었는데, 앞으로의 연구과정에서 좋은 연구기회가 있다면 함께 하고 싶습니다. 개인적으로 진우의 사회성이 너무 부럽고 배우고 싶습니다. 여러 사람들과 함께 어울리는 모습, 저는 노력해야 하는데 진우는 자연스레 나오는 것 같아 부럽고 배워야 하는 부분임에 분명합니다.

플라스틱으로 매듭 짓지만 그래도 강도팀의 장으로 생각되는 승규, 수학을 잘했고, 제 연구에 코멘트를 많이 줘서 감사합니다. 제 연구에 부족한 부분이 있을까 하여 염려해 주고, 걱정해 준 부분, 그 마음 고맙습니다.

인덕 이란 걸 타고난 것 같은 종형이, 진짜 덕이라는 걸 타고 난 것 같습니다. 어떻게 하면 저렇게 예쁨 받는 짓을 할 수 있지?? 종형이를 통해 행동, 대인관계, 그리고 사회성을 많이 배우고 가는 것 같습니다.

우주, 오민, 그리고 나정이, 너무 저한테 잘해 줘서 고맙습니다. 정말 연구실의 든든한 기둥인 것 같습니다. 우주와 오민이 정말 사랑스럽고, 알아서 잘해주고 또 나정이 하고 함께 지낼 때 멋진 남자의 모습이란 어때야 하는지를 잘 보여 준 것 같습니다. 역시 많은 부분 후배님들을 통해 배우고 나갑니다.

정준이형, 성기, 승훈이, 정준이형의 웃는 인상과 푸근했던 마음, 저하고 잘 맞았기에 논문이 나왔던 것 같습니다. 같이 디스커션 해주어서 감사합니다. 뒤에서 묵묵히 백업 해줬던 성기와 승훈이, 두 사람은 업무와 연구 스타일, 그리고 패션 부분에서 비슷한 점이 많아 보이지만 실상은 둘 다 개성이 확연히 다른 것 같습니다. 둘 다 말수는 적지만 성기는 매사를 진진하게 받아들이는 것이 장점이고, 승훈이는 순간순간 캣취하는 능력이 탁월한 것 같습니다. 둘 다 쉽지 않은 테마여서 좋은 연구 결실 맺길 바랍니다.

준상이하고 종호, 역시 수학적 도움을 많이 받았던 준상이, 고마웠습니다. 종호도 제 뒷자리에 앉아 여러가지 질문에 답변해 주어서 고마웠습니다. 준상이는 외모는 개구장이 이미지인데, 실상 생각하는 건 어른스러운 면이 있는 것 같습니다. 착하고 좋은 후배여서 고맙습니다. 종호는 오민이하고 합이 잘 맞는 것 같습니다.

앞으로 오민이하고 연구적 협력을 많이 하면 진짜 좋은 결과를 낼 수 있을 것 같습니다. 역시 착한 후배여서 고맙습니다.

혜련, 경열, 둘 다 연구적으로 끌어주고 싶은 후배여서 고마웠습니다. 혜련이는 앞으로도 잘 할 거라 생각되고 잘 될 것 같습니다. 밝은 성격이어서 고마웠습니다. 경열이는 운동에 많은 조언을 주어서 고마웠습니다. 잔류응력팀에서 좋은 연구테마 발굴하길 바랍니다. 워낙 친화력이 좋고 잘생기고 일도 잘하니 앞으로 연구하면 좋은 결과가 나올 것 같습니다. 막내들 파이팅입니다.

차마 챙기지 못해서 미안한 프론틱스, 법안전, 멀티스케일 센터 식구들 고마웠습니다. 함께 시간을 보낼 수 있어서 감사했습니다.

마지막으로 오랜 시간 참고, 맘 고생하신 부모님께 감사 드립니다. 부모님 속타게 너무 많은 시간을 보냈네요. 이제 효도하려 하니 오래오래 건강하세요. 결혼해서 며느리도 보시고, 손자손녀 재롱도 보셔야 하니 항상 건강하시길 바랍니다.

그간 열심히 달려왔지만, 막상 졸업 때가 되고 보니, 이제 시작이라는 생각이 듭니다. 이 자리에 있기 까지 도와주신 많은 분들께 감사 드리며 이 논문을 고마우신 분들께 바칩니다.
감사 드리고 항상 건강하세요.

2017 년 12 월 20 일 수요일
박 찬 평 올림